Stony Brook University

Integration of Process Diagnostics and Three Dimensional Simulations in Thermal Spraying

A Dissertation Presented

by

Wei Zhang

to

The Graduate School

in Partial Fulfillment of the

Requirements

for the Degree of

Doctor of Philosophy

in

Materials Science and Engineering

Stony Brook University

August 2008

Stony Brook University

The Graduate School

Wei Zhang

We, the dissertation committee for the above candidate for the
Doctor of Philosophy degree,
hereby recommend acceptance of the dissertation.

Professor Sanjay Sampath, Advisor
Department of Materials Science and Engineering

Professor Lili Zheng, Co-advisor
Department of Mechanical Engineering

Professor Dilip Gersappe, Chair
Department of Materials Science and Engineering

Professor David O. Welch, Member
Department of Materials Science and Engineering

Dr. Yuk-Chiu Lau, Outside Member
GE Energy

This dissertation is accepted by the Graduate School

Lawrence Martin
Dean of the Graduate School

Abstract of the Dissertation

Integration of Process Diagnostics and Three Dimensional Simulations in Thermal Spraying

by

Wei Zhang

Doctor of Philosophy

in

Materials Science and Engineering

Stony Brook University

2008

Thermal spraying is a group of processes in which the metallic or ceramic materials are deposited in a molten or semi-molten state on a prepared substrate. In atmospheric plasma spray process, a thermal plasma jet is used to heat up and accelerate loading particles. The process is inherently complex due to the deviation from equilibrium conditions, three dimensional nature, multitude of interrelated variables involved, and stochastic variability at different stages.

This dissertation is aimed at understanding the in-flight particle state and plasma plume characteristics in atmospheric plasma spray process through the integration of process diagnostics and three-dimensional simulation. Effects of injection angle and carrier gas flow rate on in-flight particle characteristics are studied experimentally and interpreted through numerical simulation. Plasma jet perturbation by particle injection angle, carrier gas, and particle loading are also identified. Maximum particle average temperature and velocity at any given spray distance is systematically quantified. Optimum plasma plume position for particle injection which was observed in experiments was verified numerically along with description of physical mechanisms. Correlation of spray distance with in-flight particle behavior for various kinds of materials is revealed.

A new strategy for visualization and representation of particle diagnostic results for thermal spray processes has been presented. Specifically, 1st order process maps

(process-particle interactions) have been addressed by converting the Temperature-Velocity of particles obtained via diagnostics into non-dimensional group parameters [Melting Index -Reynolds number]. This approach provides an improved description of the thermal and kinetic energy of particles and allows for cross-comparison of diagnostic data within a given process for different materials, comparison of a single material across different thermal spray processes, and detailed assessment of the melting behavior through recourse to analysis of the distributions. An additional group parameter, Oxidation Index, has been applied to relatively track the oxidation extent of metallic particles under different operating conditions. The new mapping strategies have also been proposed in circumstances where only ensemble particle diagnostics are available.

Through the integration of process diagnostics and numerical simulation, key issues concerning in-flight particle status as well as the controlling physical mechanisms have been analyzed. A scientific and intellectual strategy for universal description of particle characteristics has been successfully developed.

Dedicated to My Parents

献给我挚爱的父亲母亲

Table of Contents

Abstract of the Dissertation iii
Table of Contents vi
List of Symbols ix
List of Figures xii
List of Tables xv
Chapter 1 Introduction 1
1.1 Plasma Spraying Process 1
1.2 Plasma Jets 3
1.2.1 Definition of Thermal Plasmas 3
1.2.2 Characterization of the Plasma Plume 5
1.2.3 Numerical Modeling of Plasma Jets 5
1.3 Particle In-Flight 8
1.3.1 Description of Particle In-Flight Process 8
1.3.2 In-Flight Particle State Diagnostics 9
1.3.3 Current Status of Experiment and Modeling of Particle In-Flight 11
1.4 Knowledge Concerning Splat Formation 16
1.4.1 Experimental Studies on Splat Formation 16
1.4.2 Mathematical Simulation on Splat Formation 20
1.5 Objective of This Dissertation 21
Chapter 2 Statement of the Problem 23
2.1 Radial Injection of Particles into DC Plasma Jet 23
2.1.1 Injection Angle and Carrier Gas Flow Rate Effects on Particles In-Flight Characteristics 23
2.1.2 Study of Plasma Forming Process Parameters Effect on Optimum Particle Injection ('Sweet Spot') 25
2.2 Generic Correlation of Spray Distance with In-flight Particle Behavior for Different Kinds of Materials 26
2.3 Representation of Particle In-flight Characteristics and Development of Global Process Map 26
Chapter 3 Experimental Techniques and Mathematical Models 28
3.1 Diagnostics of Process 28
3.1.1 Single Particle Measurements 28
3.1.2 Ensemble Measurements 30
3.2 Mathematical Model for Plasma Flame and Particle-Flame Interaction 34
3.2.1 Plasma Flame 34
3.2.2 Interaction between Particles and Plasma Flame 37
3.2.3 Computational Domain and Mesh 42
3.2.4 Stochastic Scheme of Multiple Particle Generation 42
Chapter 4 Study of Injection Angle and Carrier Gas Flow Rate Effects on Particles In-Flight Characteristics 44
4.1 Introduction 44
4.2 Experiment and Simulation Setups 45
4.3 Results and Discussion 47

4.3.1 Injection Angle and Carrier Gas Effect 47
4.3.2 Influence of Injection Angle and Carrier Gas on Particle Size Distribution 56
4.3.3 Interaction between In-Flight Particle and Plasma Plume 57
4.4 Conclusions 61
Chapter 5 Plasma Forming Process Parameters Effect on Optimum Particle Injection 63
5.1 Introduction 63
5.2 Experiment and Simulation Setups 64
5.3 Results and Discussion 65
5.3.1 Effect of Process Parameters on In-flight Particle Behavior and Injection Optimization 65
5.3.2 Influence of Plume Angle on the In-flight Particle Behavior as A Function of Stand-off Distance 71
5.3.3 Effect of In-flight Particles on Plasma Plume 73
5.4 Conclusion 74
Chapter 6 Generic Correlation of Spray Distance with In-flight Particle Behavior for Different Kinds of Materials in APS 76
6.1 Introduction 76
6.2 Experiment and Simulation Setups 77
6.3 Results and Discussions 79
6.3.1 Experimental Observation of Particle State at Multiple Spray Distances 79
6.3.2 Simulation Results 84
6.4 Conclusion 89
Chapter 7 A Universal Method for Representation of In-Flight Particle Characteristics in Thermal Spray Processes 91
7.1 Introduction 91
7.2 Materials and Experimental Methods 96
7.3 Results and Discussion 97
7.3.1 Development of 1st Order Process Maps Across A Spectrum of Materials for A Single Process 97
7.3.2 Expanded Process Maps: Comparison Across Processes and Materials 100
7.3.3 Implications of Group Parameters on Materials and Process Assessment: Particle Size Effect in YSZ 102
7.3.4 Discussion on Distribution 104
7.3.5 Discussion on Particle Oxidation Status 110
7.3.6 1st Order Maps Based on Ensemble Particle Diagnostics 113
7.4 Conclusions 114
Chapter 8 Synthesis 116
8.1 Discussion on Salient Results 116
8.1.1 Radial Injection of Particles into DC Plasma Jet 116
8.1.2 Correlation of Spray Distance with In-flight Particle Behavior for Different Kinds of Materials 119
8.1.3 Representation of Particle In-flight Status 120
8.2 Integration of Results 122
Chapter 9 Conclusions 124
9.1 Particle Radial Injection into Plasma Jet 124

9.1.1 Injection Angle and Carrier gas Flow Rate on In-flight Particle Characteristics 124
9.1.2 Plasma Forming Process Parameters Effect on Optimum Particle Injection..... 124
9.2 Generic Correlation of Spray Distance with In-flight Particle Behavior for Different Kinds of Materials..... 125
9.3 Universal Description of Particle Characteristics and Development of Global Process Map 125
Chapter 10 Suggestions for Future Work 127
10.1 Improve Definition of Particle Molten Status..... 127
10.2 Improve Representation of Particle Oxidation Status..... 127
10.3 Continue Global Process Map Development..... 128
References:..... 129

List of Symbols

b	reference thickness, m
B_m	mass transfer number
Bi	Biot number, $Bi = hr_p / k_l$
Bim	mass transfer Biot number, $Bi_m = r_p h_m / \rho_l D_{o,l}$
C_p	specific heat, J kg^{-1} K^{-1}
C_D	drag coefficient
d_p	particle diameter, m
D	diffusion coefficient, m^2 s^{-1}
e	internal energy per unit mass, J kg^{-1}
E	electric field, V m^{-1}
f	frequency, Hz
f_{Kn}	factor of Knudsen number
f_{prop}	factor to account property variation
f_v	factor for mass transfer
F	force, N m^{-3}
Fo	Fourier number, $\text{Fo} = \alpha_l t / r_p^2$
Fo_m	mass transfer Fourier number, $\text{Fo}_m = D_{o,l} t / r_p^2$
h	heat transfer coefficient, W m^{-2} K^{-1}
h_f	latent heat of fusion, *J kg-1*
h_i	specific enthalpy, *J kg-1*
h_m	mass transfer coefficient, kg m^{-2} s^{-1}
J	current density, A m^{-2}
Ja	Jakob number, *Ja=cps(Tf−Tsub)/hf*
k	thermal conductivity, W m^{-1} K^{-1}
L_m	latent heat of fusion, J kg^{-1}
L_{evap}	latent heat of evaporation, J kg^{-1}
$\dot{m}_v$	vaporization rate, kg s^{-1}
$\dot{m}_{ox}$	oxidation rate, kg s^{-1}
p	pressure, kg m^{-1} s^{-2}
Pr	Prandtl number, $Pr=\nu/\alpha$
q	heat flux, J m^{-2} s^{-1}
$\dot{Q}$	energy input due to particles, *W m-3*
$\dot{Q}_{conv}$	convection heat transfer rate, J s^{-1}
$\dot{Q}_{rad}$	radiation heat transfer, J s^{-1}
$\dot{Q}_{vap}$	heat transfer rate for vaporization, J s^{-1}

r	radial coordinate, m
r_m	position of the melting interface, m
r_p	particle radius, m
Re	Reynolds number, $Re=\varrho Vd/\mu$
Re_P	particle Reynolds number, $Re_p=\varrho Vd_p/\mu$
S	Spray distance, cm
Sc	Schmidt number
Sh	Sherwood number
St	Stefan number, $St=cpl(Tp-Tf)/hf$
t	time, s
T	temperature, K
T_B	splat bottom temperature, K
T_m	melting point, K
Ts	particle surface temperature, K
$\vec{\tilde{u}}$	Favre average velocity vector, m s^{-1}
$\vec{u}'$	velocity fluctuation, m s^{-1}
V	velocity vector, m s^{-1}
V′	velocity fluctuation, m s^{-1}
V_P	particle velocity, m s^{-1}
We	Weber number, $We=\varrho V^2 d/\sigma$
u, v, w	fluid velocity components, m s^{-1}
W	molecular weight, kg mol^{-1}
x, y, z	coordinate, m
Yi	mass fraction of the ith species
Yo	oxidant concentration

Greek symbols

α	thermal diffusivity, m^2 s^{-1}
ε	emissivity
Δ	temperature factor
δ	skin depth, m
θ	circular coordinate
μ	viscosity, kg s^{-1} m^{-1}
μt	turbulent viscosity, kg m^{-1} s^{-1}
ρ	density of gas mixture, kg m^{-3}
ρ_p	density of particle, kg m^{-3}
Φ	viscous dissipation, kg m^{-1} s^{-3}
ω	angular frequency, rad s^{-1}
ξ	flattening ratio
σ	electrical conductivity, S m^{-1}

	Stefan-Boltzmann constant, W m^{-2} K^{-4}

Subscript

i	species i
j	solidification interface
f	film temperature
	fusion
l	liquid
m	melting
p	particle
s	solid
sub	substrate
t	turbulence
w	wall
∞	environment

Superscript

c	chemical reaction
$\tilde{}$	Favre average
T	transpose

List of Figures

Figure 1-1 Schematic of DC plasma spraying process 2
Figure 1-2 Thermodynamic and transport properties of typical plasma spray gases [4] 3
Figure 1-3 Schematic of integrated diagnostic sensor sep-up at CTSR [53] 10
Figure 1-4 A typical crystallization of a plasma sprayed metallic splat: (a) Plannar morphology[81]; (b) Heat flow and related grain structure[82] 17
Figure 2-1 Typical thermal spray process control parameters and variables 24
Figure 3-1Schematic of DPV 2000 and reference coordinate 28
Figure 3-2 Principle of measurement of DPV 2000 29
Figure 3-3 Schematic of the TDS system composing of IPP and SPT 31
Figure 3-4 Particle temperature and velocity measurement principle for Accuraspray 31
Figure 3-5 Picture of integrated sensor set up at CTSR 33
Figure 3-6 Schematic of particle heat transfer 39
Figure 3-7 Geometry and computational mesh in: (a) cross-section plane normal to the plasma jet, and (b) middle section plane of 3D plasma jet 42
Figure 3-8 Random distribution of particle size 43
Figure 4-1 Schematic of plasma spray process where θ is the injection angle ranging between -90 to 90 deg. The angle for $\theta > 0$ is called the down stream (same direction as jet flow) injection angle; for $\theta < 0$ it is called the upstream injection angle; $\theta = 0$ is the normal injection 45
Figure 4-2 Initial size distribution for YSZ particles in the experiments and numerical simulations 46
Figure 4-3 Experimental data: YSZ particle temperature and speed for normal injection, 5 degree and 20 degree injection angles at the spray distance of 130 mm 49
Figure 4-4 Simulation results: the effect of injection angle on particles temperature and velocity at the spray distance of (a) 130 mm, (b) 100 mm and (c) 70 mm, respectively 51
Figure 4-5 Simulation results: effects of injection angle on particle temperature and speed at the spray distance of 130 mm and primary gas flow rate of 30 SLM 52
Figure 4-6 Simulation results: effect of injection angle on (a) particle surface temperature, and (b) particle speed at different spray distances 55
Figure 4-7 Experimental results: particle size distribution. (a) Effect of the carrier gas flow rate for the injection angle of 20 deg and (b) Effects of injection angle at carrier gas flow rates of 5 SLM 57
Figure 4-8 Simulation results: particle trajectories with (a) plasma temperature field and (b) plasma velocity in the main flow direction; (c) temperatures of gas and particle vs spray distance at different injection angles; and (d) speeds of gas and particle vs spray distance at different injection angles. (operating conditions: primary gas flow rate of 45 SLM and carrier gas flow rate of 6.0 SLM) 61
Figure 5-1 Laser Strobe Control Vision ™ image of orthogonal external injection of particles into a DC thermal plasma jet[58] 63
Figure 5-2 Mean particle temperature and velocity (from 10,000 particles measured using DPV 2000) as a function of plume position for different primary gas (Ar) flows. Maxima could be observed in both T and V in each case. The plume position of the maximum is the same in each case 66

Figure 5-3 Plume position and definition of plume angle 67
Figure 5-4 Carrier gas effect on different sized particles. Particle trajectory for a carrier gas flow rate of 2.5 SLM (a) temperature profile (c) velocity field; for a arrier gas flow rate of 4.0 SLM (b) temperature profile, and (d) velocity field. ■: d=30 μm, ▼: d=50 μm, ◄: d=70 μm 69
Figure 5-5 (a) Tan of plume angle and ratio of initial vertical velocity to the horizontal velocity at the spray distance as a function of carrier gas flow for different primary gas flows. The vertical black lines correspond to the optimum injection. Blue horizontal line intersecting the velocity ratio axis shows that optimum injection occurs at the same value of velocity ratio. The red horizontal line intersecting the tan (θ) axis shows that the optimum occurs at the same plume angle (b) Relationship between Tan of plume angle and velocity ratio (at optimum injection, identical plume angle as well as velocity has been obtained respectively) 71
Figure 5-6 Mean values of (a) temperature, and (b) velocity at different stand off distances for carrier gas flow rate varying from 1.5 SLM to 8.0 SLM, highest T and V have been obtain at 4 SLM carrier gas flow corresponding to optimum plume angle 73
Figure 5-7 Temperature profiles of plasma plume for 30 SLM primary gas flow case: (a) without carrier gas and particle feeding, (b) 2 g/min feeding rate and (c) 20 g/min feeding rate 74
Figure 6-1 Initial size distribution for the feeding stocks in experiment and simulation 79
Figure 6-2 Statistical particle size distributions for YSZ at multiple spray distances (at flux center from DPV 2000) 80
Figure 6-3 Average particle size for YSZ, Mo and NiCrAlY at multiple spray distances (at flux center from DPV 2000)..... 81
Figure 6-4 Statistical distributions of particle velocity for Mo, with increasing spray distance, the whole distribution initially shifts to large values and then shifts back to small ones..... 81
Figure 6-5 Statistical distributions of particle surface temperature for (a) YSZ, (b) Mo and (c) NiCrAlY..... 83
Figure 6-6 Trajectories of different sized ZrO_2 in (a) temperature and (b) velocity fields. (c) maximum flux location and particle trajectory for different sized particles at different spray distances..... 85
Figure 6-7 Flame temperature and Particle surface temperature for (a) YSZ and (b) Mo 87
Figure 6-8 Numerical simulation results of particle molten status for (a) YSZ and (b) Mo 89
Figure 7-1 (a) T-V global process map, (b) M.I.-Re global process map and (c) M.I.-K.E. global process map..... 99
Figure 7-2 Global process map for multiple process and materials (a) T-V map and (b) M.I.-Re map..... 102
Figure 7-3 Nozzle and particle size effect on process window for YSZ (a) T-V map, (b) M.I.-Re map..... 103
Figure 7-4 (a) global process map considering temperature and velocity distribution; (b) global process map considering M.I. and Re distribution 105
Figure 7-5 Molten Content: Number percentage of molten particles..... 106
Figure 7-6 Statistical representation of global process map 107
Figure 7-7 (a) YSZ process map considering M.I. and Re distribution and (b) Correlation of average *M.I.*, *Re* and predicted splat thickness distribution..... 108
Figure 7-8 Al_2O_3 process map considering different processes and (a) temperature, velocity distribution;(b) M.I., Re distribution..... 110

Figure 7-9 Oxygen effect on particle in-flight status from simulation 111
Figure 7-10 (a) O.I.-M.I. and (b) O.I.-Re map for Molybdenum particles under different combination of nozzle and particle sizes combinations..... 113
Figure 7-11 Global process map considering different processes 114
Figure 8-1 Schematic of plasma plume and particle injection..... 117
Figure 8-2 Schematic of the so called 'Sweet Spot Location'..... 118
Figure 8-3 Tan of plume angle and ratio of initial vertical velocity to the horizontal velocity at the spray distance for different primary gas flows. The red circles correspond to the optimum injection. Blue horizontal line intersecting the velocity ratio axis shows that optimum injection occurs at the same value of velocity ratio. The red vertical line intersecting the tan (θ) axis shows that the optimum occurs at the same plume angle 119
Figure 8-4 Trajectories of different sized YSZ in temperature profile of plasma plume 120
Figure 8-5 Effect of injection angle and spray distance on (a) particle Melting Index (M.I.), and (b) particle Kinetic Energy (K.E.)..... 122

List of Tables

Table 1-1 Summary of gases used in plasma spray 4
Table 1-2 Summary of selected model and simulation results in DC plasma research 7
Table 1-3 Summary of selected model in particle-plasma interaction research 15
Table 3-1 Sensors presently used at CTSR: Principle, procedure and information obtained [54, 134] 33
Table 4-1 Operating conditions for plasma jet and carrier gas flow 47
Table 4-2 Properties of YSZ feedstock material 47
Table 4-3 Experiment results and model validation at 130 mm spray distance 49
Table 4-4 Simulation results at 130 mm spray distance 52
Table 4-5 Simulation results for injection angle effect at different spray distances 56
Table 5-1 Process parameters for experiment and simulation during air plasma spraying of YSZ 65
Table 6-1 Operating conditions used in the experiments and modeling 78
Table 6-2 Operating conditions and properties of the feedstocks 78
Table 6-3 Statistical values at ‘Flux Center’ for (a) temperature at different spray distance 85

Acknowledgement

I would like to thank Professor Sanjay Sampath and Professor Lili Zheng for their guidance and support in preparing and executing this work. Without their expertise and efforts this work would not have been possible. Special thanks go to Professor Hui Zhang for his inspiring advices and constant encouragement.

I would like to thank my dissertation committee members, Professor Dilip Gersappe, Professor David O. Welch and Dr. Yuk-Chiu Lau for their enlightening discussions and suggestions.

I am indebted to Dr. Anirudha Vaidya, Dr. Vasudevan Srinivasan and my CTSR colleague Jose Colmenares for providing me invaluable help on experimental data acquisition. I am also indebted to Dr. Hongbing Xiong and Dr. Mingyu Zhang who taught me so much about numerical simulation.

Thank you to all the wonderful friends and colleagues in the Center for Thermal Spray Research and Process Modeling Lab. They are Dr. Dang Cai, Hua Huo, Zhi Pan, Dr. Yang Tan, Dr. Brain Choi, Dr. Alfredo Valarezo, Dr. Meng Qu, Dr. Guanghua Wei, Dr. Haisheng Fang, and Jiuan Wei.

Most of all, thank you to my parents for their love, care and support during this whole process. Without them I don't know where I would be.

It is gratefully acknowledged to the financial support by MRSEC program of the National Science Foundation under award DMR 00890021.

Chapter 1 Introduction

Thermal spraying is a group of processes in which the metallic or ceramic materials are deposited in a molten or semi-molten state on a prepared substrate. The process involves the formation of combustion or plasma flame, feeding the fine metal or ceramic particles into the hot zone of the flame, and particle deposition on the prepared substrate. During the short time of flight, the particles are rapidly heated and accelerated, forming a spray of partially or completely melted droplets, facilitating the process of particle impact, spreading and solidification onto the prepared substrate. Since the momentum, heat and mass transports govern the whole process, control of these phenomena is critical to the quality of the coatings.

Due to the versatility and cost-efficiency of thermal spray processes, numerous industries have introduced the technology in the manufacturing process to produce high performance coatings [1, 2]. The tailored combination of material/coating can provide resistance to heat, wear, erosion, corrosion, etc. Coatings are also used to restore worn or poorly machined parts to the original dimensions and specifications or for their capability in manufacturing of high performance ceramics, composites, refractory metals and functionally graded materials. The scientific research, however, has lagged behind the technological applications due to the complexity of the phenomena involved. The integration of the scientific understanding of the complex process and approaches in the practice is therefore very important.

In this chapter, the current thermal spray knowledge is briefly reviewed. Specifically the versatility of the industrial thermal spray technologies, diagnostic techniques applied to them and the heat, mass and momentum transport phenomena in thermal spray are covered.

1.1 Plasma Spraying Process

Figure 1-1 shows the schematic of a DC plasma spray process, which includes the plasma generation, plasma and in-flight particle interaction and deposit formation on substrate. The plasma plume shows unusual properties such as high temperature, up to 14000K, high velocity, up to 2500 m/s, steep temperature and velocity radial gradients, up to 10^7 K/m and 5×10^5/s and also low gas density (1/30 to 1/50 of the room temperature gas). They are laminar in their core and turbulent in their fringes. When they exit the torch nozzle, the resulting vortices coalesce induces an engulfment process of the ambient gas with large scale eddies entraining bubbles of cold gas. In addition, the plasma jets are continuously fluctuating in length and position because of the continuous movement of the arc root on the anode wall, which results in a sort of piston flow.

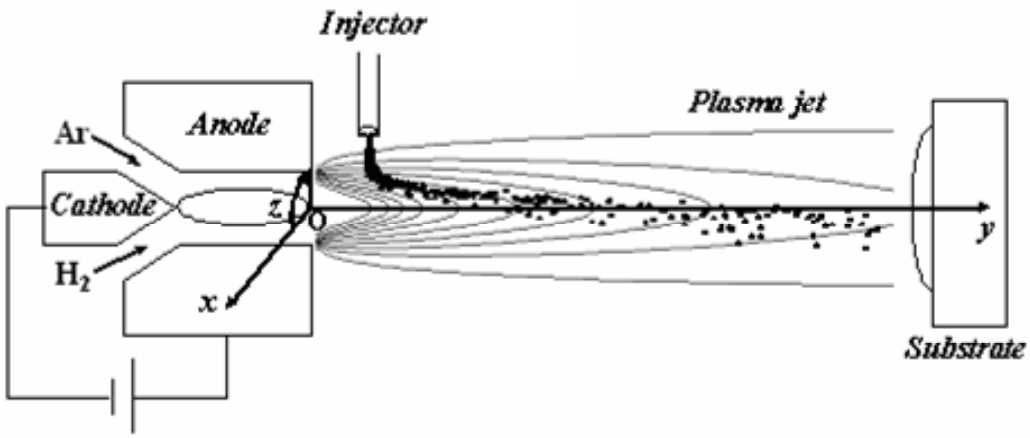

Figure 1-1 Schematic of DC plasma spraying process

In plasma spraying, the solid particles are injected into the plasma jet through an injector set downstream or upstream of the nozzle exit. In this injector, particles collide between themselves and the injector wall. Therefore, they have trajectory and velocity distributions at the injector exit. It results in a dispersion of their trajectories in the plasma jet.

Particles impact on the part to be coated at velocities between 100 to 300 m/s. The molten or semi-molten material spreads out from the point of impact and forms a lamella referred to "splat". The flattening time is below a few micro seconds and splat solidification generally starts before the flattening process is completed. The next particle that impacts a few tens of micro seconds later flattens on already solidified particles. The piling up of a few splats forms a pass in less than one millisecond. The next pass is deposited a few seconds later. The thickness of a pass varies between 3 and 60 microns. The flow and heat transfer phenomena during the impact and solidification processes control the microstructure and thermo-mechanical properties of coatings. The build-up of a coating in plasma spraying is a multi scale problem with time scales ranging between microseconds and seconds and length scales ranging from a few micrometers to a few hundred micrometers or more.

The main advantage of this process is that there is no limitation to the melting temperature of the sprayed materials. This significantly extends the technology possibility to any material that could be melted, including refractory ceramics. Plasma spray is also highly efficient, reliable and easy to handle. Because of these advantages, plasma spray has become one of the most common techniques to produce functional coatings. The typical feeding rate of plasma spray is 3-5 kg/h. The plasma spray process is cost-effective, and is an excellent fit for applications where the extremely low porosity is not a priority and where substantial amounts of material must be applied. It is also the only method by which ceramics can be efficiently thermally sprayed.

1.2 Plasma Jets

1.2.1 Definition of Thermal Plasmas

Plasma is a dense cloud of electrons, ions, atoms and molecules. There is no clear-cut boundary between the plasma and the gas. It remains many of the properties of the gases and also satisfies the physical laws valid for gases. Specific properties of plasma different from the neutral gases rely on its response to electro-magnetic forces [3]. Plasma can be produced by transferring energy into a gas until the energy level is sufficient to ionize the gas, allowing the electrons and ions to act independently of one another. The plasma state is achieved when, under an electric field, currents can be sustained as the free electrons move through the ionized gas. Once the energy input is removed, the electrons and ions recombine, releasing heat and light energy.

In DC plasma arc, enthalpy of gas needs to be sufficient to generate core plasma temperatures, which may exceed 20,000°C, depending on the gas properties and its electrical breakdown characteristics. Figure 1-2 shows energy density, or enthalpy values of the typical plasma spray gases. Enthalpy of gas indicates the heating potential for gas when it is heated to the plasma state. The monatomic gas, such as Argon and Helium, simply ionize, generating their respective ionic species, Ar^+ and He^+, and their related free electrons. Figure 1-2 also plots the energy content of the gases as a function of temperature. Note that the diatomic gases, for example Nitrogen and Hydrogen, have higher enthalpies for a given excitation temperature, which is related to the dissociation of their molecular structure, followed by ionization.

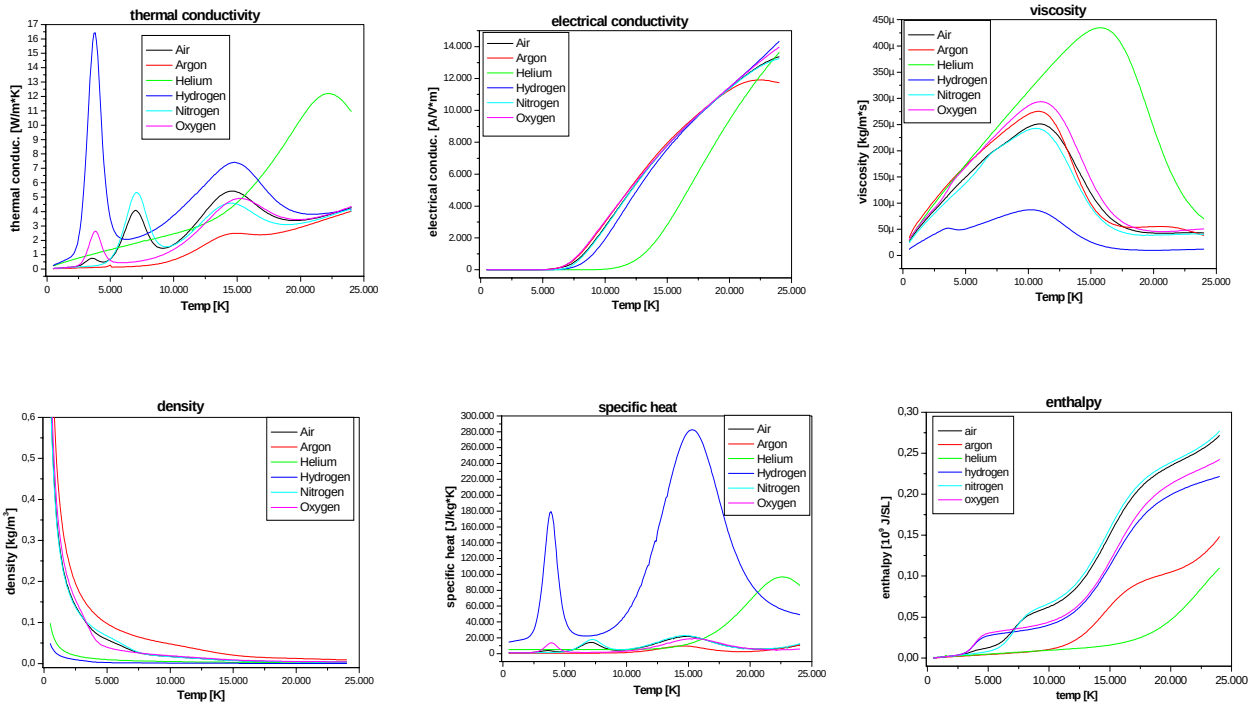

Figure 1-2 Thermodynamic and transport properties of typical plasma spray gases [4]

Depending on the material and torch, the plasma-forming gas can be pure Ar, Ar-He, Ar-H_2, N_2-H_2, or Ar-He-H_2. The various spray gases contain always a heavy gas such as argon or nitrogen to achieve a high gas momentum. The latter helps to push and stabilize the arc root down stream in the anode nozzle, and accelerate the particles without using a too high gas flow rate. For example, adding H_2 to Ar can increase its enthalpy and thermal conductivity significantly and decrease the viscosity [5]. Summary of gases used in plasma spray is listed in Table 1-1.

Table 1-1 Summary of gases used in plasma spray

Gas	Application for thermal spray
Argon	-Key process for many thermal spray applications, particularly plasma spraying, because it is less aggressive toward electrode and nozzle hard ware; -Completely inert and easily ionized, it can be used as the primary plasma gas or as a secondary gas with nitrogen to increase its energy; -Used as a powder carrier gas in a completely inert environment.
Hydrogen	-Ideal for applications where high heat, low oxidation and high particle velocities are required; -Also used in plasma spray applications to affect the plasma energy and plume characteristics.
Nitrogen	-Can be used as the plasma gas for electric arc and plasma spraying or for shrouding of plasma, electric-wire and HVOF to produce near vacuum chamber quality coatings at low cost with insignificant oxide inclusions and porosity; -Cost-effective plasma gas, generally inert to most materials, with exceptions like titanium; -Used alone as a primary gas or as part of a gas blend.
Helium	-A noble gas, completely inert to all spray materials, with good heat transfer properties and a high sensitivity for better plasma energy control; -Often used as a secondary gas with argon when hydrogen and nitrogen could cause deleterious effects; -Increasingly important as a carrier gas in cold spray applications where particle velocity is critical.
Oxygen	-Used to enhance combustion in HVOF and flame spray operations.

The high temperature of the plasma is reduced near the walls of the water-cooled anode, leading to a boundary layer of low electrical conductivity [3]. This layer compresses the plasma, leading to an increase in the temperature and pressure at the core of the plasma. This is known as the thermal pinch effect. A magnetic pinch is concomitant with the thermal effect because the core of the plasma is electrically

conductive and the electric field lines encircle the plasma flame, further confining plasma core and increasing its energy density.

1.2.2 Characterization of the Plasma Plume

Many techniques have been utilized to characterize the plasma jet for its composition, temperature and velocity. In the plasma jet with temperatures approaching 15000 K, traditional temperature measurement techniques, such as thermo-couples, can not be used. Plasma temperatures can be measured with the help of atomic or molecular spectroscopy, as well as by two-color pyrometry at two wavelengths. The plasma velocity can be measured with either a Pitot tube probe technique [6] or with a time-of-flight two-point laser anemometer [7]. The first method relies on very stringent simplifying assumptions for the local values of Reynolds number, plasma density and viscosity. The second one is limited by laser beam diffraction and the inhomogeneous seeding across zones of steep velocity and temperature gradients. Despite these limitations both methods are frequently used to estimate plasma jet velocities in order to optimize plasma spray conditions and coating quality.

In plasma core, optical methods which are based on the propagation of light fluctuations due to arc root fluctuations can be used [8]. In plasma plume, enthalpy probes with mass spectrometer are usually used [9-11] to follow-up the transient behavior of the plasma plumes. CCD cameras coupled with nitrogen-pulsed laser illumination [12] or high speed video systems [13] are utilized for the imaging.

Whatever the measuring method used, the existence of local thermodynamic equilibrium is questionable, especially in the jet fringes, at the jet core extremity (where the jet becomes fully turbulent) or when a cold gas or liquid is injected. However, local thermodynamic equilibrium is generally assumed because most of the measurements needed are comparative values related to torch working conditions [14].

1.2.3 Numerical Modeling of Plasma Jets

A series of models has been proposed [15-19] to calculate the plasma jet temperature and velocity distributions. By matching with the plasma gas flow rate and enthalpy, these models calculate temperature and velocity distributions at the nozzle exit. The codes consist in momentum and thermal energy equations for the multi-component species mixture, continuity equations for each component of the mixture taking into account the mixing with the surrounding atmosphere but usually neglecting chemical reactions, and state relations for an ideal gas mixture with temperature-dependent specific heat, enthalpy and transport properties. Recently, Tokar et al. [19] developed an approach to solve transport equations numerically for plasmas with spontaneously arising and arbitrarily located transport barriers. Compared to standard methods, this approach reduces the number of operations required to obtain a converged solution significantly. Mariaux [20] developed a 3D transient model of plasma spray, in which

the conversion of energy in the torch nozzle, from electric power to thermal energy, is considered. The power generation is assumed uniform throughout the medium and takes into account as a source term in the heat equation. This simple model yielded an estimation of the effective power of the torch. However, no comprehensive and reliable model can currently take into account the arc column inside the torch with its attachment to the anode-nozzle wall, which is a full 3-D unsteady state problem. The local thermodynamic equilibrium is generally assumed except for the two-temperature model studied by Chang et al. [17], in which the electrons and heavy particles have different temperature. The plasma is treated as a compressible, continuous multi-component, and chemically reacting ideal gas with temperature-dependent thermodynamic and transport properties.

In the past most numerical simulations have been conducted in a 2-D computational domain in which the axisymmetric assumption is necessary [21-23]. In fact, the plasma jet exhibits three-dimensional behavior due to the side jet injection of particles and the fluctuation of the plasma jet. Therefore, a transient three-dimensional model is needed to fully describe the effects of side carrier gas jet and injected particles. More and more recently published papers used 3-D model to simulation plasma jet. Wang et al. [24] used a three-dimensional model to simulate laminar-plasma in material re-melting processing. Modeling study is performed concerning the heat transfer and fluid flow for a laminar argon plasma jet impinging normally upon a flat work piece exposed to the ambient air. Cheng et al. [25] conducted three dimensional simulation research of shrouding gas effects on a laminar argon plasma jet impinging upon a flat substrate in air surroundings. Ahmed and Bergman [26] studied the ceramic particles in Ar-H_2 plasma jet using a 3-D model coupled with the commercial computational code FLUENT. Vardelle et al. [27] have performed 3-D simulations for the plasma spray process using the commercial computational fluid dynamics code ESTET. Li and Chen [28] developed a three-dimensional computational model that is capable of handling transverse carrier gas injection and its influence on the plasma jet behavior and particles trajectories. Noted that most three-dimensional models so far are based on the assumption that the particle temperature is uniform across the radius during in-flight, and some models neglect the effects of particles on the plasma gas.

Various models have been also been adopted in the numerical simulations of turbulent jet under plasma conditions: mixing hypothesis [29, 30], two-equation k - ε model [31-33], multiple time scale turbulence model [34], etc. The most commonly used model is the k - ε model, if necessary, with the correction to account for low Reynolds number. Although the results predicted by the k - ε model are not satisfactory, it has provided semi-quantitative information on the plasma jet. Cheng et al. [35] studied turbulent argon thermal plasma jets issuing into ambient air. The three dimensional simulation results were also compared with the characteristics of laminar plasma jets. It was found that the length of the high-temperature region of the laminar plasma jet is

much longer and increases notably with increasing jet inlet velocity or inlet temperature, while the length of the high-temperature region of the turbulent plasma jet is short and less influenced by the jet inlet velocity or inlet temperature. Cheng et al. [32] investigated entrainment of ambient air into a turbulent argon plasma jet. It is shown that the entrainment of ambient air into the turbulent argon plasma jet can be treated simply by the combined turbulent and molecular diffusion between only two different gases (argon and air).

Some researchers turned to more sophisticated turbulence model, and found that the multiphase models could be a better choice for turbulent flow. Huang et al. [36] developed a two-fluid model for an argon plasma jet flowing into an argon stagnant environment. In their study, the plasma jet was considered as a two-fluid mixture consisting of hot, out-moving fragments and cold, in-moving fragments. Lin et al. [37] used a multiphase transport model for relativistic heavy ion collisions simulation. The simulation results have been compared with experimental data and good agreements were achieved. A summary of selected model and simulation results has been listed in Table 1-2.

Recently, a three-dimensional transient numerical model for plasma jet and particle is developed by Xiong et al [38, 39] to investigate the plasma jet perturbation by carrier gas and particle loading, and their effects on the in-flight particle behavior. The plasma jet and the particle trajectory are described in the three-dimensional geometry, and the non-thermal equilibrium of the particle in-flight is considered by employing one-dimensional thermal model. This model is incorporated into the LAVA code, originally developed at INEEL in a two-dimensional geometry. The modified computational code LAVA-P-3D has been tested with experiment and further applied to thermal spray process. The detailed literature review of modeling work of particle in-flight and its interaction with plasma jet will be covered in the following section.

Table 1-2 Summary of selected model and simulation results in DC plasma research

Author & references	Model and simulation	Comments
Ramshaw and Chang, 1995 [40]	Implicit calculation of kinetics and equilibrium chemical reaction.	Comprehensive model
Chang and Ramshaw ,1996 [17]	Model the non-equilibrium effects in nitrogen and Hydrogen plasma.	
Huang, 1995 [36]	Two-fluid turbulence model, which considered two parcels: in-moving and out-moving.	
Ahmed, 2001 [26]	3D model to study melting of the ceramic particles.	Using commercial code FLUENT
Vardelle, 2001 [41]	3D simulation of plasma jet generation and	Using commercial

	particle injection.	code ESTET
Xiong, 2004 [38]	3D simulation of plasma jet generation and particle injection. Considering interaction between plasma jet and in-flight particle.	Comprehensive model

1.3 Particle In-Flight

1.3.1 Description of Particle In-Flight Process

Particles are injected into the plasma jet through one or two injectors by a carrier gas. The injection geometry (injector design, position and angle with the torch centerline) and the mode (in-side or outside the nozzle) to a large extent control the distribution of particle trajectory in the plasma jet and, therefore, their acceleration and heating process. In most cases, the injector is orthogonal to the jet axis either inside the anode-nozzle (downstream of the arc root) or outside it[42]. Typical injector internal diameters range between 1.5 and 2 mm.

The powders used in plasma spraying may have very different morphologies depending on the manufacturing process. Even if powders manufactured by various processes may appear to be equivalent with respect to chemical composition and particle size distributions, they will have different treatment in the flow and properties of the resulting coatings. The particle characteristics that affect their treatment in the gas flow are mainly their shape that controls their floatability, their density that affects their acceleration and heating, and their purity. During their pneumatic transport through the injector, they collide between themselves and the injector wall. These collisions are responsible for the particle jet divergence at the injector exit. This divergence is specially marked for particles with diameters below 20 microns and it will result in a broad distribution of trajectories within the plasma jet. The dispersion of particles by the flow turbulence enhances this phenomenon [42].

When the particles penetrate the plasma jet core, they are firstly heated and accelerated. Then, in the plasma plume, they decelerate and slowly cool down. Particles treated in DC plasma flows have a residence time in the millisecond range and receive a heat flux as high as 10^8 W/m^2 [43]. As a result of the high gradients in the plasma jet, particles which follow different trajectories will have different accelerations and heating history. For example, the larger and denser particles are more resistant to the flow drag force and spend more time in the plasma jet, which is favorable for the plasma spray process. However, for large particles of low density and low conductivity materials the rate of heat conduction in the particles may be too slow to ensure a homogeneous heating and melting during the residence time of the particles in the plasma jet. Particles can react in flight with the plasma gas or surrounding gas which mixes with the plasma jet, and undergo chemical reactions, decomposition and evaporation [18]. In addition, the large difference between particle and flow velocity may induce convective

movements with the molten droplets, at least those which melting temperature is below 2300K [37]. This results in a continuous renewing of the liquid material at the particle surface. For metal or alloy particles sprayed in air, this liquid movement brings about a high oxidation rate enhanced by the presence of atomic oxygen in the plasma plume.

1.3.2 In-Flight Particle State Diagnostics

During the past decade, plasma plume and in-flight particle interactions have been investigated extensively. A large number of measurement techniques have been developed and commercial instruments based on these have been applied to study the particle state in thermal spray processing.

Methods such as Laser Doppler Anemometry have been used to measure the trajectories and velocities of individual particles in plasma plume [44]. Time of flight techniques have also been adapted by varying the methods of detecting particles. These include methods such as recording particles based on thermal emissions and providing active illumination with laser light to detect the particles. High speed two-color pyrometric techniques have been used to measure ensemble average as well as single particle temperatures [45]. The DPV2000 manufactured by Tecnar utilizes this principle [46] and is being used widely in the thermal spray industry and research establishments. Based on the research of Fincke et al [47], the in-flight particle temperature T_p, velocity v_p and diameter d_p measurements for each single particle can be observed one at a time. Average temperature, velocity and diameter can be measured using ensemble techniques, where the sensor observes an ensemble of particles simultaneously. The difficulty involved in the single particle technique depends on the number of particles in-flight, which is at the minimum (lower powder flow rate of about 10 g/h) of 10^6 part/s. Thus, the particle measurement volume is limited so that individual particles can be observed without overwhelming interference from the other particles. Simpler diagnostic instruments based on CCD cameras, such as the 'Spraywatch' [48], have also been developed and are increasingly finding their utility in spray booths. Another innovative technique has been developed, Particle Shape Imaging (PSI), which records the shape and size transformation of powder particles in flight [49]. Ensemble-averaged imaging of the spray jet has been used in the Particle Flux Imaging (PFI) system to track changes in flux density. The technique approximates the spray plume with ellipses and monitors changes in critical parameters of these ellipses [50]. The evaporation rate of particles can be measured either by emission spectroscopy of metallic species or by absorption spectroscopy in plasma plume. The condensation of vapors from the vaporized particles in the plasma plume can be measured by using an electrical low pressure impactor [51]. The loading effect (plasma jet cooling) of particles can be obtained through the emission of an argon atomic line whose intensity decreases when the mass flow rate of particles increases [52].

There are two additional important issues regarding particle measurements. The first one is related to the sensor limitations. For example, pyrometers are limited to temperatures over about 1800K and lower temperature particles are not seen. Similarly laser anemometers are limited to particles over a few micrometers large. The second observation is related to the plasma jet core emission. The flux emitted or scattered by the particle must be higher than that of the continuum. The observation wavelength of the emitted, scattered or reflected light must be chosen in a wavelength range where neither line nor molecular emission exists. Pyrometry measurements are therefore only possible in the plasma plume and laser scattering in the plasma core requires high power continuum wave lasers. Of course, high-power pulsed lasers can be used to visualize particles in the plasma core[45].

Integrated multi-sensor approach adopted at CTSR which is shown in Figure 1-3 can not only enable closer look at the process but also facilitate cross-correlation of sensor data and enhance the understanding of the sensors themselves as well as the process [53]. The detailed descriptions of all the sensors used can be found in Chapter 3. Thorough understanding of the data from these different sensors combined with fundamental understanding of the process would lead to strategies to control the process using these sensors in real-time or near-real-time.

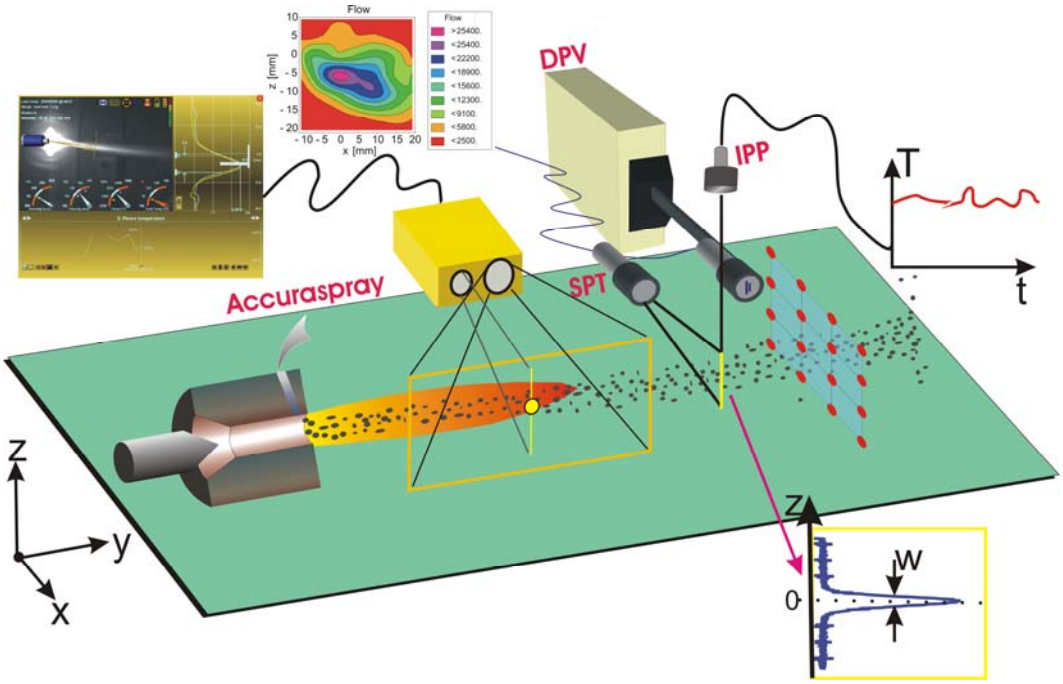

Figure 1-3 Schematic of integrated diagnostic sensor sep-up at CTSR [53]

1.3.3 Current Status of Experiment and Modeling of Particle In-Flight

The interaction between the particles and the plasma jet is a critical factor determining the final coating properties, which to a large extent depend on the particle temperature, velocity and melting status at the impact on the substrate. The literature review of experiment and modeling study of particle flight are briefly summarized as the following.

1.3.3.1 Experimental Studies on Particle In-Flight

Various experiments have been conducted to investigate particle flight behavior in order to improve the coating properties.

Li et al. [54] studied particle characterization and splat formation of plasma sprayed zirconia. A process map study has been carried out to examine the role of process variables on the properties of the deposit formed in thermal spray. A group parameter, melting index, is used to interpret the molten state of particles, which also reflects the thermal energy of the particles. The kinetic energy and fluidity of particles are characterized through their Reynolds number. Splat morphological features such as flattening and fragmentation are characterized against the group parameters. Deposition rate test confirms the significance of the concept of melting index. It is highlighted in this paper that particle group parameters, i.e., melting index and Reynolds number describe the particle in-flight status very well and can be used to predict the deposit behaviors.

Fang et al. [55] studied influence of in-flight particle characteristics on the forming quality. Relationships between the melting state, the in-flight property of particles and the forming quality were investigated. The experimental results show that the temperature field distributions of plasma jet are mainly affected by plasma generator power though CCD imaging and gray-scale processing. The velocity of in-flight particle is directly determined by the flow rate of work gas, and the surface temperature of in-flight particle is obviously affected by assisted gas rate. The energy coupling and momentum transferring between plasma and particle have a significant influence on deposition efficiency, porosity, microhardness and microstructure of spray-formed parts, and it also provides a good idea to control the forming quality on-line.

Guessasma et al. [56] et al. studied velocity and temperature distributions of alumina-titania in-flight particles in the atmospheric plasma spray process. Control of the thermal spray process generally considers the monitoring of the mean in-flight particle characteristics (i.e., mean velocity and temperature) during the coating process. Three processing parameters (arc current, primary and secondary plasma gas flow rates) were correlated to the characteristic distributions in the case of alumina-titania in-flight particles. A high speed two color pyrometer was used to measure the individual in-flight particle characteristics at the center of the particle flow, which were used to build

velocity and temperature distributions. Results showed a change on characteristic distributions and demonstrated a significant effect of the energetic parameters in the control of the in-flight particle characteristics.

Control of the powder injection also plays an important role on coating properties. A number of studies were conducted to investigate how powder chemical composition, particle size distribution and morphology, and injector size, shape, position and location affect the coating properties [41, 57-60]. Particle morphology [54, 61], which is related to the powder manufacturing techniques, plays an important role on pneumatic feeding. Research shows that both the injection method and the homogeneity of the particles are key parameters for coating behavior, especially at high temperatures.

Not much work has been published for systematical study of particle oxidation during flight. Oyed et al. [62] studied the oxidation of stainless steel particles in the plasma jet. Two types of 316L austenitic stainless steel particles were sprayed in ambient or controlled atmosphere with varying torch parameters and surrounding gases composition. It was shown that besides diffusion based oxidation, convective oxidation in the particles can occur within the plasma jet core if plasma to particle kinematic viscosities ratio and relative Reynolds number (Re) are superior to 55 and 20, respectively. The oxide formed or oxygen dissolved at the surface of the liquid particle can be swept into its interior forming isolated oxide nodules. Fresh liquid metal is transported from interior towards particle surface. The oxidation rates were estimated to be higher compared to diffusion based oxidation. The diffusion based oxidation of particles in the plasma jet plume can be principally controlled by their size (specific surface area), temperature and velocity (dwell time) and the molar fraction of oxidizing and reducing species in the plasma jet. While investigating the influence of the atmosphere of plasma jet on the in-flight particle oxidation, it was found that the surface area of the oxide nodules and the mass percentage of total oxygen in collected particles followed a parabolic and linear relationship with $p(O_2)$ in the surrounding atmosphere. Keeping surrounding $p(O_2)$ at 0.1 and altering N_2 and Ar content resulted in higher oxygen content in particles sprayed in Ar rich surrounding whereas no distinct difference in oxide nodules surface area was measured.

1.3.3.2 Numerical Simulations of Particle In-Flight

To understand the effect of in-flight particle behavior so as to improve the coating quality, an accurate description of transport phenomena of particles is essential. Current status of the modeling work about particle physics in thermal spray is briefly reviewed as the following.

1.3.3.2.1 Physics of particle behavior in flight

Most models treat the particles in the flow as discrete Lagrangian entities that exchange mass, momentum, and energy with the gas [39, 63, 64]. Special characteristics of thermal plasma, such as steep temperature gradients in the boundary layer surrounding the particle, non-continuum effects (Knudsen effect), varying plasma properties, thermophoresis, turbulent dispersion, evaporation, etc. have also been studied [65]. However, the understanding of particle behaviors in plasma jet is not complete, especially for particle phase change, evaporation and oxidation.

Because the molten state of the particles at impact will affect the particle spreading and solidification, many efforts have been devoted to optimizing operating conditions to ensure complete melting of particles before impact on the substrate. He et al. [66] investigated particle melting during HVOF thermal spraying using Inconel 625 powders. They concluded that the volume fraction of unmelted particles in the coatings was dependent on the proportion of powder within a specified size range, 30 to 50 μm in their experiment. Dyshlovenko et al. [67] studied hydroxyapatite powder behavior in plasma jet. Numerical simulations of hydroxyapatite (HA) coating deposition by plasma spraying were conducted. The velocity and temperature fields of $Ar+N_2$ plasma generated by a commercial plasma torch of given power at atmospheric pressure are calculated three-dimensionally using the GENMIX numerical code. The trajectories and temperatures fields inside particles were calculated numerically using Plasma 2000 code. These fields determined at experimental spray distance were used to predict the crystal phases composition of the sprayed coating Fauchais et al. [68] investigated the behavior of particles in-flight and demonstrated the surging and whipping of the plasma jet due to the arc-root fluctuations, which changes the mean trajectory of the particles and the engulfment process of the air entrainment. Prystay and Moreau et al. [69] used an integrated optical monitoring system to measure the particle velocity and temperature and studied the correlation between particle temperature and velocity with the structure of plasma-sprayed zirconia coatings. It was shown that the temperature of the sprayed particles had a significant effect on the coating properties than the velocity for their operating conditions. Ahmed and Bergman [70] simulated processing of nanostructured zirconia agglomerates with plasma spraying. Transition regions for the phase change response of the sprayed material to the thermal processing conditions were identified. The retained nanostructure content and liquid fraction of the sprayed material are correlated to particle diameters, injection velocities, as well as this thermal spray processing parameter. A novel method to produce desired coatings composed of partially molten material using a bimodal particle size distribution of the sprayed powder is suggested. Delluc et al. [71] conducted modeling of plasma jet and particle behaviors in spray conditions. A simplified code was developed to study the effects of the different macroscopic spray parameters. The 3D features of plasma jet induced by

the carrier gas jet and powder injections have been investigated by Xiong [38], through which the understanding has been improved for plasma jet behavior. More accurate prediction of particle acceleration, heating, melting and metal oxidation has been achieved using this 3D model.

Research has also been conducted to understand the in-flight particle melting in various thermal spray processes [39, 64, 66]. The effects of the melt fraction on the splat morphology, however, are not fully understood. Vaidya *et al.* [54] conducted investigation of the splat morphology over a wide range of particle conditions. They defined a "melting index" to indicate the particle melting state based on the in-flight temperature, velocity and diameter, and correlated this parameter with the splat morphology after impact. This index was further refined by Zhang *et al*. through energy analysis [72]. A thermal network analysis has been employed by Xiong et al. [39, 73] to identify the particle melting status. A dimensionless number, melting index, has been defined and correlated with the experimentally measurable parameters to estimate the melting fraction of the particles. Numerical results and experimental data were also used to validate the melting index.

1.3.3.2.2 Particle oxidation

The plasma spraying of metals under atmospheric conditions will inevitably cause oxide formation. The oxygen content and oxide types are related to various parameters, such as particle temperature and velocity, spray distance, feedstock composition, plasma gas type, and substrate temperature. Also, the high temperature encountered in thermal spraying results in the formation of a wide variety of oxide structures. The oxides within the particles upon impact will affect the coating properties significantly. Currently, most applications of spray coating require low oxide levels, since the coating performance will be degraded due to the brittleness and reduced corrosive resistance by the oxide within the coating. However, the general opinion that oxides deteriorate the coating properties may not be necessarily true [74]. Rather it may lead to new application of forming coatings with controlled proportions of metal and oxide phases. Therefore, it is desirable to understand the mechanism of oxidation and its effect on coating properties, and hence to control the amount, composition and distribution of oxides within the deposits.

There are two stages of oxidation exist in thermal spray, i.e. in-flight oxidation and splat oxidation. During the first stage, particles interact with the entrained air. Oxidation in this stage strongly depends on the particle temperature and whether the molten or solid particle can react. In the second stage, the solidified deposit material interacts with a gaseous mixture consisting mainly of the ambient atmosphere, which is characterized by rapid decrease of splat temperature. Hackett et al. [75] discussed three possible sources of oxidation during plasma spray: (i) in the core of the flame, (ii) at the end of the plume to the substrate and (iii) during the time on the substrate exposed to

hot gases until subsequently covered by another layer of splats. It was concluded that oxidation occurs primarily on the substrate. However, Vardelle et al. [76] discussed that oxidation does not primarily occur at the substrates, it is rather from the in-flight part.

It is still challenging to model the oxidation of metal droplets in thermal spray. Vardelle et al. [76] presented an estimation of the oxidation of pure iron during plasma spraying by assuming that the gas-phase diffusion as the rate-controlling process. A quasi-steady-state model of the iron particle oxidation during deposition was proposed by Smith et al. [77], in which diffusion of Fe through FeO_2 scale in the solid state as the rate-limiting step was considered. Wan et al. [64, 65, 78, 79] developed a comprehensive oxidation model for covering broad temperature ranges during the particle flight and deposition. Their model considered oxidant diffusion around the particle surface or spat, oxidation on the surface, as well as oxygen diffusion in the molten molybdenum. The effects of particle size and other parameters, such as particle temperature and velocity, on oxidation and evaporation have not been discussed. Xiong et al. [73] presents analysis and characterization of the melting and oxidation behavior of in-flight particles. Two practical parameters, melting index and oxidation index, have been proposed to estimate the melt fraction and the oxide content, respectively. Values of those two indices have been validated by the three-dimensional simulation results for two common materials, ZrO_2 and Mo. Table 1-3 listed the summary of selected modeling work on plasma and particle interaction.

To summarize the review of experiment and simulation work of characterization of particle behavior in flight and its effect on the coating quality, it is found that systematic study of particle behavior under various spray conditions using an approach integrating experiment and numerical simulation is missing. Besides, effect of oxidation on in-flight characteristics as well as resulting deposition quality need to be further investigated.

Table 1-3 Summary of selected model in particle-plasma interaction research

Author & references	Model and simulation	Comments
Chen and Pfender, 1985 [80]	Momentum and heat transfer to a single particle exposed to thermal plasma.	
Vardelle, 1995 [76]	Present an estimation of the oxidation of pure iron during plasma spray.	Assume the gas-phase diffusion as controlling process.
Smith, 1997 [77]	Propose a quasi-steady state model of the iron particle oxidation during deposition.	Consider the diffusion of Fe through FeO_2 scale in the solid state as the rate-limiting step

Wan, 1999 [64], 2001[78] , 2002 [79]	Model of in-flight particle evaporation and oxidation (Molybdenum).	Consider evaporation controlled by vapor diffusion through boundary layer.
Xiong, 2005 [73]	Melting and oxidation of in-flight particle (YSZ and Molybdenum)	Defined non-dimensional parameters to represent molten and oxidation status

1.4 Knowledge Concerning Splat Formation

In general, a successful application of thermal-sprayed coatings to engineering usage depends strongly on the quality of the adhesion between the coating and the substrate or the previously deposited layers. In most cases, the adhesion/cohesion is of the mechanical type; surface pits and grooves of a rough surface are filled with the spreading molten material due to the impact pressure. Subsequent solidification leads to mechanical interlocking. However, inter diffusion and possibly chemical reactions across the substrate or previously deposited layers may occur if the heat transfer from the impinging molten particles causes a local melting of the layer underlying the flattened particle.

Since this thesis is more focused on study of particle in-flight state, experimental and numerical studies of splat formation will only be briefly reviewed in this section.

1.4.1 Experimental Studies on Splat Formation

Herman and Safai[81] had investigated the grain morphology of plasma sprayed aluminum splat in their early work. Sampath[82] extended the study of rapid solidification and microstructure development during plasma spray to nickel, molybdenum and Ni-Al alloys. Figure 1-4 shows a schematic of the planar morphology and heat flow related grain structure of a solidified metallic particle. According to their study, in the central core region, where the particle first comes into contact with the surface, heat is extracted through the substrate, which makes the central part undergoes a sufficient undercooling to crystallize as equiaxed grains. However, the peripheral areas, where the heat is not extracted through the substrate but rather back through the core region, exhibit a poorer contact with the substrate and a slow cooling rate resulting in radially elongated grains that propagate from the core and terminate at the rim.

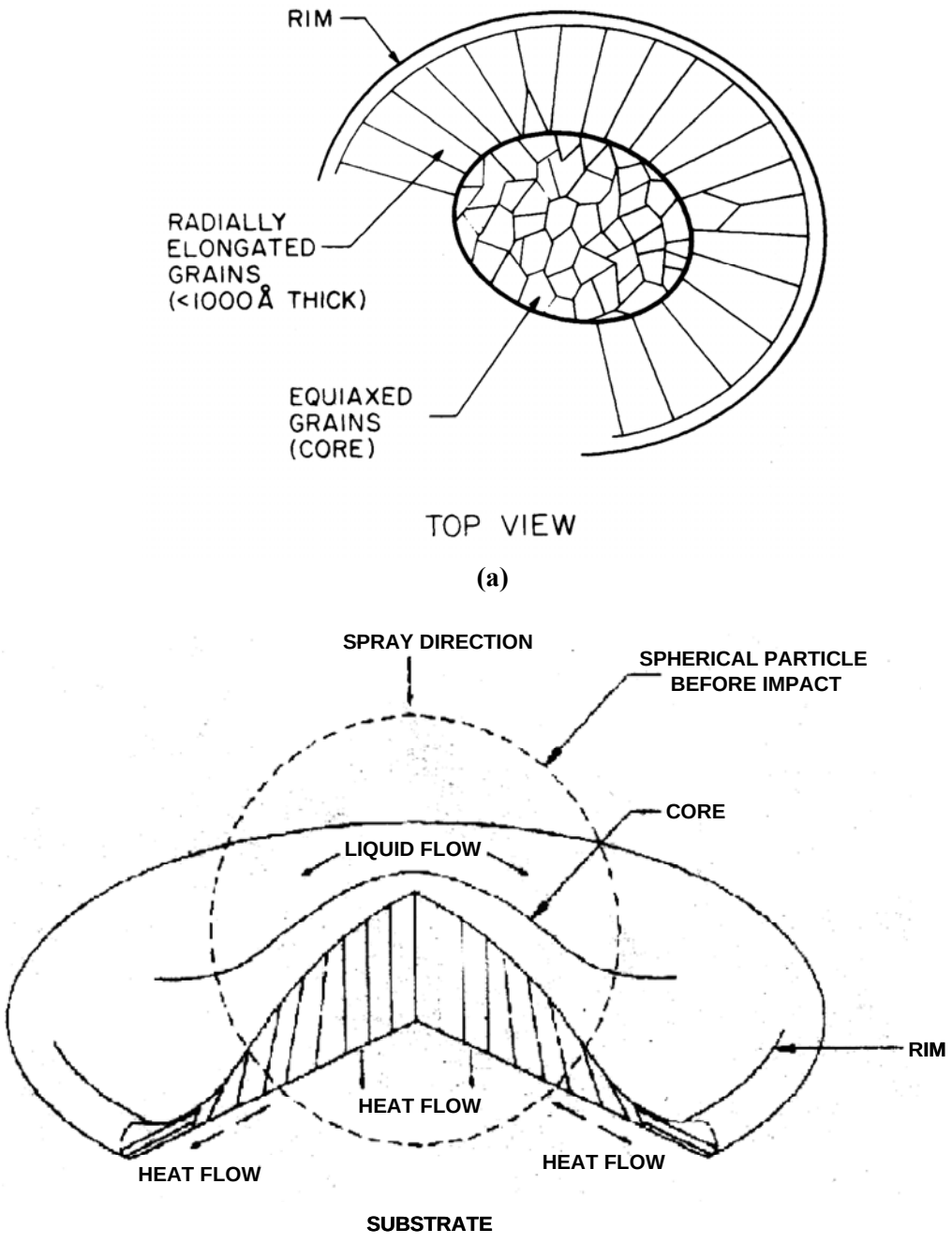

Figure 1-4 A typical crystallization of a plasma sprayed metallic splat: (a) Plannar morphology[81]; (b) Heat flow and related grain structure[82]

Jiang et al.[83] confirmed this argument by studying the grain morphology of molybdenum splats plasma-sprayed on hot glass substrates. In his study, the dendrite

grain growth direction has been characterized, which suggests that solidification is from the periphery of the molten splat inward, and solidification starts after the splat has reached its final diameter for this specific case.

Splat formation depends strongly on the impacting particle temperature and velocity. Other factors include the influence of oxidation on wetting properties and composition complexity, for example uniform composition and morphology or composite material, which affects heat propagation within the particle. Such parameters are linked to the spray technique used (flame, HVOF, RF or APS) and particle size. As soon as the particle temperature is close to, but below, the melting temperature, spreading requires a high impact velocity. Over melting temperature, the viscosity of liquid phase decreases rapidly with particle temperature, and the spreading requires much lower impact velocities.

Oxidation depends on the transport phenomenon controlling it. For particles with a temperature close to the melting temperature, oxidation is diffusion-controlled and occurs in a shell at the particle periphery. It is generally limited to a few oxide weight percent. On the contrary, for fully molten particles, it may be promoted by convection within the liquid droplet. This phenomenon is about one order of magnitude more than with diffusion. The latter occurs as soon as the velocity difference between the particle and the flame or the plasma jet is high enough to induce a particle Reynolds number higher than 20 and when the ratio of the kinematic viscosities of the plasma and molten particle is higher than 50[84]. In addition, the oxidation level is also a function of the oxygen entrained by the jet which (a) increases with the jet velocity, (b) diminishes with a shrouding gas, and (c) according to some authors, faster with atomic oxygen than with molecular oxygen. Atomic oxygen is essentially observed in DC air plasma jets flowing.

Sampath and Herman[82] reported that Ni splat prepared with VPS exhibits contiguous shape in contrast to fragmented splats prepared with APS. Bianchi et al.[85] compared the alumina splats morphologies prepared with direct current APS and RF plasma at reduced pressure environment. It was found that melting and adhesion are improved with RF torch. Ni-5 wt% Al deposits were produced with wire-arc spraying, APS, HVOF and cold spraying by Jiang and Sampath et al.[86]. Splats made with wire arc spraying and APS are fragmented, whereas splats produced with HVOF process are relatively contiguous.

Moore and Safai et al.[87, 88] reported one of the earliest studies on particle-impact phenomena for ceramic and cermets particles. Some correlations were found between spray parameters and the particle solidification process.

Fauchais, Fantassi, Bianchi and Vardelle and et al.[76, 89-92] systematically studied the influence of particle parameters at impact on zirconia splat formation and solidification in plasma spraying process. It was found that the droplet flattening time (inversely proportional to the cooling rate) decreases with the increase of the particle

velocity and temperature, whereas the splat-flattening ratio goes up with the increasing particle velocity and temperature. In addition, the relationship of flattening ratio and Reynolds number was found to agree quite well with Madejski's model. The flattening ratio was reported to decrease with increasing diameter of the impinging particles[93]. Jiang et al.[94] reported the increase of the fragmentation degree of plasma sprayed molybdenum particles with the increase of the particle kinetic energy. It was also demonstrated in Wright et al.[95]'s paper of plasma sprayed nickel that the fraction of unmelted particles increases with increasing velocity at low temperature and at higher temperatures the droplets break off and splash off the substrate. Benjan et al.[96] studied the relationship between droplet size, velocity and splash. Li et al.[54] carried out process map study to examine the role of process variables on the properties of deposit formed in thermal spray. In their study, a group parameter, melting index, was used to interpret the molten state of particles, which also reflected the thermal energy of the particles. The kinetic energy and fluidity of particles are characterized through their Reynolds number. Splat morphological features such as flattening and fragmentation were characterized against the group parameters.

It is widely accepted that the rate of oxidation depends on the individual rates of three consecutive phenomena: 1) the rate of mass transfer of oxygen from the gas phase to the particle surface; 2) the chemical rate of oxidation of the droplet; 3) the diffusion of the oxygen from the reaction surface of the particle to the interior. Vardelle et al.[97] have examined the factors influencing the relative magnitude of oxygen pick-up in the three stages of plasma spraying process, namely gas-solid phase oxidation during the initial preheating of the particles to their melting point, gas-liquid phase oxidation of the molten droplet in flight, gas-solid oxidation of the splat formed after impact of the particle with the substrate. It was highlighted that the oxidation occurs principally during the time of exposure of the splat to the hot gases surrounding the substrate, before they're covered by other impinging splats.

Wan et al.[78] have presented a model for oxidation of plasma sprayed molybdenum particles. It was demonstrated that the main oxidation mechanism for flying particle is the oxidant diffusion in gas phase when the particle is melted, and for a particle during deposition is the diffusion of metal/oxygen ion through a very thin oxide film. Espie et al.[98] have investigated the influence of APS process on the in-flight oxidation of pure iron particle. As indicated in their study, wusite is the only oxidation phase detected. This oxidation appears at the surface but also mainly in the core of the particles due to the strong convection with the droplets. FeO and dissolved oxygen represented respectively 12 wt% and 3 wt% of collected particles. Thus, an in-flight oxidation prediction model will have to integrate both convection and diffusion of oxygen in iron particles. It was also found that the dissolved oxygen in iron allows a better wettability on ceramic substrates.

1.4.2 Mathematical Simulation on Splat Formation

Complete modeling of coating formation process is difficult due to the fact that the phenomena taking place at impact have different reference times [99]. It takes about one to a few microseconds for splat flattening, 3 to 10 microseconds for splat solidification, one-tenth to a few milliseconds for layer or pass formation, and a few seconds to a few hours, depending on particle size, for next layer or pass formation. Moreover, most phenomena are cross-linked.

Splat flattening ratio (the ratio of splat diameter and droplet diameter) and fragmentation degree (a parameter used to describe the extent of break up of a splat, for rigid pan-cake shaped splats it equals to one) are two major quantities that have been linked to the formation of coating microstructure and properties. A number of numerical and analytical models have been developed to predict the splat-flattening ratio and the ultimate geometry of the splat based on the conservation of macroscopic mechanical energy.

Jones [99] pioneered the study of droplet cooling, freezing after impact on the substrate. His model predicted that the solidification time scale is much larger than the spreading time scale due to the contact thermal resistance and nucleation delay in non-equilibrium solidification. This suggests that solidification does not play a significant role in determining the eventual splat size. This argument is more significant for smaller droplet and high velocity such as those in thermal spray. Madejski[100] developed an analytical model of droplet spreading and solidification, allowing examination of splat flattening ratio. This allowed prediction of the splat flattening ratio. His model is expressed as:

$$\frac{3\xi_m^2}{We} + \frac{1}{\mathrm{Re}}\left(\frac{\xi_m}{1.294}\right)^5 = 1 \tag{1-1}$$

Here ξ_m, Re and We are the splat flattening ratio, Reynolds number and Weber number of droplet respectively. Madejski indicated that in his experiments with millimeter scale droplets, substrate materials have no effect on the flattening ratio.

As reviewed in the survey by Fauchais et al.[101], early studies have partially or completely neglected the material solidification and their models can be simply expressed as:

$$\xi_m = k\,\mathrm{Re}^a \tag{1-2}$$

with different values of k (from 0.8 corresponding to the mean diameter of an extensively fingered splat to 1.294 for disk-shaped splat) and a (from 0.125 to 0.2).

Recent studies have included solidification which can start even before flattening is complete. This will provide a more accurate estimation of the flattening process. Wan and Zhang et al.[102] showed that the solidification plays an important role in splat spreading for molybdenum deposition on various substrates. The time scale for

solidification is comparable to that of droplet spreading so that the solidification can arrest the droplet spreading. For partially stabilized zirconia droplets, solidification generally occurs after droplet spreading is complete and the effect of solidification on the flattening degree can usually be neglected. Their model is expressed as:

$$\left(\frac{\xi_m}{1.18}\right)^{2.5} = \sqrt{\mathrm{Re}}\left(\sqrt{\left(\frac{S}{2}\sqrt{\mathrm{Re}}\right)^2 + 1} - \frac{S}{2}\sqrt{\mathrm{Re}}\right) \tag{1-3}$$

where S is a non-dimensional solidification rate, can be expressed as [103]

$$S = \sqrt{\frac{2Ja}{\mathrm{Re}\,\mathrm{Pr}}\frac{k_s}{k_l}} \tag{1-4}$$

where Ja is Jakob number, $Ja = c_l(T_m - T_{sub})/L_m$, c_l is specific heat of the melt(J/kgK), T_m and T_{sub} are melting point of droplet material and substrate initial temperature(K), L_m is latent heat of fusion(J/kg), k_s and k_l are thermal conductivity(W/mK) of the melt and solid, respectively. Pr is Prandtl number, $Pr = \nu/\alpha$, ν is kinetic viscosity (m^2/s), α is thermal diffusivity of the melt (m^2/s). Substituting Eq. (1-4) into Eq. (1-3) gives

$$\xi_m = \left(\sqrt{\frac{Ja}{2\,\mathrm{Pr}}\frac{k_s}{k_l} + 1} - \sqrt{\frac{Ja}{2\,\mathrm{Pr}}\frac{k_s}{k_l}}\right)^{0.4}\left(1.18\,\mathrm{Re}^{0.2}\right) \tag{1-5}$$

Note that Eq. (1-5) has the same form as Eq. (1-2).

Wang and Robert et al.[104, 105] modified the 1-D calculations by considering nucleation processes. Recently Zhang et al.[106, 107] integrated a VOF-based fluid flow solver and solidification model to study splat formation and substrate melting. The influence of the substrate material, interfacial thermal contact resistance, and wettability on the nucleation, grain size distribution, and rapid solidification process has been investigated.

Raessi et al. [108] used a three-dimensional model of droplet impact and solidification to simulate the effect of surface roughness on the impact dynamics and the splat shape of an alumina droplet impinging onto a substrate. Simulations were run with and without considering solidification. By comparing the results, they have concluded that solidification plays a major role in determining splat shape on a rough surface.

1.5 Objective of This Dissertation

There has been growing interest in thermal spray processing of materials in the past years, with the existing applications widen and new applications explored. Many experimental and numerical studies are conducted in this area to understand the fundamental phenomena involved in this process and to optimize the operating

parameters for the improvement of the coating quality. However, such study is difficult since this process involves many physical phenomena and chemical reactions. Although the trial and error experimental method with proper post-sample analysis has provided a tool to understand the plasma and particle behaviors, it suffers from high cost, long cycle duration, and insufficient information that can be acquired. As the results, numerical simulation becomes a powerful tool to provide insights of physical and chemical processes occurring in the plasma jet and in-flight particles. It allows extensive studies of many issues such as particle size, velocity, and temperature and phase composition. In addition, evaporation and oxidation of the particles, which are among the major process concerns but difficult for experiment measurements, can also be studied with numerical method.

This dissertation is aimed at understanding the in-flight particle state and plasma plume characteristics in Air Plasma Spraying (APS) through the integration of experimental process diagnostic and three-dimensional numerical simulation. Key issues such as the phenomena of optimum particle injection angle and impact locations will be investigated through both experiment and numerical simulation. Through this investigation, guidance for optimizing plasma spraying process conditions will be obtained.

To relate process conditions to the particle in-flight state in a systematic and intelligent manner, 1st order global process maps will be developed and used to enable a universal description of particle state in thermal spray. Temperature (T)-Velocity (V) and/or Melting Index (M.I.)-Reynolds (Re) number will be used as measurements of thermal and kinetic energy of particles, respectively. Cross-comparisons amongst different spraying processes, such as Air Plasma Spray (APS), Twin Wire Arc (TWA) process, and High Velocity Oxygen Fuel (HVOF), and different materials, such as metals, ceramics, and cermets will be conducted in detail using the concept of global process maps. An additional group parameter, Oxidation Index (O.I), will be applied to relatively track the oxidation extent of metallic particles under different operating conditions. The new mapping strategies will also be proposed in circumstances where only ensemble particle diagnostics are available.

Chapter 2 Statement of the Problem

The process parameters required to produce tailored and reproducible coatings are usually specified in terms of controllable ones, which are associated with the spray equipment such as arc current, plasma gas composition, flow rate and spray distance. These parameters are typically determined based on experiment and/or experience. The easy-to-use optical sensors, which are recently developed based on the fundamental studies of the behavior of particles within the plasma jet and at impact[14, 76, 109, 110], are therefore very important for the purpose of process diagnostics.

The key thermal spray process control parameters and variables are shown in Figure 2-1. For a given particle morphology and size distribution, particle trajectory within the plasma jet determines particle thermal and kinetic energy at the point of impact with the substrate, which, in turn, controls the thermo-mechanical properties of the coating [85, 111]. Study of the effect of these key process control parameters is therefore very important for achieving high quality coatings rapidly.

Investigations presented in this thesis focus on the integration of the process diagnostics and numerical simulation for better understandings of particle in-flight status and its effect on the subsequent coating properties. This integration procedure is essential for providing science based guidance on the selection of process parameters to optimize particle in-flight status as well as splat and coating qualities. These concurrent and cross linked studies are discussed in the following sections.

2.1 Radial Injection of Particles into DC Plasma Jet

2.1.1 Injection Angle and Carrier Gas Flow Rate Effects on Particles In-Flight Characteristics

Experimental studies with in-flight sensors have shown the importance of injector geometry, injection method and carrier gas flow rate on the particle trajectory, which provides an additional dimension for the process control. To produce high quality coatings with desirable performance, optimization and control of thermal spray processes are necessary through improving the understanding of complex heat, momentum and mass transport phenomena in-between the plasma jet and the particles. Numerical simulation of the plasma spray process has received considerable attention during the last two decades, in particular the interaction between the in-flight particles and the plasma jet. Most simulations have been conducted in a two dimensional geometrical configuration. The effects of carrier gas flow and orthogonal particle injection were typically neglected because of difficulty in handling the complex three dimensional interactions between the carrier gas and the high temperature jet. However, the carrier gas flow injection not only enables the particle entrainment in the high-

temperature/high-velocity plasma jet, but at the same time, it disturbs the jet and affects the characteristics of in-flight particles behaviors. The understanding of carrier gas and particle injection effects on plasma jet and particle behavior is therefore desirable for control and design of plasma spray process as well as controlling the coating quality.

The goal of this study is to investigate the influence of particle injection angle on particle in-flight behavior and characteristics through an integrated modeling and experimental approach. Experiments were conducted to examine the characteristics of in-flight particles such as size distribution, temperature and velocity for the limited operating conditions. Numerical simulations have been carried out to systematically study the effect of injection angle on particle behavior under various carrier gas flow rates, and plasma jet perturbation by particle injection angle, carrier gas, and particle loading. The latter information is difficult to obtain from the experiments. Such an integrated analysis will be valuable to understand the effects on optimal design of plasma spraying process.

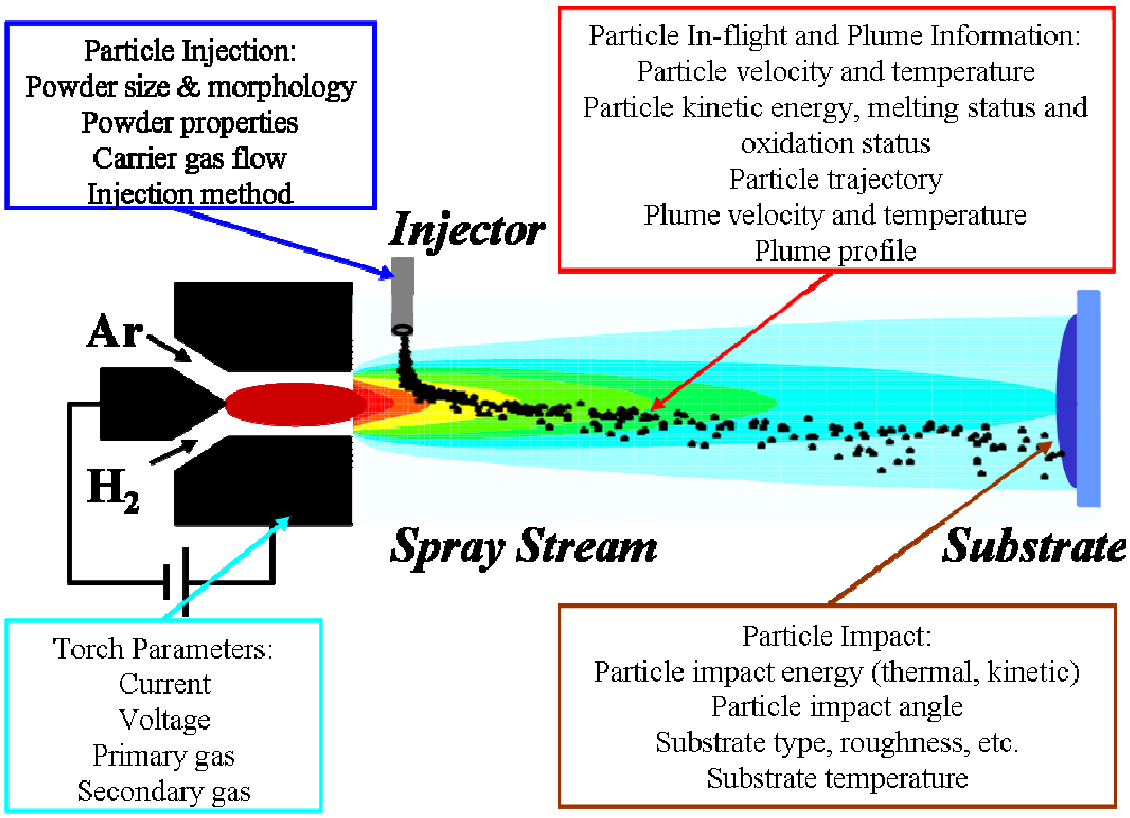

Figure 2-1 Typical thermal spray process control parameters and variables

2.1.2 Study of Plasma Forming Process Parameters Effect on Optimum Particle Injection ('Sweet Spot')

As mentioned in the previous part, apart from process parameters, particle injection has been found to play an important role on particle in-flight behavior, especially for the external orthogonal injection of less dense particles such as ceramics [72, 112, 113]. However, the initial hot zone of the plasma represents significant density and temperature gradients. External radial injection of particles into the plasma jet is complex primarily due to the variability in in-flight particle state resulting from trajectory based interaction of particles with the plasma. Various process and material aspects will influence particle injection. The plasma condition, injection location, angle of injection, carrier gas flow, and powder feed rate are some of the process attributes that influence particle injection.

Recent experiment have identified the existence of an optimum condition for injection based on the total spray stream intensity, which to a first approximation is an indication of the ensemble particle temperature [41]. The existence of this optimum condition has not been established across a wide range of process, injection and feedstock conditions that influence particle injection significantly. The basic criterion for the occurrence of the phenomena has not been completely explained. Whether the same injection condition results in simultaneously maximum heat and momentum transfer to particles remains to be understood. In-flight parameter to consistently identify optimum injection (based on achieving maximum in thermal and kinetic states of particle) that can be measured and controlled real-time has been established in CTSR (Center for Thermal Spray Research) at Stony Brook University. The influence of controlling injection based on the aforementioned optimum condition on the process downstream has not been studied systematically at every step in the process.

Even though experimental studies can provide a reasonable understanding of particle behavior under different process parameters at different spray distances, they fail to provide information on particle in-flight characteristics effects on plasma plume. Also, it is difficult to obtain acceptable data at closer spray distance directly from experiment [112, 113]. The behavior of particles in-flight at closer stand-offs could only be understood by simulations.

This goal of this study is to carry out systematic investigation to identify and quantify maximum average temperature and velocity at any given spray distance. Diagnostic tools such as IPP and SPT were used to measure the plume characteristics and ensemble temperature. DPV-2000 has been used to measure the distributions of individual particle characteristics such as temperature, velocity and size at the point of the maximum particle flux. Three-dimensional simulations were performed for the cases presented in the experiments. Specifically, the effects of carrier gas flow rate on the in-flight particle characteristics were studied at multiple stand-off distances.

Fundamental approach to optimize particle injection was also investigated through the integration of experiment and simulation by studying coupling effect of in-flight particle on plasma plume.

2.2 Generic Correlation of Spray Distance with In-flight Particle Behavior for Different Kinds of Materials

Significant efforts have been directed to understand the influence of process parameters (primary and secondary gas, plasma power) and their relationships with morphology and properties of molten particles upon impact, and eventual coating properties. Even though experiments have revealed the dramatic influence of spray distance on particles in-flight behavior and subsequent coating qualities[55, 114-117], understanding the correlation between spray distance and in-flight particle status for different feeding stocks is insufficient due to the following reasons: (1) Even though diagnostic sensors realized on-line monitoring and control of the particle in-flight behavior, stable and repeatable experimental data for multi-spray distances is still insufficient due to the time, feeding stock consumption and erosion of spray torches. (2) It is not safe to perform diagnostic experiments at a short spray distance (typically less than 50mm in APS). And (3) Direct measurement of particle molten status is difficult in the experiments, since the diagnostic sensors can only provide particle surface temperature. What is more, average particle surface temperature is not a good indicator for particle molten status, especially for ceramic particles. Recently, both experiment [53] and simulation [39] revealed that the statistical particle temperature distribution provided more information on particle molten status [11-13].

Approaches to optimize the plasma spray processes have been tried before via combining numerical simulations and experiments [70, 117-119]. In this dissertation studies have been carried out to further examine the statistical distributions of in flight particle characteristics for different kinds of materials in a systematical way. The correlations between powder properties and spray conditions will also be investigated in detail.

2.3 Representation of Particle In-flight Characteristics and Development of Global Process Map

Different strategies have been employed to meet the requirements for approximating the nature of the microstructure and sprayed coatings [47, 69, 120-122] with the help of diagnostic devices. The main objective of these devices is to measure the spray plume characteristics: namely the particle velocities, temperatures, trajectories and size distributions. They include measurement of *individual particle* parameters within the spray stream (e.g. Tecnar DPV 2000 and Inflight™ integrated particle sensor) as well as

ensemble particle sensors for group measurements of particle velocities and temperatures (e.g. Tecnar Accuraspray, Oseir Spraywatch, Inflight Particle Pyrometer etc.)[45, 47, 53, 123-125]. Many of these sensors measure particle temperatures through the use of thermal emission emanating from a molten/semi-molten traveling particle, and, use time-of-flight measurements to extract the particle velocities. Generally the velocity measurements can be measured with reasonable accuracy. However, the estimation of particle temperatures introduces inaccuracies as they rely on knowledge of emissivity of a material[45]. Furthermore, given the dynamic nature of the process, with associated gradients in chemistry and temperature within a given particle, true determination of particle temperatures continues to offer significant challenges. A direct measurement of particle melting status is extremely difficult since pyrometric technique only provides access to the particle surface temperature. For temperature measurements, the measured emission is principally from the surface of a particle and, in general, does not provide information on the bulk temperature of an entire particle. This is particularly important for widely used refractory ceramics, such as yttria stabilized zirconia (YSZ), due to its low thermal conductivity resulting in large temperature gradient along the radial direction. Most sensors measure temperature at a given location and does not take into account the in-flight time for a traveling particle. Given large differences in melting points, it is difficult to cross-correlate across a variety of materials systems.

In contrast to ceramics, oxidation is an important attribute of metallic particle in-flight behavior.[78, 126-128]. Not withstanding issues with coating properties, in-flight oxidation can affect diagnostic measurement itself due to changes in particle state. Furthermore, oxidation reactions are exothermic and can boost the metallic particle temperature well beyond the thermal spray imparted heating zone. Zhang et al derived a dimensionless parameter, *Oxidation Index(O.I.)*, to characterize the oxide content of the in-flight particles [73].

It is the author's intension in this thesis to examine and extend the applicability of these group parameters (Melting Index-*M.I.*, Reynolds Number-*Re*, Kinetic Energy-*K.E.* and Oxidation Index-*O.I.*) so as to enable a universal description of particle state (molten status, kinetic energy and oxidation status, respectively) in thermal spray. Both averages and distributions in the data will be analyzed and illustrated through the concept of 1st order process maps. Considerations will be further provided for multiple processes for ceramics and metallic alloys. And finally, approximations to the new mapping strategies will be proposed in circumstances where only ensemble particle diagnostics are available. Through this investigation, a universal method to represent particle in-flight characteristics will be obtained.

Chapter 3 Experimental Techniques and Mathematical Models

3.1 Diagnostics of Process

Integrated multi-sensor approach adopted at CTSR has been shown in Figure 1-3 in chapter 1. The demonstrated approach can not only enable closer look at the process but also facilitate cross-correlation of sensor data [53] and enhance the understanding of the sensors themselves as well as the process. Thorough understanding of the data from these different sensors combined with fundamental understanding of the process would lead to strategies to control the process using these sensors in a real-time or near-real-time manner.

3.1.1 Single Particle Measurements

The DPV 2000 (Tecnar Automation Ltd, Quebec, Canada) measures in-flight particle status (up to 4000 particles per second) by detecting the emitted thermal radiation from particles. Methods of measurement and details of instrumentation can be accessed in published documents [46, 129, 130]. A brief review of the principles is provided here. The measurement system (as shown in Figure 3-1) consists of a sensor head mounted on a XY displacement stage, an optical fiber cable and a detection unit containing photo-detectors and a computer.

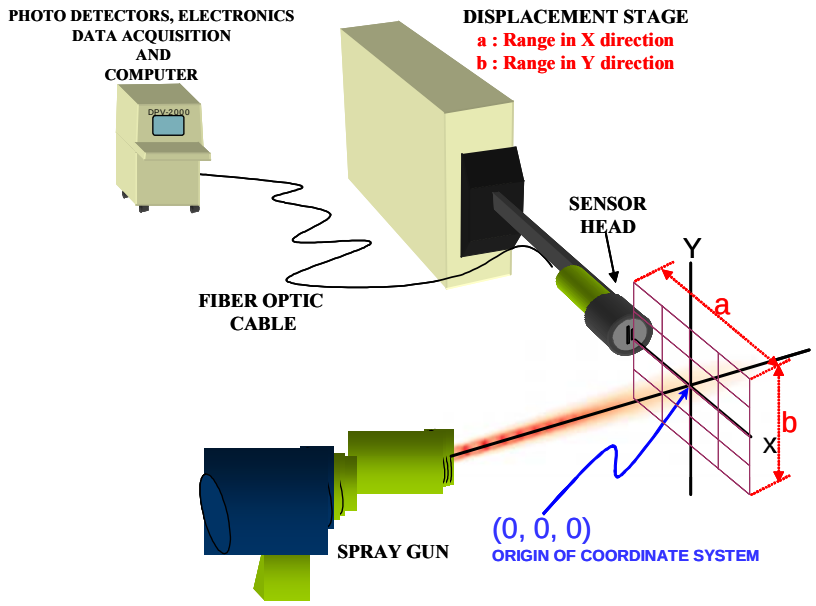

Figure 3-1Schematic of DPV 2000 and reference coordinate

As shown in Figure 3-2, when a particle passes in front of the sensor head, its image is formed on a two-slit mask fixed on the end of an optical fiber that guides the radiation to the detector unit. This transmitted radiation is split by a dichroic mirror and filtered through two bandpass filters. Two photo detectors located behind the filters are used to sense the transmitted radiation. The output of these detectors is amplified and the data is acquired through a digitizing board in the computer. These two-peak signals are used to calculate the particle velocity and temperature. The particle velocity is calculated from knowing the optical magnification, distance between slits and the time of flight from two-peak signal. Temperature of the particle is calculated from the ratio of radiation intensities collected at 1000 and 790 nm (the two bandpass filter center values). Particle size is estimated from absolute intensity of radiation at 790 nm. Although the principle of measurement of temperature is independent of the emissivity due to the use of two-wavelength pyrometry (assuming the particle to be gray body), the total intensity emitted and measured is a function of the emissivity that is material and temperature dependent. More information on the sensor can be found in references [46, 129, 130].

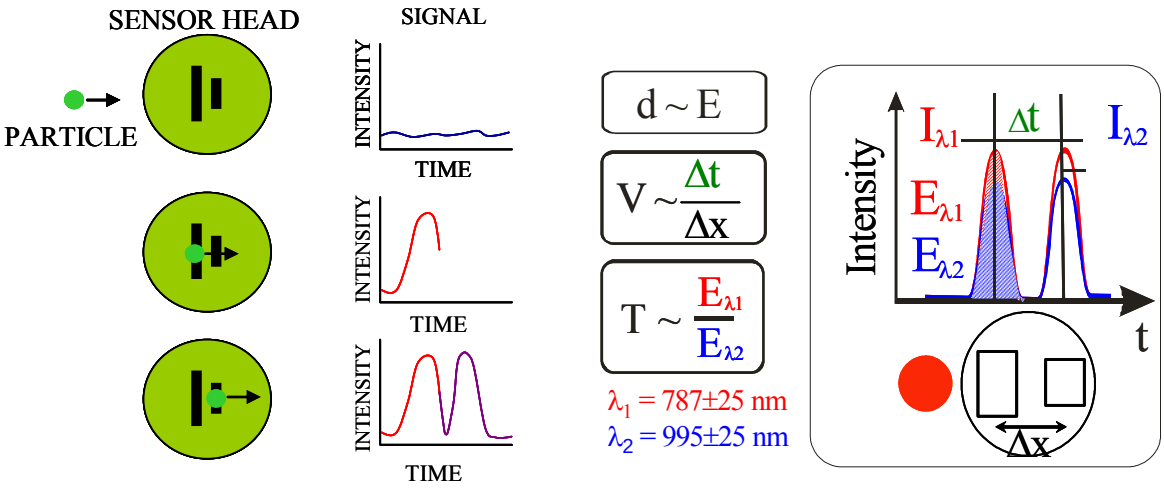

Figure 3-2 Principle of measurement of DPV 2000

In order to attain a fixed coordinate system for all measurements and to yield maximum flexibility with the data acquisition procedure, the DPV Sensor head was aligned as described below. The sensor orientation was kept orthogonal to the spray stream and the optical fiber array was also aligned to be perpendicular to the spray direction as shown in Figure 3-1. The center of the range of movement of the XY displacement stage (0, 0) was coincident with the axis of the anode at a fixed stand off distance (for example, 100 mm). This point was taken as origin (designated as (0,0,0) point in the figure) and the robot was programmed with this location as its reference.

Usually there are two types of measurements – *single point measurement* at the autocenter (1D CCD array in between the two slits detects the location of maximum intensity in the plume which is called autocenter position) and *scan* in the form of a programmable grid superimposed on the limited X-Y plane (Figure 3-1). The scan, preferably in the form of a square, can cover as much as 110 mm x 110 mm in the X-Y plane symmetric to the torch axis. This distance depends on the X-Y controller available and on the focus of the optics. Typically data is acquired from more than 10,000 particles in single point measurement (to reduce random error and improve statistical reliability) and about 300 particles at each spot during the scanning process.

3.1.2 Ensemble Measurements

The measurement of spray stream as an ensemble can be carried out by recording the total incandescence of the spray stream. This technique has been utilized to estimate the temperature and centroid position in the Torch Diagnostic System (Inflight Ltd, Idaho Falls, ID, USA). This system comprises of two sensors – the Spray Position and Trajectory (SPT) and In flight Particle Pyrometer (IPP). The SPT is a line scan camera that images the spray stream on a linear CCD array and then analyzes the image to obtain width of the distribution and also its centroid. The IPP (pyrometer) is a two color pyrometer specially engineered to be used in the thermal spray booth environment. It has a nearly cylindrical measuring volume within which the spray stream measurements are made. By analyzing the emitted radiation from an ensemble of particles, an average temperature of the spray plume is measured. Further instrument details have been described in the literature [131-133]

Instrumentation and the setup of sensors are depicted in Figure 3-3. In order to compare data across different sensors, the same coordinate system has been used as that for DPV 2000. The IPP has a working distance of about 200 mm and was mounted on the 'Y' axis. It is important to note that the IPP has a cylindrical volume of measurement which is about 50 mm in length and 5 mm in diameter. Due to this, optimally, the IPP needs to be mounted in a way that the line of sight of the instrument is nearly perpendicular to the torch axis and also, the sensor is located in a plane defined by the injector and the nozzle axis. By following this guideline, there is minimal chance of the spray stream going completely out of the field of view of the sensor due to a change in the carrier flow.

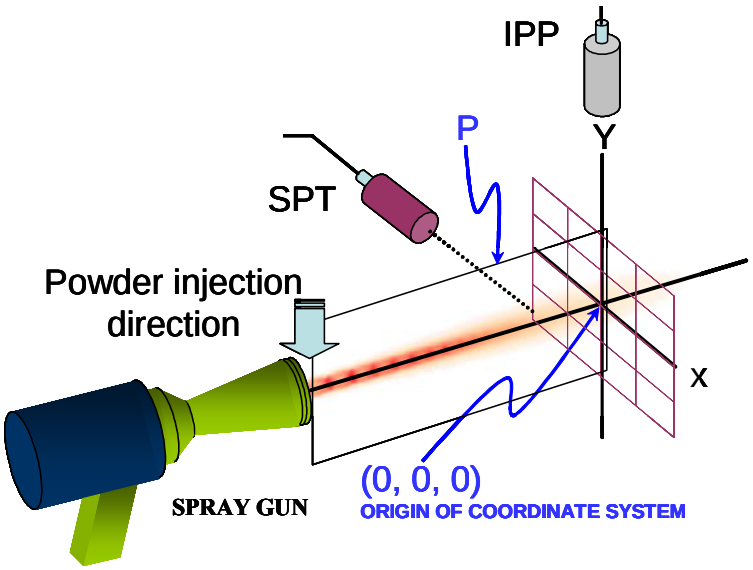

Figure 3-3 Schematic of the TDS system composing of IPP and SPT

Accuraspray is another ensemble sensor in the integrated sep-up, as shown in Figure 3-4. In operation, the sensor head is aimed at the plasma plume from a distance of 200 mm and the parameters that can be measured include average particle temperature and velocity, position and width of plasma plume, and internal sensor head temperature. Values of all these parameters are continuously recorded, displayed and compared on the screen.

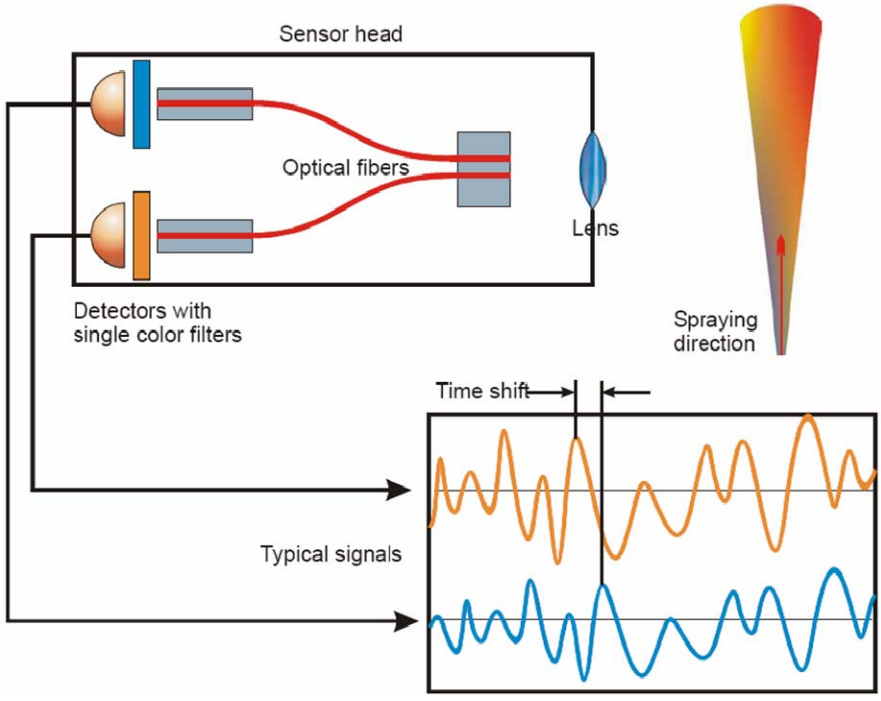

Figure 3-4 Particle temperature and velocity measurement principle for Accuraspray

As shown in Figure 3-4, accuraspray features a dual fiber optical device that "sees" the flow of particles at two different points along the spray stream. The signal from the down-stream detector is very similar to the first one but delayed in time because it comes from the same particles detected a few millimeters apart. This simple and time-shift cross-correlation yields a very precise measurement of the time delay from which the velocity can be calculated since the gap between the measuring points is a precisely known constant. In addition, the detectors are filtered at two different colors allowing the mean particle temperature to be measured using the very well known twin wavelength pyrometry principle (assumes that the emissivity of the particles is the same for the two wavelengths). One advantage of this method is that the value of the cross-correlation (between 0 and 1) gives an indication of the validity of the temperature measurement. A strong correlation between the two signals (above 0.6, for example) means that the two detectors are seeing the same particle population which is essential for the twin wavelength pyrometry to work properly.

The actual integrated diagnostics sensor set up has been shown in Figure 3-5. Meanwhile, Table 3-1 lists the cooperation of multiple sensors. To accommodate the different sensors from the spray torch, all the sensors can not be located to view (0 0 0) simultaneously. Instead, as shown in Figure 3-1, the Accuraspray is mounted to view point (0 0 -30), IPP and SPT to view (0 0 0) simultaneously (to realize on-line control of injection [58]) and DPV 2000 to view (0 0 30). When the long duration DPV measurements are being made, simultaneous measurements with the SPT / IPP can be made at a spray distance closer by 30mm. By moving the spray torch along the y axis as shown in Figure 3-1, the sensor coordinates can be translated to compare data from multiple sensors for the same spray distance. This integrated diagnostic sensor set-up provides redundancy, complementary data acquisition and the opportunity to cross correlate data from different instruments.

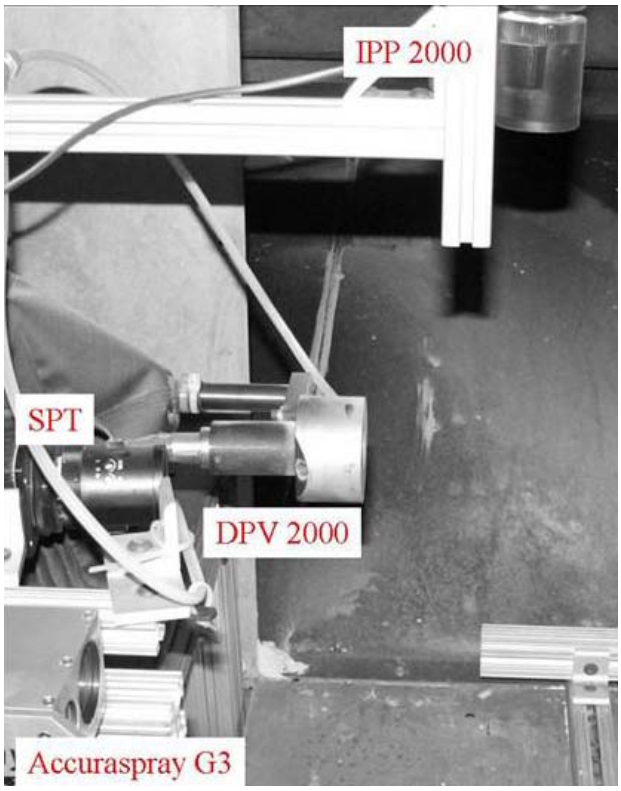

Figure 3-5 Picture of integrated sensor set up at CTSR

Table 3-1 Sensors presently used at CTSR: Principle, procedure and information obtained [54, 134]

Sensor	Capability	Principle	Location of Data Acquisition	Information from data
DPV 2000	Individual particle	Two-wavelength pyrometry and time of flight	Plume flow center at SD (Single Point)	Distribution and Average of T, V and D
			Grid of points across the plume at SD (Scan)	T, V and D at each point in the scanning grid
SPT	Ensemble	Line intensity imaging	1D section of the plume orthogonal to nozzle axis at SD	Plume intensity profile including central point and peak width
IPP	Ensemble	Two-wavelength pyrometry	3D volume at SD	Average ensemble T
Accuraspray	Ensemble	Two-wavelength pyrometry	3D volume at SD	Average ensemble T, V and plume intensity profile including central point and peak width

3.2 Mathematical Model for Plasma Flame and Particle-Flame Interaction

3.2.1 Plasma Flame

The simulation for DC plasma plume needs to take various physical and chemical phenomena into consideration. The plasma jet formed after the plasma source is expelled out of the plasma torch. At the fringes of the plasma jet downstream, large scale eddies will be developed because of the shear stress, which leads to the transition to the unstable turbulent flow. The mass, momentum and energy transports of the plasma jet are greatly influenced by the turbulence. Chemical reactions also need to be considered in this high-temperature multi-species gas, all of which make the modeling more complex.

The modeling of DC arc formation is reported in many studies during the last two decades, which include the arc formation in the electrode region as well as the transition from the plasma to the electrode surface. One of the challenges is the description of the phenomena at the anode wall. This description has to be dynamic and three-dimensional and includes numerous parameters affecting the arc–anode interaction.

Since the modeling of arc formation is complex and the result is not reliable, most simulations of plasma jet start from the results of calculating temperature and velocity distributions at the nozzle exit matching with the plasma gas flow rate and enthalpy:

$$v(r,0) = V_{cl}\left[1-(r/R_i)^m\right] \tag{3-1}$$

$$T(r,0) = (T_{cl}-T_w)\left[1-(r/R_i)^n\right]+T_w \tag{3-2}$$

where R_i is the torch nozzle exit radius. Parameters V_{cl}, m, T_{cl} and n are selected to match the known flow rate of cold plasma gas and the power supplied into the plasma torch as closely as possible. In this dissertation, the expression from Chang [31] was used, which has already been validated with experiments [135]. For example, for the flow rate (Ar/H_2 plasma gas) of 40/7 cm^3/s and the net power of 19.52 kW, the values of V_{cl}, m, T_{cl} and n are 2560.23 m/s, 1.2, 12988 K and 6, respectively.

3.2.1.1 Plasma Jet

The governing equations for the DC plasma jet consist of the following several parts: continuity, momentum and thermal energy equations for the multi-component fluid mixture, species equations for each component of the mixture taking into account the mixing with the surrounding atmosphere, state relations for an ideal gas mixture with temperature-dependent specific heat, enthalpy and transport properties, and so on. The governing equations can be represented as the followings:

Continuity equation:

$$\frac{\partial \rho}{\partial t} + \nabla \cdot (\rho \vec{u}) = 0 \tag{3-3}$$

Species equations:

$$\frac{\partial \rho_i}{\partial t} + \nabla \cdot (\rho_i \vec{u}) = -\nabla \cdot \vec{J}_i + \dot{\rho}_i^c \tag{3-4}$$

where ∇ is the vector differential operator in cylindrical coordinate, J_i is the diffusion mass flux, the subscript i represents different species, and $\dot{\rho}_i^c$ is the rate of change $\dot{\rho}_i$ due to chemical reactions. J_j is the diffusion mass flux of species j, which is determined by a self-consistent effective binary diffusion approximation [136], and represented as:

$$J_j = -cM_j D_j \nabla\left(\frac{\rho_j}{M_j c}\right) + \left(\frac{\rho_j c}{\rho}\right) \sum_i M_i D_i \nabla\left(\frac{\rho_i}{M_i c}\right) \tag{3-5}$$

Momentum equation:

$$\frac{\partial(\rho \vec{u})}{\partial t} + \nabla \cdot (\rho \vec{u} \vec{u}) = -\nabla\left(p + \frac{2}{3}\rho k\right) + \nabla \cdot \vec{\sigma} + F \tag{3-6}$$

where F represents the momentum source or sink due to the injected particles, k is the turbulent kinetic energy per unit mass, and $\vec{\sigma}$ is the viscous stress matrix. The viscous stress can be represented by:

$$\vec{\sigma} = (\mu + \mu_t)\left[\nabla \vec{u} + (\nabla \vec{u})^T\right] + (\lambda + \lambda_t)\nabla \cdot \vec{u}\mathrm{I} \tag{3-7}$$

where μ is the viscosity, μ_t is the turbulence viscosity, I is the unit matrix,

$$\lambda = -2\mu/3 \tag{3-8}$$

$$\lambda_t = -2\mu_t/3 \tag{3-9}$$

Thermal energy equation:

$$\frac{\partial(\rho e)}{\partial t} + \nabla \cdot (\rho e \vec{u}) = -p\nabla \cdot \vec{u} - \nabla \cdot \vec{q} + \rho\varepsilon + \dot{Q}_c - \dot{Q}_R + \dot{Q}_p \tag{3-10}$$

where $\vec{q}$ is the heat flux vector, ε is the viscous dissipation rate, $\dot{Q}_c$ is the rate of change of ρe due to chemical reactions, $\dot{Q}_R$ is the heat loss rate due to radiation, and $\dot{Q}_p$ is the heat source or sink due to injected particles.

The heat flux vector, $\vec{q}$, contains contributions from both pure heat conduction and species diffusion, which is given by:

$$\vec{q} = -K\nabla T + \sum_j h_j \vec{J}_j \,. \tag{3-11}$$

3.2.1.2 Chemical Reactions

Chemical reactions such as ionization, dissociation, recombination and so on taking place in the plasma jet can be treated using a general kinetic algorithm. Partial

equilibrium has been assumed in which fast reactions are considered to be in equilibrium while slower ones proceed kinetically [40]. The chemical reaction *S* can be symbolized by:

$$\sum_i a_{is} X_i \Leftrightarrow \sum_i b_{is} X_i \tag{3-12}$$

Where X_i represents species *i*, a_{is} and b_{is} are stoichiometric coefficients for reaction *S*. The mole density ρ_i^c can be described by:

$$\rho_i^c = M_i \sum_s (b_{is} - a_{is}) \omega_s \tag{3-13}$$

Where M_i is the molecular weight for species *i*.

Kinetic reactions

The kinetic chemical reactions proceed at a rate of ω_s can be presented as:

$$\omega_s = k_{fs} \prod_i (\rho_i / W_i)^{a'_{is}} - k_{bs} \prod_i (\rho_i / W_i)^{b'_{is}} \tag{3-14}$$

where reaction orders a'_{is} and b'_{is} are not necessarily equal to a_{is} and b_{is}, so that empirical reaction orders can be used. The coefficients k_{fs} and k_{bs} are determined by Arrhenius equation:

$$k_{fs} = A_{fs} \exp(-E_{fs} / T) \tag{3-15}$$

$$k_{bs} = A_{bs} \exp(-E_{bs} / T) \tag{3-16}$$

Equilibrium reactions

The progress rate for chemical reaction is calculated by an implicit scheme, and one kind of solution is using the equilibrium constant:

$$\prod_i (\rho_i / M_i)^{b_{is} - a_{is}} = K_s(T) \tag{3-17}$$

where K_s can be determined for every chemical reaction in such fashion as:

$$K_p = B_p T^{n_p} \exp(Q_{k,ref} / RT) \tag{3-18}$$

in which, $B_p = \exp\left(\sum_i (b_{is} - a_{is}) \pi_{Ai} \right)$, $n_p = \sum_i (b_{is} - a_{is}) \pi_{Bi}$ and $Q_{k,ref} = \sum_i -(b_{is} - a_{is}) H_{i,ref}$

3.2.1.3 Boundary Conditions

Boundary conditions at the nozzle inlet of inflow

Mass fractions of argon and hydrogen gas are given, and the temperature and axial velocity are estimated from $\tilde{v}(r,0) = V_{cl}\left[1 - (r / R_i)^m\right]$ and $\tilde{T}(r,0) = (T_{cl} - T_w)\left[1 - (r / R_i)^n\right] + T_w$, where the parameters V_{cl}, m, T_{cl} m and n are selected to match the known flow rate and the power supplied to the plasma torch;

Boundary conditions at the torch wall

The temperature is estimated from $\widetilde{T}(r,0) = 700 - 400\ln(r/R_{in})/\ln(R_{out}/R_{in})$, the velocity components in r and y directions are zero, and $\partial\phi/\partial y = 0$ is applied to ϕ, representing the temperature and energy;

Boundary conditions at the open boundaries

The values of temperature and pressure are assigned the same as that in ambient for inflow, while $\partial\widetilde{\phi}/\partial y = 0$ for outflow;

Boundary conditions at the symmetric axis (r=0)

The values of each parameter, ϕ, is determined according to the immediate neighborhood point in the following format,

$$\phi\big|_{r=0} = \left(\sum_{i=1}^{N}\phi_i\right)/N(\phi = u, v, T), \qquad \text{and} \qquad w = 0 \tag{3-19}$$

where ϕ_i (i = 1, 2, ….N) are the values of ϕ at locations with the distance Δr from the centerline. The specification of the boundary conditions for all other scalar parameters is the same as that for temperature.

Boundary conditions at the circular direction, Z

The periodic boundary condition is used:

$$\phi(x, y, 2\pi) = \phi(x, y, 0). \tag{3-20}$$

Source terms of carrier gas and injected particles

The source terms of carrier gas is added in the governing equations of species, momentum and energy at the cells of the injector resided. The size of the injector is very small with the diameter of 1.8 mm, and its effect on the plasma jet is negligible.

The calculations are initialized from the cold air and then mixed with the incoming jet until the steady state can be reached. The steady state solution is expected to be unique and independent of the initial conditions. For the Ar / H_2 plasma, to avoid the attachment between the arc and the anode, a swirl velocity is usually introduced. To save the computation time, this effect is not considered here in calculation.

3.2.2 Interaction between Particles and Plasma Flame

The mathematical models for the particle physical and chemical phenomena will be presented in this section. The computational particles are created at the spot of injection and tracked throughout their flights. The solution of the plasma gas provides the information on the conditions external to the particles. The injected particles have been treated in a Lagrangian coordinate. The effects of the particles loading effects on the plasma plume have also been considered.

When the particles fly through the plasma flame, the mass, momentum and energy transfer from the flame will dramatically change the particle properties. These transport

phenomena include particle acceleration, heating and melting, evaporation and the metal particle oxidation, and so on.

To trace the in-flight particles individually the Lagrangian approach has been used. Particle acceleration and heating are tracked after injection in which the drag force by plasma flame and the heat transport on the particle surface are considered. For heat transfer, some effects specific to thermal plasma environment need to be considered. The main effects are due to the high temperature gradient prevailing in the boundary layer surrounding the particles, varying plasma properties, non-continuum conditions, thermophoresis, turbulent dispersion, evaporation and possible chemical reactions on the particle surface. Some of the particle-plasma interaction models are listed in detail as follows.

3.2.2.1 Particle Acceleration Model

The driving forces on a particle immersed into a plasma plume include the viscous drag, the pressure gradient and gravitational force. Since the drag force is the only prominent one that affects the particle momentum transfer significantly for the particle size of smaller than 100 μm in plasma jet, the momentum transfer between the particle and plasma jet can be represented as:

$$F_p = m_p \frac{d\vec{V}_p}{dt} \quad , \tag{3-21}$$

$$\frac{d\vec{V}_p}{dt} = \frac{3}{8}\frac{\overline{\rho}}{\rho_p}\frac{C_D}{r_p}\left|\tilde{\vec{V}} + \vec{V}' - \vec{V}_p\right|\left(\tilde{\vec{V}} + \vec{V}' - \vec{V}_p\right) , \tag{3-22}$$

where $\vec{V}'$ is the turbulence velocity fluctuation. The coefficient C_D for the drag force can be expressed as [63]:

$$C_D = \frac{24}{\mathrm{Re}_p} + \frac{6}{1+\sqrt{\mathrm{Re}_p}} + 0.4, \qquad \text{for } \mathrm{Re}_p < 100 \tag{3-23}$$

Or, in some work, the drag coefficient is:

$$C_D = \begin{cases} \dfrac{24}{\mathrm{Re}_p} & for \quad \mathrm{Re}_p < 1 \\ \dfrac{24}{\mathrm{Re}_p}\left(1 + 0.15\,\mathrm{Re}_p^{0.687}\right) & for \quad 1 < \mathrm{Re}_p < 10^3 \\ 0.44 & for \quad \mathrm{Re}_p > 10^3 \end{cases} . \tag{3-24}$$

Reynolds number is defined as:

$$\mathrm{Re}_p = \frac{\rho_f D_p \left|\tilde{V} + V' - V_p\right|}{\mu_f} \tag{3-25}$$

where D_p is particle diameter, ρ_f and μ_f are the mean density and viscosity of gas phase around the particle, respectively.

3.2.2.2 Lumped Heat Capacity Model

For the cases in which particle temperature can be assumed as uniform, the energy conservation equation can be expressed as:

$$m_p C_p \frac{dT_p}{dt} = \pi D_p^2 \dot{q} \qquad \left(for \quad T_p \neq T_m\right) \tag{3-26}$$

$$m_p L_m \frac{d\chi_p}{dt} = \pi D_p^2 \dot{q} \qquad \left(for \quad T_p = T_m\right) \tag{3-27}$$

where χ_p is the melt fraction of the particle, and $\dot{q}$ is the heat flux at the particle surface.

3.2.2.3 One-dimensional Model with Heat Conduction

If the Biot number (*Bi* defined as hr_p/K_p) related to particles is higher than 0.1 for ceramic material and large particles, the heat transfer in the particle has to be taken into consideration, because the temperature gradient within the particles can be large. Therefore, a one-dimensional model for particle heating and melting is used in which a spherical shaped particle is assumed and internal convection within the molten part of the particle has been neglected. Figure 3-6 shows the geometry and the heat transfer between the particle and flame environment.

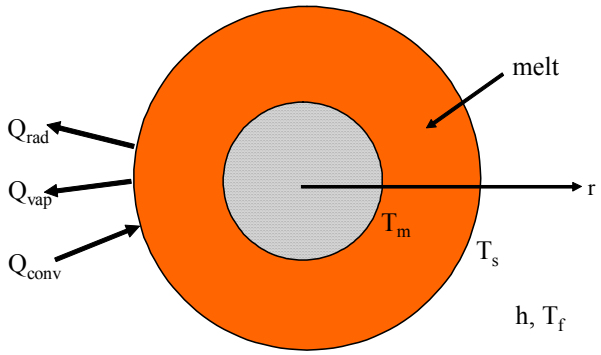

Figure 3-6 Schematic of particle heat transfer

Temperature distribution inside the particle can be described by heat conduction as the followings,

$$\rho_p C_p \frac{\partial T_p}{\partial r} = \frac{1}{r^2}\frac{\partial}{\partial r}\left(K_p r^2 \frac{\partial T_p}{\partial r}\right), \tag{3-28}$$

where the subscript p represents the particle and the properties ρ_p, C_p, and K_p are taken as local values. The boundary conditions for a particle with melting interfaces are given below,

$$\left.\frac{\partial T_p}{\partial r}\right|_{r=0} = 0 \ , \tag{3-29}$$

$$\left.\left(K_p \frac{\partial T_p}{\partial r}\right)\right|_{r=r_m^-} - \left.\left(K_p \frac{\partial T_p}{\partial r}\right)\right|_{r=r_m^+} = L_m \rho_p \frac{dr_m}{dt}, \tag{3-30}$$

$$4\pi r_p^2 \left.\left(K_p \frac{\partial T_p}{\partial r}\right)\right|_{r=r_p} = \dot{q} \ . \tag{3-31}$$

For the cases when resolidification occurs, an additional constraint has to be applied to the resolidification interface,

$$\left.\left(K_p \frac{\partial T_p}{\partial r}\right)\right|_{r=r_s^+} - \left.\left(K_p \frac{\partial T_p}{\partial r}\right)\right|_{r=r_s^-} = L_m \rho_p \frac{dr_s}{dt} \ . \tag{3-32}$$

The melting condition can be either considered as equilibrium or non-equilibrium. If an equilibrium melting or resolidification happens, the interface temperature can be assumed to be the melting temperature:

$$T_p\Big|_{r=r_m,\ r_s} = T_m \tag{3-33}$$

Otherwise for non-equilibrium melting, there is superheating and the interface movement is related to interface temperature, T_i, by:

$$\frac{dr_m}{dt} = \mu_k \left(T_m - T_i\right) \tag{3-34}$$

where μ_k is the linear kinetic coefficient, for example, the values of μ_k for molybdenum and zirconia are 0.23 and 0.01 m/s-K according to Wang [137]. For the non-equilibrium solidification the consideration is similar to melting.

In the above energy conservation models, the heat flux at the particle surface can be expressed as following,

$$\dot{q} = \dot{Q}_{conv} - \dot{Q}_{vap} - \dot{Q}_{rad} \tag{3-35}$$

$$\dot{Q}_{conv} = 4\pi r_p^2 h\left(\widetilde{T}_f - T_s\right) \tag{3-36}$$

$$\dot{Q}_{vap} = \dot{m}_v L_v \tag{3-37}$$

$$\dot{Q}_{rad} = 4\pi r_p^2 \varepsilon_p \sigma\left(T_s^4 - \widetilde{T}_\infty^4\right) \tag{3-38}$$

Considering heat transfer by convection, evaporation and radiation the heat transfer coefficients is calculated from:

$$h = \frac{k_f Nu}{2r_p} \tag{3-39}$$

$$Nu = 2.0 + 0.6\,\mathrm{Re}_p^{1/2}\,\mathrm{Pr}^{1/3} \tag{3-40}$$

In equation (3-36) $\widetilde{T}_f$ is the film temperature defined as the average value of gas temperature at the cell where the particle is located. At the immediate vicinity by the particle surface:

$$\widetilde{T}_f = \left(T_c + T_w\right)/2\,. \tag{3-41}$$

It is worth to mention here that for simplification spherical shaped particles has been assumed in this simulation. However, particle morphology does affect the flowability especially for the angular shaped ones. [138]

3.2.2.4 Particle Effects on Plasma Flame

Most of the recent models for the particle-plasma interaction assume that the effects of loaded particles on the plasma jet are negligible. However, this is not the case in practice, especially when the particle feeding rate is high. Also, the small amount of injected particles can have a great influence on the plasma turbulence structure. Recently, some models have been proposed for the two-way interaction of the particle and plasma jet. Ramachandran and Nishiyama [139, 140] developed a three-dimensional model considering the two-way interactions of energy, momentum and turbulence between the plasma flame and the injected particles.

In the model used in this dissertation, the effect of plasma cooling by the injected particles is incorporated, by considering the source terms of heat and momentum for coupling the particle phase to the gas phase equations. The particles in the LAVA code are considered as discrete Lagrangian entities that interact with the plasma gas. Each computational particle represents a group of similar real particles and it is stochastically generated by sampling from the probability distributions of the particle size, velocity and its direction at the injection nozzle.

For coupling the particles and gas phases, the exchange terms of momentum F_p and heat $\dot{Q}_{conv}$ and $\dot{Q}_{rad}$ must appear with the opposite sign in the fluid dynamical equations for the plasma gas. For this purpose, it is necessary to sum over all particles in the corresponding computational cell. Therefore, the source terms due to injected particles in the governing equations of plasma jet are defined as:

$$F = -\frac{1}{\alpha V_{cell}} \sum_P N_p F_p \tag{3-42}$$

$$\dot{Q} = \frac{1}{\alpha V_{cell}} \sum_P N_p \left[4\pi r_p^2 h\left(T_s - \widetilde{T}_f\right) + F_p\left(\vec{\widetilde{V}} + \vec{V}' - \vec{V}_p\right)\right] \tag{3-43}$$

$$\dot{W} = -\frac{1}{\alpha V_{cell}} \sum_P N_p F_p \vec{V}' \tag{3-44}$$

In which α is the volume percentage of particles in the computational cell, N_p is the number of particles in the computational cell and V_{cell} is the volume of the computational cell, m^3.

3.2.3 Computational Domain and Mesh

Solution to the above equations is performed by using the program Lava-3D-P [39, 141]. The computational domain, mesh, and some of the boundary conditions used in the plasma jet calculation are shown in Figure 3-7.

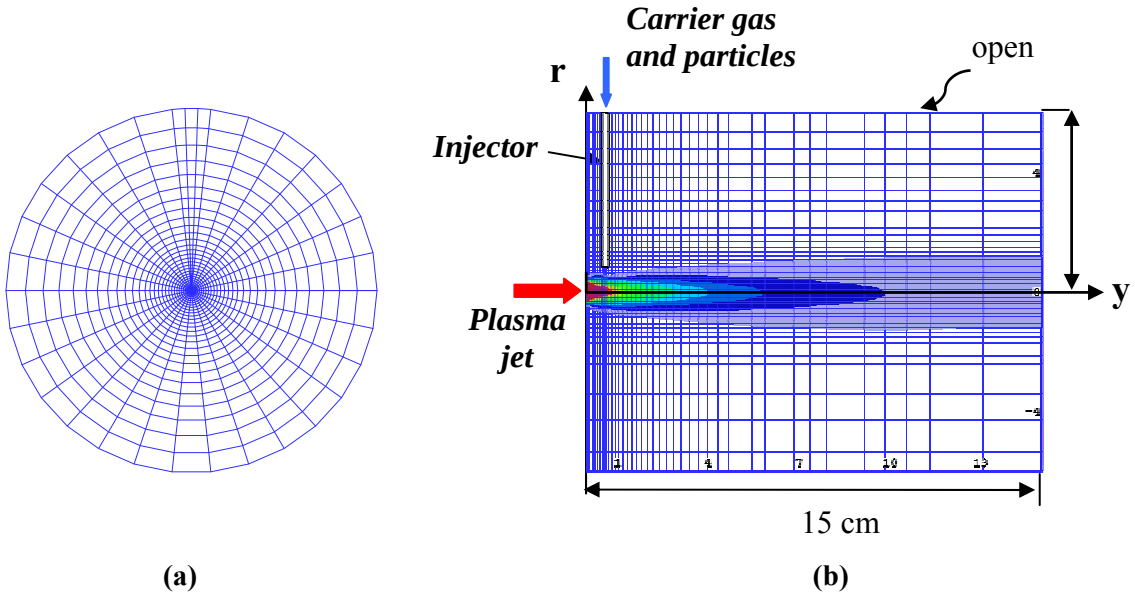

Figure 3-7 Geometry and computational mesh in: (a) cross-section plane normal to the plasma jet, and (b) middle section plane of 3D plasma jet

3.2.4 Stochastic Scheme of Multiple Particle Generation

The method for solving particle generation is based on the ideas of Monte Carlo method and discrete particle method [142]. The particles are created by sampling randomly from assumed probability distributions that govern particle properties at injection, *i.e.*, position, size and velocity. Given the distribution function $f(x)$ corresponding to the random variable x $(x1 \le x \le x2)$, such as shown in Figure 3-8, the number of particles in the interval dx about the value x, is given according to distribution function $f(x)$:

$$dN = f(x)dx \tag{3-45}$$

The random variable, P, is defined as $P(x) = \int_{x_1}^{x} f(x')dx'$. It should be noted that $N(x) = P(x)$. Hence, the number of particles is uniformly distributed with respect to the variable $P(x)$. Usually the random number generator has a uniform distribution in

the range from zero to one. Therefore, if we sample from the given distribution of x, and scale it by $\int_{x_1}^{x_2} f(x)dx$ to obtain $P(x)$:

$$P(x) = \frac{\int_{x_1}^{x} f(x')dx'}{\int_{x_1}^{x_2} f(x)dx} \qquad and \qquad P(x) \in [0,1] \tag{3-46}$$

X can be obtained by inverting the random number P, and the particle size is therefore distributed according to $f(x)$. In this dissertation, the particle size distribution for simulation has been set the same as that used in experiment.

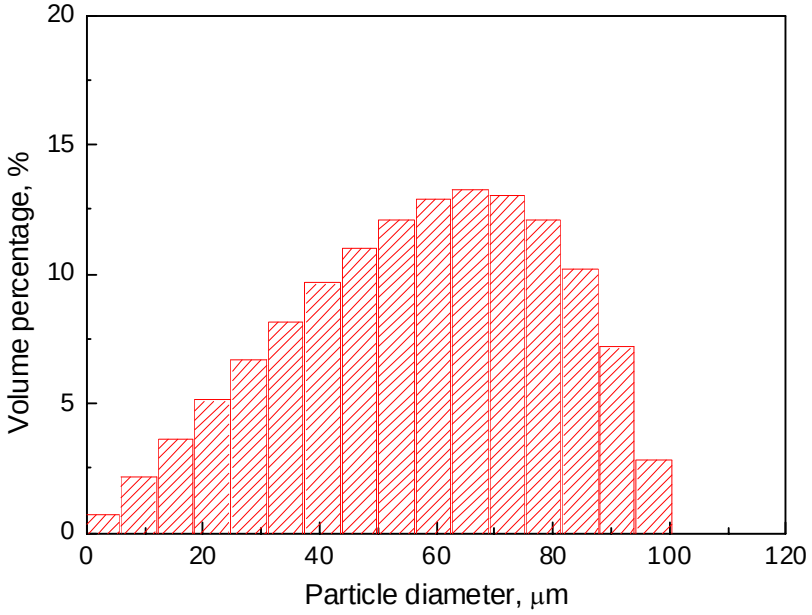

Figure 3-8 Random distribution of particle size

Chapter 4 Study of Injection Angle and Carrier Gas Flow Rate Effects on Particles In-Flight Characteristics

4.1 Introduction

During the last decade, numerous research have been carried out to investigate the influence of process parameters (power source, nozzle parameter, feedstock selection, injection methods and substrate conditions, etc.) and their relationships with morphology and properties of molten and semi-molten particles upon impact, and eventual coating quality [68, 143]. It is well recognized in the thermal spray community that the interaction of particles with the plasma is critical to the coating properties, which, to a large extent, depend on particles' temperature, velocity and melting status upon impact at the substrate. The experiments by Vardelle et al. [41] show that changing injection method can influence particle in-flight behavior significantly. This may provide an additional dimension for the process control.

To produce a good quality coating with desirable functionality, control and optimization of thermal spray processes are necessary through improving our understanding of complex heat, momentum and mass transport phenomena involved. Modeling plasma spray process has received considerable attention during last several decades [26, 41, 139, 144], in particular the interaction between the in-flight particles and the plasma jet [27, 28, 36, 64, 71, 79, 145]. Most simulations were conducted in a two dimensional geometrical configuration. The effects of carrier gas flow and particle injection from side were typically neglected because of difficulty in handling the complex three dimensional interactions between the carrier gas and the high temperature jet. Though the carrier gas flow injection enables the particle entrainment in the high-temperature/high-velocity plasma jet, it disturbs the jet and will affect the characteristics of in-flight particles behaviors [144-146]. The understanding of carrier gas and particle injection effects on plasma jet and particle behavior is desirable for control and design of plasma spray process.

In this chapter the influence of particle injection angle on particle in-flight behavior and characteristics is investigated through an integrated modeling and experimental approach. Plasma spraying of YSZ particles is selected as an example. Experiments are conducted to examine the characteristics of in-flight particles such as size distribution, temperature and velocity for the limited operating conditions. Numerical simulations are carried out to systematically study the effect of injection angle on particle behaviors under various carrier gas flow rates, and plasma jet perturbation by particle injection angle, carrier gas, and particle loading. It is shown that the comprehensive analysis is helpful for achieving optimal design of plasma spray.

4.2 Experiment and Simulation Setups

The experiments were to spray YSZ fused and crushed particles with angular morphology using Sulzer Metco 7 MB plasma torch (Westbury, NY, USA). The feeding stocks were injected radially via the argon carrier gas into the Ar-H_2 DC plasma jet. The injector (with inner diameter of 1.8 mm) is located at 8 mm above the torch axis, and 6 mm from the plasma torch exit. The schematic of plasma spray process is displayed in Figure 4-1. A commercially available YSZ powder was used and its size distribution shown in Figure 4-2 was measured by Beckman Coulter 2 LS 13 320 Laser Diffraction Particle Size Analyzer (Beckman Coulter Inc., Fullerton, CA, USA). DPV 2000 (Tecnar Ltée, St-Bruno, QC, CA) was used to measure the particle in-flight characteristics such as temperature, velocity and diameter[47, 53, 147]. The DPV 2000 instrument has two measurement modes for the in-flight particle states: single point and scan modes. For the single point mode, diagnostic data was collected through auto-centering sensor head to the maximum particle flux location (Flux center) and making measurements of particle velocity, temperature and size. For the scan mode, the sensor head was first auto-centered to the maximum flux location and then scanned in a square grid, e.g. a step of 5 mm and a total scanned area of 30×30 mm^2 around it to obtain a cross-sectional measurement of the complete particle stream, providing the contour information for that cross-section. The integrated diagnostic system used in experiments can be found in Figure 1-3.

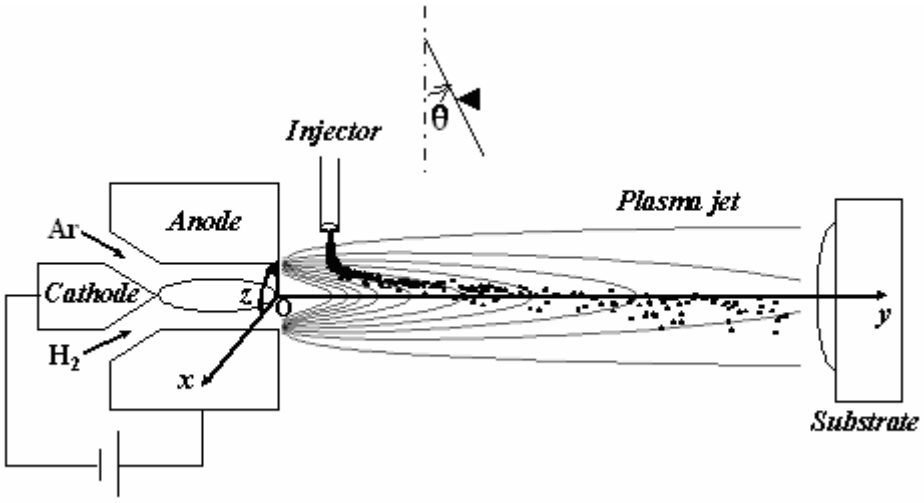

Figure 4-1 Schematic of plasma spray process where θ is the injection angle ranging between -90 to 90 deg. The angle for $\theta > 0$ is called the down stream (same direction as jet flow) injection angle; for $\theta < 0$ it is called the upstream injection angle; $\theta = 0$ is the normal injection

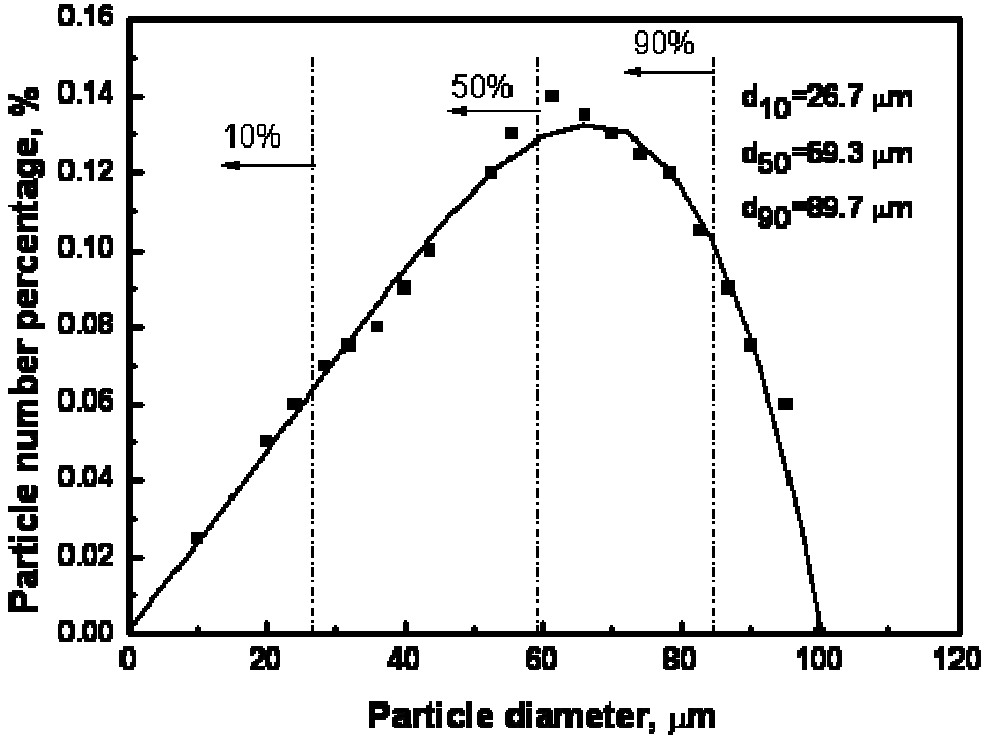

Figure 4-2 Initial size distribution for YSZ particles in the experiments and numerical simulations (dry powder system, d_{10} = 26.7 μm , d_{50} = 59.3 μm and d_{90} = 89.7 μm)

In this chapter, DPV single point mode had been used to obtain in-flight particle information at flux center. The sensor obtains the temperature, velocity and diameter over 10,000 particles at the maximum particle number flux position about 1 minute. The sensor can get information for single particles, which is valuable to give statistical information for a group of particles. It is noted that collection of such information is based on the assumption of gray body. Particle size and emissivity significantly affect the selection of particles by the sensor and thus the DPV system tends to collect information of big and hot particles.

The computational domain and boundary conditions for completing the simulations can be found in Chapter 3. Table 4-1 shows the operating conditions of plasma jet and carrier gas flow used in the experiments and numerical simulations, while Table 4-2 enlists the particle parameters and properties.

Table 4-1 Operating conditions for plasma jet and carrier gas flow

Processing parameters	Experiment	Simulation	
Primary gas, Ar, SLM[a]	45	45	30
Secondary gas, H_2, SLM	5.0	5.0	4.0
Current, A	500	500	400
Voltage, V	50.5	50.5	40
Carrier gas flow rate, Ar, SLM	5.0-7.0	4.0-8.0	2.5-8.0
Spray distance, mm	130	10-150	10-150

[a] SLM means standard liter per minute; 1 SLM=16.67 $cm^3 s^{-1}$

Table 4-2 Properties of YSZ feedstock material

Parameters	Values
Feeding rate, g min^{-1}	2.0
Mean size, μm	55
K_s, W m^{-1} K^{-1}	2.0
K_l, W m^{-1} K^{-1}	3.0
$C_{p,s,}$ J kg^{-1} K^{-1}	580
$C_{p,l,}$ J kg^{-1} K^{-1}	713
ρ_s, g cm^{-3}	5.89
ρ_l, g cm^{-3}	5.89
T_m, K	2950
L_m, kJ kg^{-1}	812.4
L_v, kJ kg^{-1}	6000

4.3 Results and Discussion

4.3.1 Injection Angle and Carrier Gas Effect

4.3.1.1 Experiment Observation of Injection Angle and Carrier Gas Effect on Particle Characteristics

Experiments have been conducted for five different carrier gas flow rates (5, 5.5, 6, 6.5 and 7 SLM) and three different injection angles (0, 5, 20 deg). Experimental results from DPV-2000 Flux Center at the spray distance of 130 mm are shown in Figure 4-3.

For a given carrier gas flow rate in the range of 5 to 7 SLM, it was found that with the increase in the injection angle from 0 to 20 deg, the particle surface temperature monotonically decreases. However, the particle's speed initially decreases and then increases. For all the carrier gas flow rates, the observed temperature reduction is about 100^{o}C as the results of the injection angle increase of 20 deg, which is expected to affect coating quality significantly. The observations above will be compared with the corresponding results obtained from numerical simulations and the controlling mechanisms will be explained in section 4.3.3.

For a given injection angle in the range of 0 to 20 deg, both the surface temperature and speed of particles will initially increase and then decrease as carrier gas flow rate increases. This is due to the fact that temperature and speed of particle depend strongly on heat and momentum transfer between plasma jet and particle. High plasma jet velocity will exert large drag force on particle, accelerating it to reach a higher velocity. On the other hand, high plasma temperature will allow more heat transferred to particle through its surface so as to increase particle temperature. Plasma jet has the highest temperature and axial speed in the core or jet axis center. Particles injected from side at a low carrier gas flow rate can only reach out-edge of plasma jet where both temperature and axial speed are low. Increasing carrier gas flow rate can bring particles further into a location where plasma has higher temperature and velocity. However, if the carrier gas flow rate is too large, particles will be carried further passing the plasma jet axis to a location where lower plasma jet temperature and velocity reside. It is worth to mention that there is a little discrepancy of this trend as shown in Figure 4-4 (a). Reversed trend has been obtained when carrier gas flow rate is increased from 6 SLM to 8 SLM. The observed discrepancy is, however, less than 5% of the absolute mean value. Consistent trend for carrier gas effect has been obtained in Figure 4-4 (b)-(d) under various process conditions and spray distances. That is, after reaching the highest temperature and velocity, further increasing carrier gas flow rate results in decreased T and V.

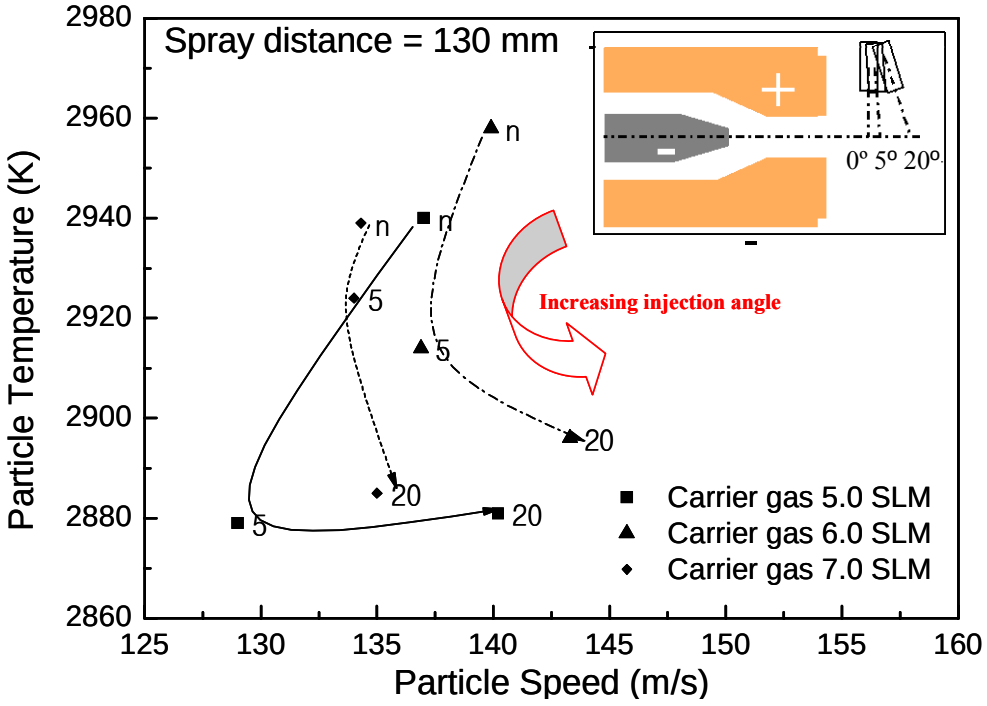

Figure 4-3 Experimental data: YSZ particle temperature and speed for normal injection, 5 degree and 20 degree injection angles at the spray distance of 130 mm

4.3.1.2 Numerical Simulation on Injection Angle and Carrier Gas Effect on Particle In-flight Characteristics

To understand the particle temperature and velocity with different injection angles, simulations have been performed at a broad range of injection angles (-30 to 30 deg) and carrier gas flow rates (4 to 8 SLM). As shown in Table 4-3, for carrier gas flow rate of 6 SLM, the predicted temperature and speed of particles have been compared with the experimental ones. It is clearly shown that the simulation results agree very well with the experiments and difference between prediction and experiment is less than 5%. Also, simulation results show the same trend observed in the experiments.

Table 4-3 Experiment results and model validation at 130 mm spray distance

(a) Particle surface temperature (K)

Carrier gas flow rates	*Injection angle*		
	0	5	20
6	2958	2914	2896
6*	2910	2905	2890

(b) Particle speed (m/s)

Carrier gas flow rate	Injection angle		
	0	5	20
6	140	137	143
6*	148	143	147

Note: * indicate simulation results

The effects of injection angle on particle surface temperature and velocity at different carrier gas flow rates are displayed in Figure 4-4(a)-(c) for the spray distances of 130 mm, 100 mm and 70mm, respectively. The primary gas flow rate is 45 SLM, which is the same as experiments. The combined effects of injection angle and carrier gas flow rate on particle temperature and velocity are examined here. Another set of operating conditions with a smaller primary gas flow rate of 30 SLM have also been simulated (Figure 4-5 and Table 4-4). The trends of temperature and speed changing with the injection angle for all of the simulated cases have been found to be consistent with the experimentally measured ones.

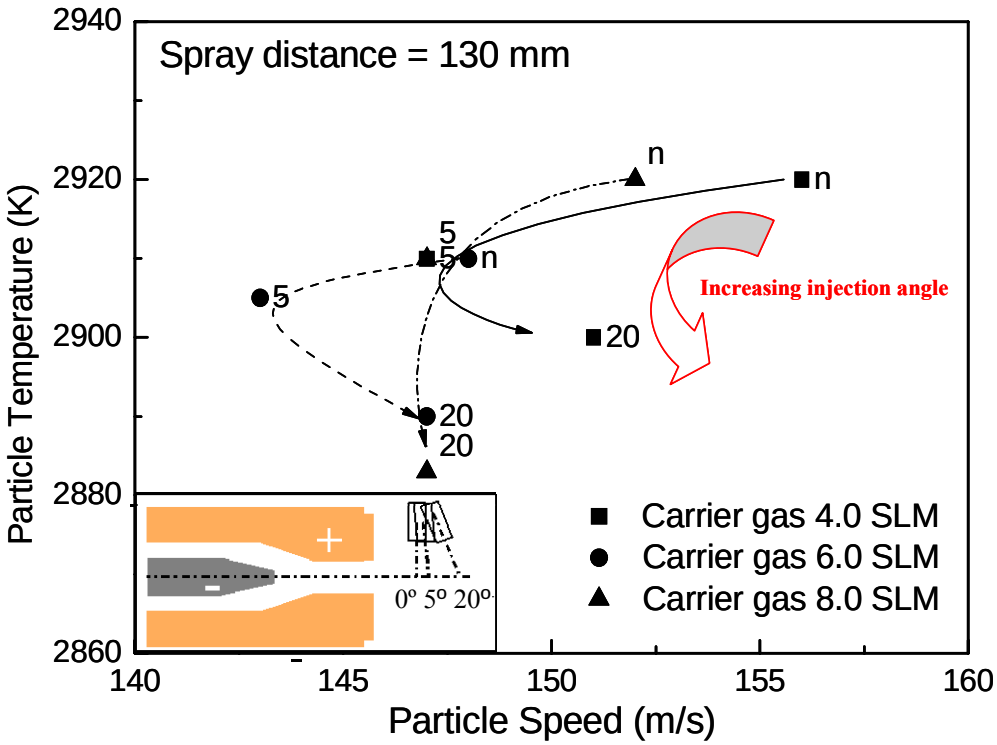

(a)

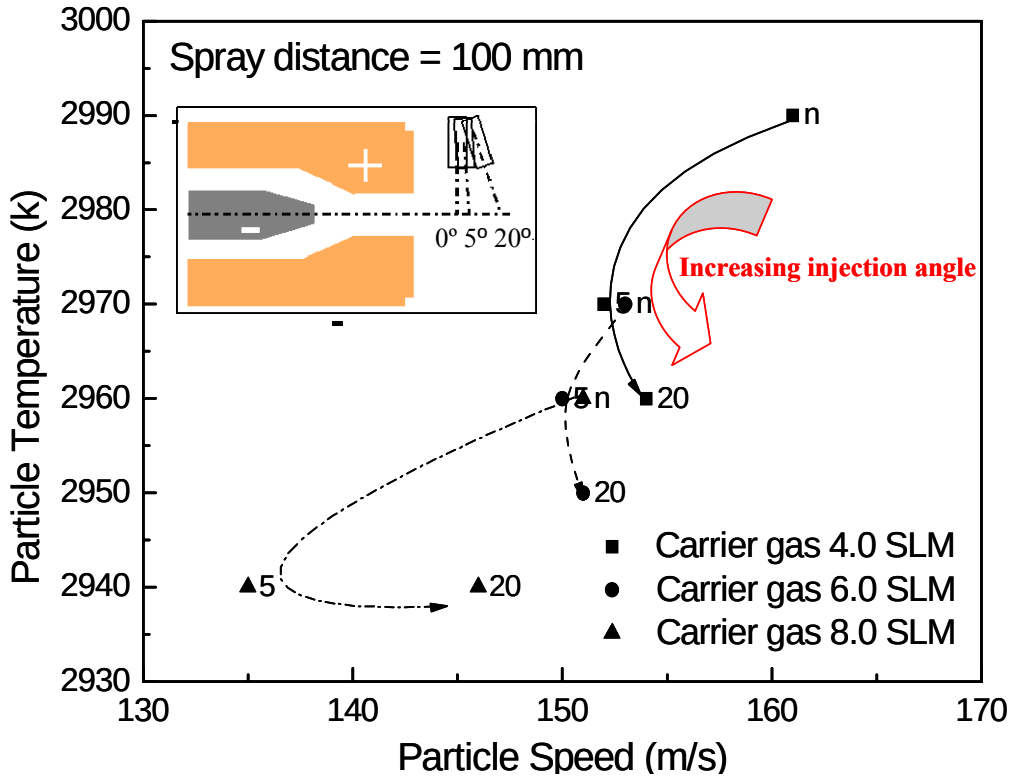

(b)

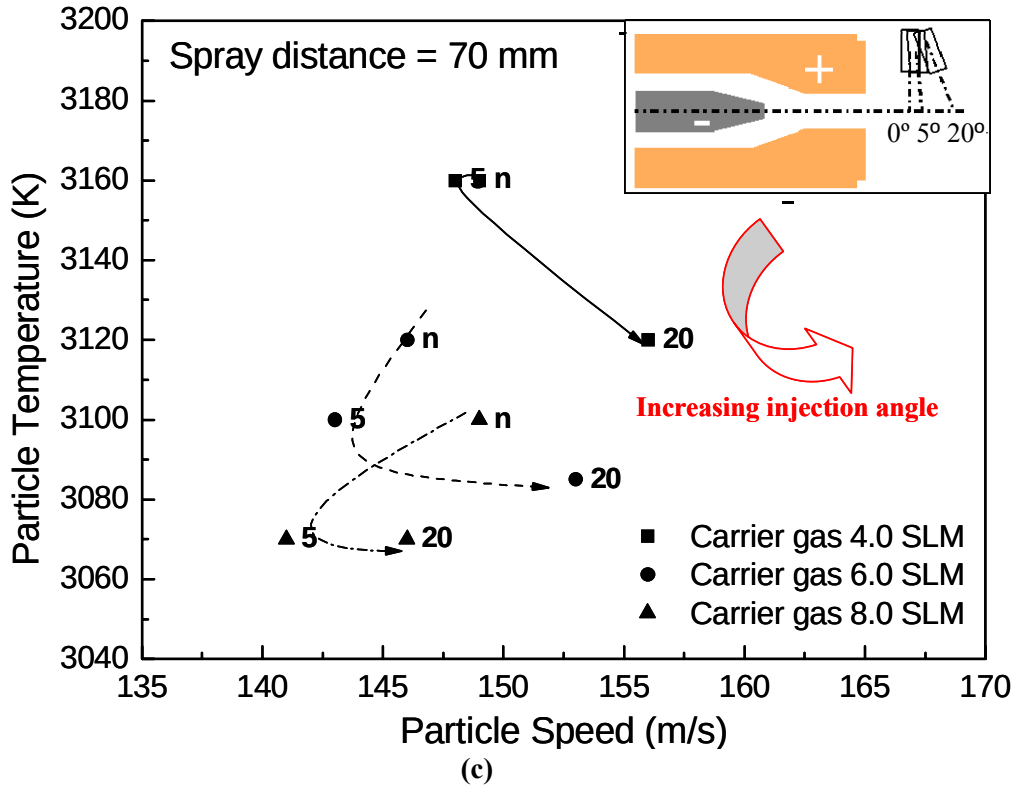

(c)

Figure 4-4 Simulation results: the effect of injection angle on particles temperature and velocity at the spray distance of (a) 130 mm, (b) 100 mm and (c) 70 mm, respectively

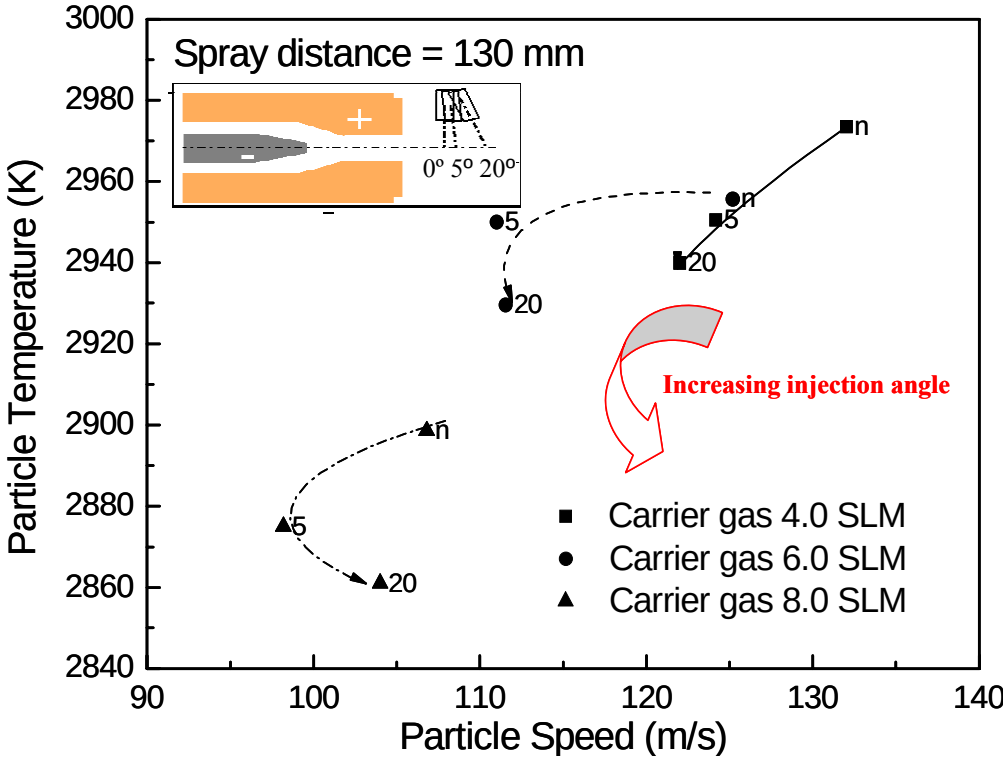

Figure 4-5 Simulation results: effects of injection angle on particle temperature and speed at the spray distance of 130 mm and primary gas flow rate of 30 SLM

Table 4-4 Simulation results at 130 mm spray distance

(a) Particle surface temperature (K)

Carrier gas flow rate, SLM	Injection angle, deg		
	0	5	20
4	2973	2951	2940
4*	2920	2910	2900
6	2956	2950	2930
6*	2910	2905	2890
8	2899	2875	2861
8*	2920	2910	2883

(b) Particle speed (m/s)

Carrier gas flow rate, SLM	Injection angle, deg		
	0	5	20
4	132	124	122
4*	156	147	151
6	125	111	112
6*	148	143	147
8	107	98	104
8*	152	147	147

Note: * indicate 45 SLM primary gas cases

4.3.1.3 Influence of Primary Gas Flow Rate and Injection Angle on Particle Characteristics

Two sets of operating conditions with different primary gas flow rates (45 and 30 SLM) have been simulated to investigate the influence of primary gas flow rate on the injection angle effect. The conditions and resulting statistical temperature and speed at Flux center are presented in Table 4-4. The injection angle and carrier gas effect at different primary gas flow rates are shown in Figure 4-4(a) and Figure 4-5 for the primary gas flow rate of 45 and 30 SLM, respectively. A higher primary gas flow rate provides greater momentum to in-flight particles, resulting higher particle in-flight speed (Figure 4-4a). As to the particle temperature, by increasing the flow rate of the primary Ar gas while maintaining the secondary H_2 flow rate, the H_2 composition in the plasma gas is decreased. The plasma energy density and particle temperature are therefore lowered. Due to the higher axial velocity of the plasma jet resulted from a large primary gas flow rate, particles will have less chance to penetrate vertically into the high temperature core, which further reduces the particle temperature. By increasing the carrier gas flow rate, the particle trajectory will shift more downwards which favors the penetration into the high temperature zone. Thus the competition of these effects will determine the particle temperature. Comparing Figure 4-4(a) with Figure 4-5, it can be concluded that, as far as the particle velocity is concerned, the change of plasma jet momentum due to primary gas flow rate will have a predominant influence.

It should be noted that the increase in carrier gas flow rate results in larger velocity difference for the case with a primary gas flow rate of 30 SLM (Figure 4-5). When the primary gas flow rate is low, the particle trajectory will be shifted more downwards by increasing the carrier gas flow rate, compared with the case with a high primary gas flow rate, and the acceleration time for the particle in the high velocity zone is reduced more.

With a carrier gas flow rate of 4 SLM, the particle temperature is higher in Figure 4-5 due to the high plasma jet temperature at a low primary gas flow rate. Comparing Figure 4-4(a) with Figure 4-5, the temperature difference is found to be reduced when the gas flow rate is increased to 6 SLM. This is because the particle trajectory is lowered

more significantly for the case with a low primary gas flow rate. When the carrier gas flow rate is further increased to 8 SLM, the change of particle temperature difference is reversed with a low particle temperature in Figure 4-5. This is because in the case where a primary gas flow rate is 30 SLM, particles penetrates vertically through the plasma plume rapidly when the carrier gas flow rate becomes very high and their heating time is therefore reduced significantly.

In the present study, according to both experiment and numerical results, it is concluded that a carrier gas flow rate of 4 SLM is preferred for achieving high particle temperature and velocity.

4.3.1.4 Combined Effect of Injection Angle and Spray Distance on Particle Characteristics

To investigate the spray distance effect on particle in-flight state, the statistical information has been presented for different spray distances in Figure 4-4(a)-(c). It is clearly seen that the temperature of particles at the spray distance of 70 mm is 100-130^{o}C higher than those at the spray distance of 100 mm and about 220^{o}C higher than those at the spray distance of 130 mm. This is because both plasma jet and in-flight particle have been cooled down by the cold ambient air at the spray distance from 70 mm to 130 mm.

Figure 4-6 shows the results at a broad range of injection angles (-30 to 30 deg) with the spray distance ranging from 6 to 13 cm. The carrier gas flow rate is fixed at 4 SLM since it favors high particle temperature and velocity, as discussed previously. The statistical average temperature and speed of particles for different spray distances have been listed in

Table 4-5.

From results in Figure 4-6(a) and (b), it can be concluded that for all the tested spray distances, both the speed and surface temperature of particle decrease with the increase of the injection angle. When the injection angle is fixed, the particle temperature will decrease with the spray distance, while the particle speed will increase with the spray distance.

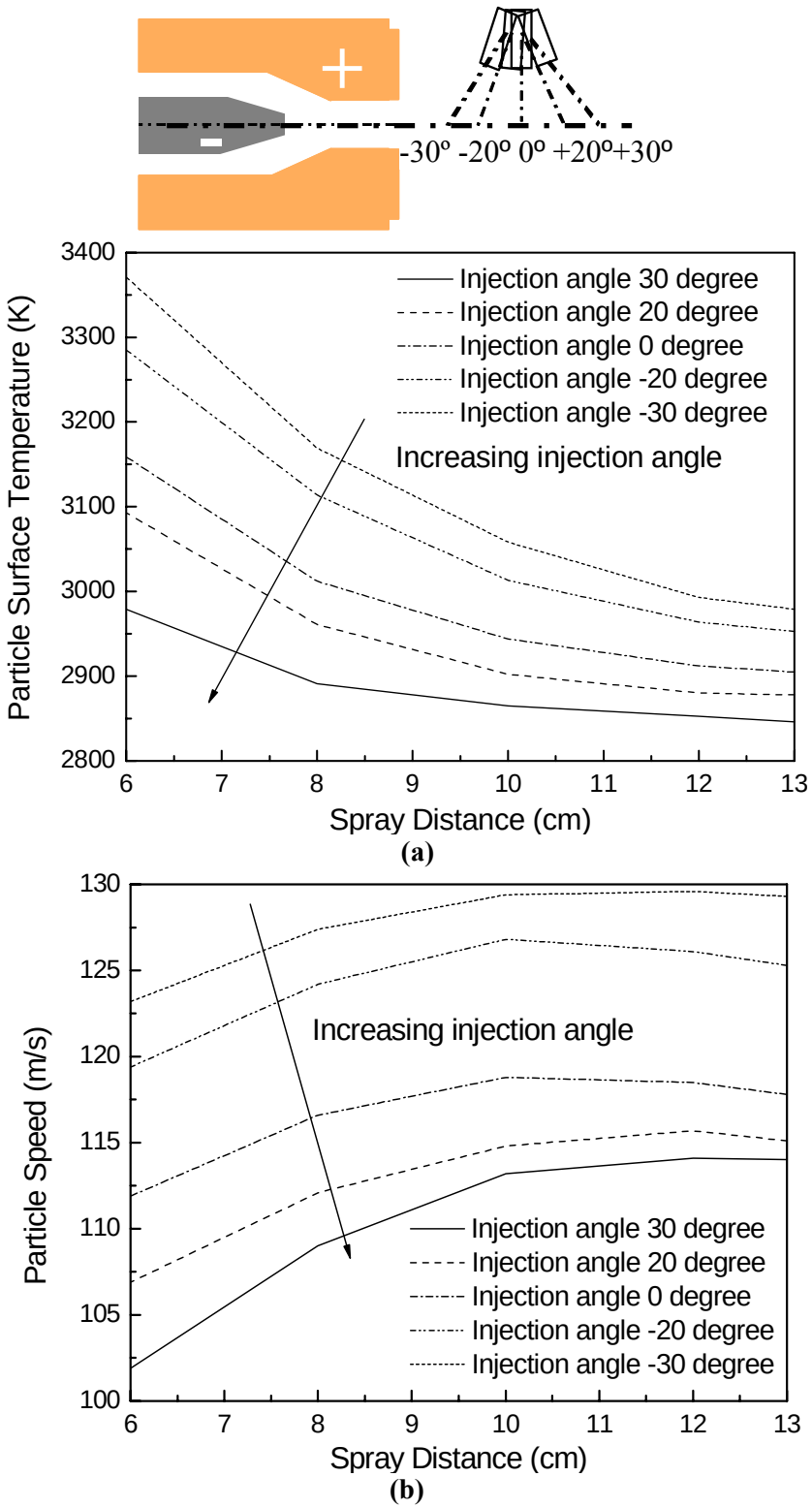

Figure 4-6 Simulation results: effect of injection angle on (a) particle surface temperature, and (b) particle speed at different spray distances

Table 4-5 Simulation results for injection angle effect at different spray distances

SD, mm	T, K	V, m/s	Injection angle						
			-30	-20	-5	0	5	20	30
70	T		3270	3185	3119	3089	3067	2963	2935
		V	125	124	122	114	112	110	106
100	T		3058	3013	2991	2944	2933	2902	2865
		V	129	127	125	119	118	115	113
130	T		2979	2953	2924	2905	2903	2878	2846
		V	129	125	123	118	117	115	114

4.3.2 Influence of Injection Angle and Carrier Gas on Particle Size Distribution

Figure 4-7(a) shows the particle size distribution at the Flux Center for the cases with the primary gas flow rate of 45 SLM and the injection angle of 20 deg. By increasing the carrier gas flow rate form 5 to 6 and 7 SLM, the mean particle size drops from 62 to 57 and 55 μm with the standard deviations of 22, 21 and 20 μm, respectively. It is noted that the particle diameter from DPV system does not result directly from a measurement but from a computation based on assumptions (emissivity) and its accuracy is 80% max. When increasing the carrier gas flow rate, the initial particle speed increases, so does its momentum. This will make it easier for large sized particles to penetrate through the plasma plume vertically, which explains the drop of particle size at the Flux Center when increasing the carrier gas flow rate.

Figure 4-7(b) reveals the particle size distribution under different injection angles for the primary gas flow rate of 45 SLM and the carrier gas flow rates of 5 SLM. At the same carrier gas flow rate, the particle trajectory shifts upwards when the injection angle is increased, favorable to the dwelling of large sized-particles. This can be seen from the increased (as shown by the red arrows in the graphs) peak value for the large sized particles in the figures.

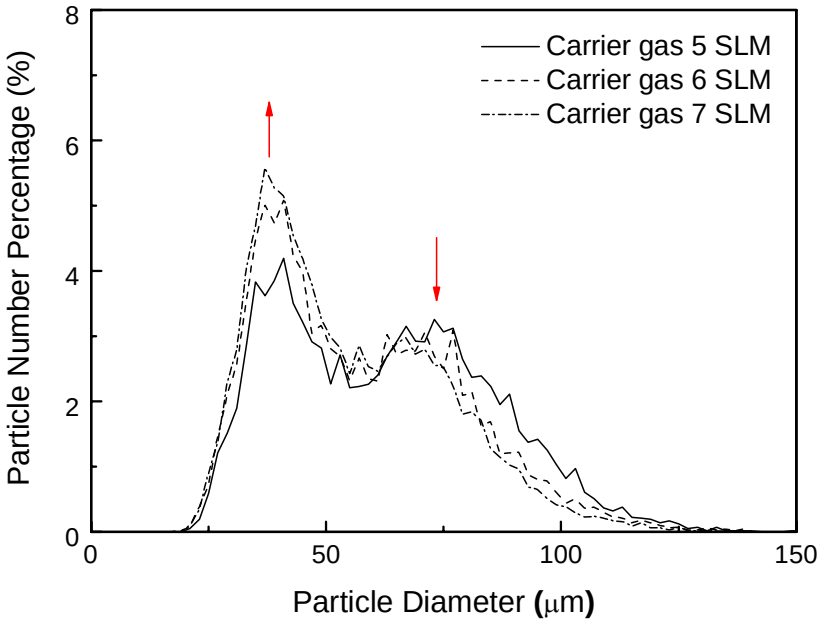

(a)

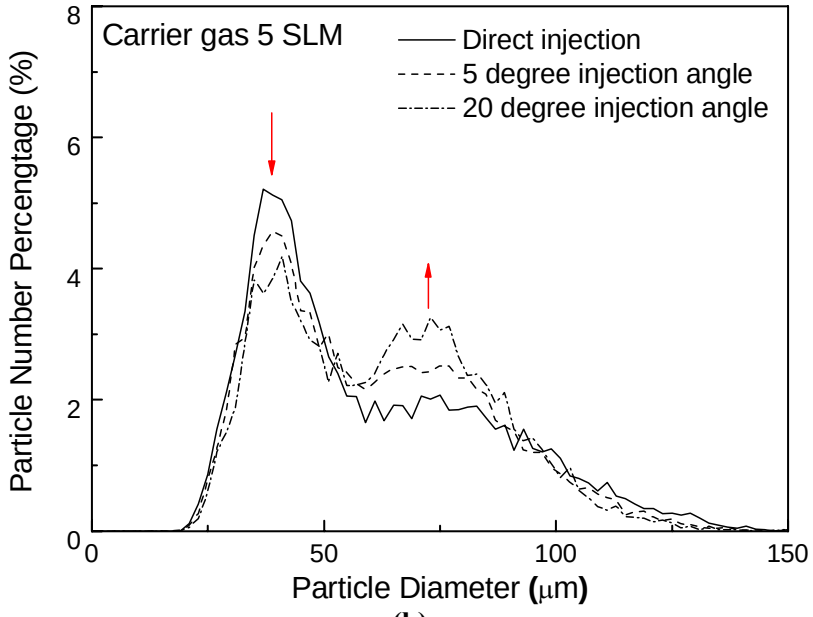

(b)

Figure 4-7 Experimental results: particle size distribution. (a) Effect of the carrier gas flow rate for the injection angle of 20 deg and (b) Effects of injection angle at carrier gas flow rates of 5 SLM

4.3.3 Interaction between In-Flight Particle and Plasma Plume

In experiments it is difficult to accurately quantify the influence of in-flight particles on the plasma jet even though the particle status can be obtained from the diagnostic

sensors. With the help of numerical simulation, such effects can be predicted and the experimentally observed phenomena can be better understood.

Figure 4-8(a) and (b) show the contours of temperature and velocity components of plasma in the axial direction, and average trajectories of particles under different injection angles. Since the average size of particles is about 55 μm, the particles with 50 μm diameter are presented here. As highlighted by dash-dot ellipse in Figure 4-8(a), the temperature contour suddenly changes. Simulation results show the occurrence of such sudden change at the location where particle's temperature is at its melting point. It is therefore believed that significant heat absorbed by particle to accommodate its phase change is the key reason causing plasma jet temperature drop. This phenomenon will be further studied in the next chapter by considering loading effect on the plasma plume profile. Due to the strong correlation between velocity and temperature of plasma jet, similar change is also predicted for the velocity as seen in Figure 4-8(b). Figure 4-8(c) and (d) show the particle and surrounding gas temperature and velocity at various injection angles. As seen in Figure 4-8(a), the hot regime of the plasma jet is limited within a short distance from the nozzle exit. Particles with zero and small injection angles at certain carrier gas flow rate tend to enter into high temperature zone, where it is easily heated up to the melting temperature due to strong heat transfer between particles and plasma jet. Compared with Figure 4-8(b), plasma jet tends to heat up particles within a spray distance of 5 cm. When the spray distance is larger than 5 cm, the plasma jet temperature is lower than the particle temperature, so the particles are actually cooled by the plasma jet. For the normal injection, particles are heated up rapidly to the highest temperature in the hot plasma jet and then cooled down gradually. For the injection at 20 degree angle, the rate of particle temperature change is mild. This is attributed to the fact that particles can not penetrate into the hot zone for rapid heating and their upward trajectories reduce the strength of penetration resulting in slow temperature changes. It is worth to mention that, in experiments, some small particles may be bounced off from the plasma jet due to various forces acted on the particles, in particular thermophoresis forces and Knudsen effect. In the simulations, only the drag force is considered. All particles are therefore capable of penetration. This may over-predict the amount of particle collected. In fact, for particles to penetrate within the plasma flow, density of momentum imparted to particles has to be of at least the same order as the one imparted to plasma flow. Under the current assumption, the determination factors for particle penetration are the carrier gas flow rate and injection angle.

In terms of the plasma jet flow, the range of high velocity is much longer than the range of high temperature (Figure 4-8b). Particles can be accelerated at the far downstream region. Figure 4-8(d) shows that particles with the normal injection (0 deg injection angle) will be accelerated rapidly within a short spray distance of 2 cm. After that the acceleration is decreased compared with other injection angles. This is due to

the reason that, in the normal injection, particles penetrate into the high speed core earlier and then pass through it. Figure 4-8(d) shows that the particles with 20 deg injection angle have the highest velocity at downstream; while the particles with 5 deg injection angle have the lowest speed with a moderate acceleration/deceleration rate. Particles with 0 or 5 deg injection angles can penetrate into the hot core and their temperature is higher than those with 20 deg injection angle at the same carried gas flow rate. On the other hand, the speed of particles with an injection angle of 20 deg is higher due to longer residence time for such particle in the high velocity zone of the plasma jet. The numerical results can explain the experimental data in Figure 4-3.

As shown in Figure 4-3, for the particles with 0 or 5 deg injection angles, the carrier gas flow rate of 6 SLM will provide the right momentum for particles to move into the hot core so that the temperature will achieve the maximum value which is higher than those with carrier gas flow rates of 5.5 and 6.5 SLM. The particles with 20 deg injection angle will all locate in the high velocity region. As the carrier gas flow rate increases, the particle trajectory will move downwards and the speed is expected to be smaller since particles will penetrate vertically through the high velocity zone earlier. By adjusting the injection angle and carrier gas flow rate, the optimal operating conditions can be achieved.

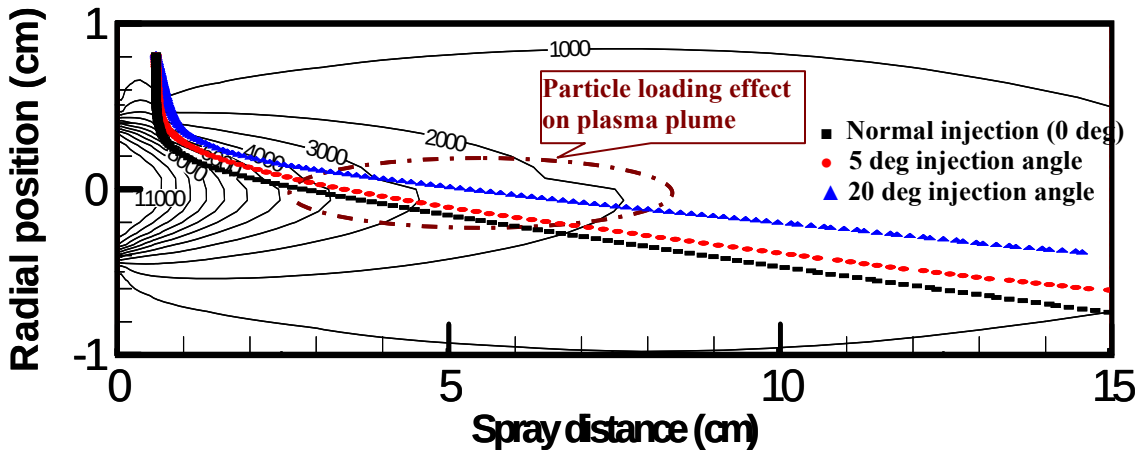

(a)

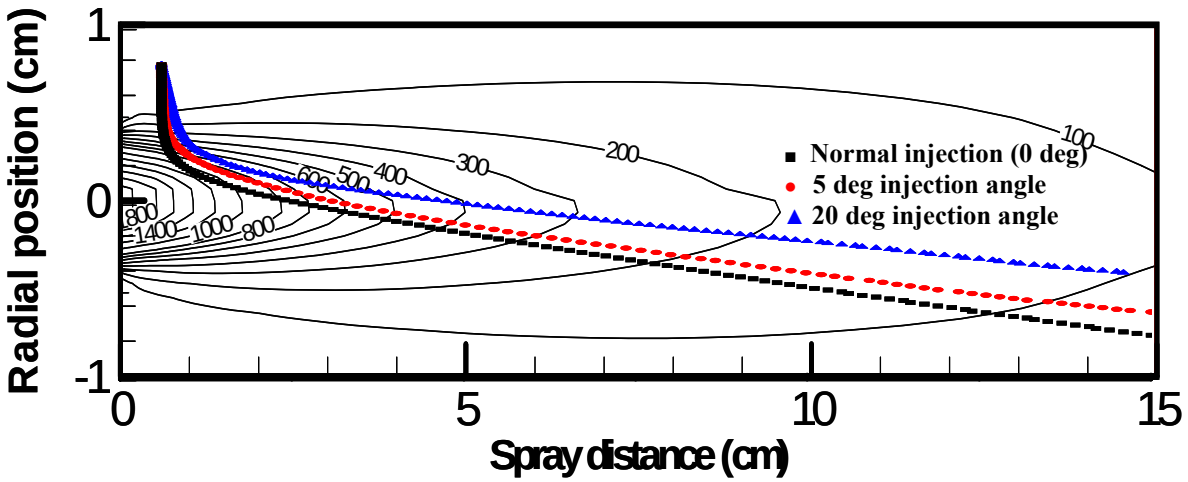
Radial position (cm)
Spray distance (cm)
Normal injection (0 deg)
5 deg injection angle
20 deg injection angle
100
200
300
400
500
600
800
1000
1400

(b)

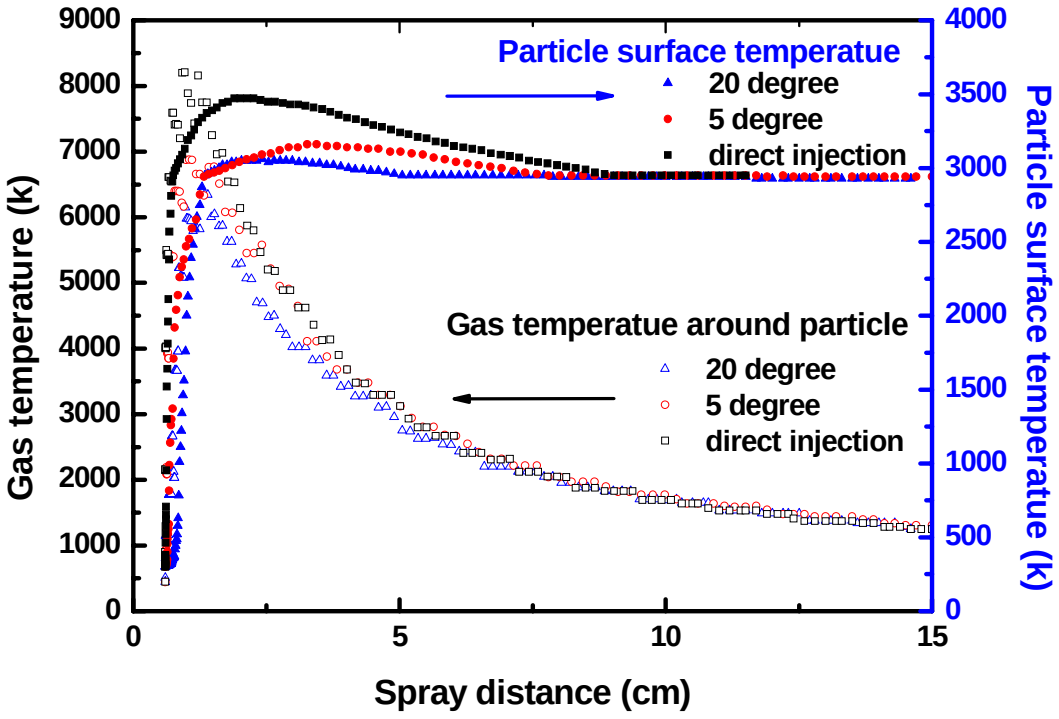
Particle surface temperatue
20 degree
5 degree
direct injection
Gas temperatue around particle
20 degree
5 degree
direct injection
Gas temperature (k)
Particle surface temperatue (k)
Spray distance (cm)

(c)

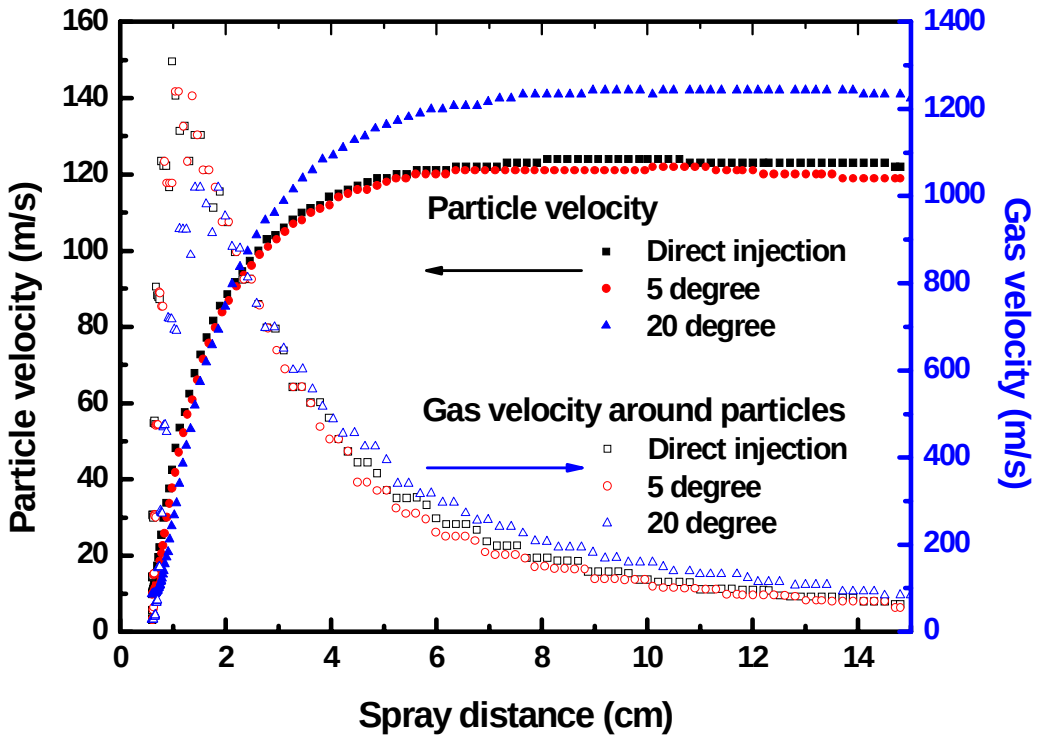

(d)

Figure 4-8 Simulation results: particle trajectories with (a) plasma temperature field and (b) plasma velocity in the main flow direction; (c) temperatures of gas and particle vs spray distance at different injection angles; and (d) speeds of gas and particle vs spray distance at different injection angles. (operating conditions: primary gas flow rate of 45 SLM and carrier gas flow rate of 6.0 SLM)

4.4 Conclusions

In this chapter simulations were performed and diagnostic experiments were conducted to investigate the correlation among the particle injection angle, carrier gas flow rate and primary gas flow rate with the characteristics of in-flight particles. Numerical results were compared with the experimental measurements and a good agreement has been achieved. The results show that:

- The injection angle and carrier gas flow rate both have significant impacts on the plasma jet and in-flight particle trajectory, consequently, particle surface temperature and particle velocity. When the carrier gas flow rate is fixed, it is found experimentally and numerically that the high particle surface temperature can be achieved at a small injection angle while the high particle speed can be achieved at a large injection angle.
- For the moderate injection angle of 5 degree, the particle speed achieved is the lowest while the particle temperature is in between. This observation is

found to be independent of the primary and secondary gas flow rate and spray distance.

- In the case of both carrier gas flow and injection angle changing, a high carrier gas flow rate and a small injection angle should be used to ensure high particle temperature and velocity at a certain spray distance.
- Under the current operating conditions, the carrier gas flow rate of 4 SLM and injection angle of –30 deg should be chosen. In addition, a spray distance in the range of 8 to 10 cm is favorable for providing the particles with higher velocity and surface temperature.

Chapter 5 Plasma Forming Process Parameters Effect on Optimum Particle Injection

5.1 Introduction

Apart from process parameters, particle injection has also been found to play an important role on particle in-flight behavior, especially for the external orthogonal injection of less dense particles such as ceramic ones[71, 114, 115]. Experimental studies further showed that changes of in-flight particle properties caused by particle injection are in the same order as that resulting from a systematic change in process parameters[115, 117, 139, 148, 149]. Ideal injection of particles would be axially through the torch. Novel variants in torch designs such as the three cathode design (Northwest Mettech Corp., North Vancouver, Canada), electromagnetically coalesced plasma using three cathodes (Flame Spray Industries, Port Washington, NY) and stick type cathode with modifications (100 HE; Progressive Technologies Inc, Grand Rapids, MI) [150] have allowed for axial injection with some success. However, there are several design constraints and disadvantages that have prevented widespread implementation of this axial injection strategy. They include arc instabilities introduced by the presence of solid particles within the plasma forming zone, powder build-up and clogging of the nozzles during the spray, and complexities in nozzle design and hardware assembly.

Injection of powder particles into a DC plasma plume radially has been extensively studied. Figure 5-1 illustrates radial injection process through laser strobe imaging[58]. Although significant experience base and applications have existed for this method, very limited scientific investigations have been conducted.

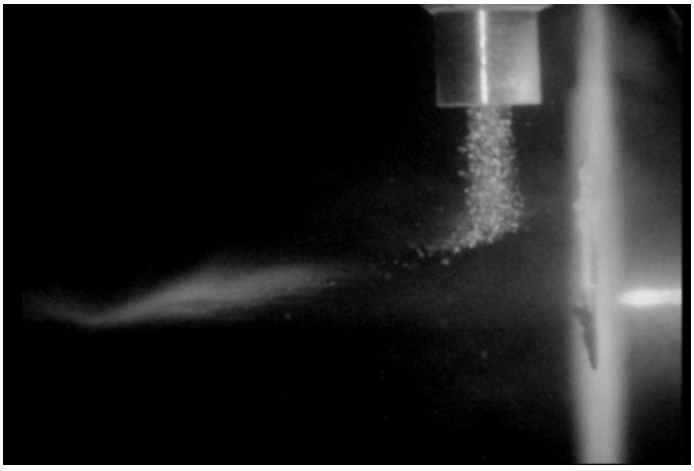

Figure 5-1 Laser Strobe Control Vision ™ image of orthogonal external injection of particles into a DC thermal plasma jet[58]

During radial injection, since the particles do not necessarily follow an axial flow path, the interaction of the trajectory with plasma jet becomes important. Experimental work at the Center for Thermal Spray Research (CTSR) has shown the existence of a maximum in average T_P & V_P for any given combination of plasma forming process parameters, i.e. different combinations of primary and secondary plasma gas flow rate, current and voltage. This is clearly due to maximized heat and momentum transfer to particles.

In this chapter, a systematic investigation to identify and quantify maximum average temperature and velocity at any given spray distance is presented. The fundamental mechanism behind the experimentally observed phenomena that there exists optimum average T_P & V_P for any given combination of plasma forming process parameters is identified through comparing of numerical and experimental results. Finally, effect of particle injection on plasma plume, which has been briefly described in Chapter 4, is analyzed in detail at the end of this chapter.

5.2 Experiment and Simulation Setups

Sulzer Metco (Westbury, NY, USA) 7MB DC plasma torch has been used with a nozzle exit diameter of 8mm. Ar and H_2 are used as primary and secondary plasma gas, respectively. Angular morphology YSZ feedstock (HW1532, Saint-Gobain) with 10 to 75 μm size distribution and 55 μm average diameter was injected radially into the plasma plume through a 1.8 mm injector at about 6 mm downstream from the nozzle exit and 8 mm above the torch axis. The properties and size distribution of feedstock particles used in simulations are the same as those used in experiments. The size distribution of YSZ particles is shown in Figure 4-2.

To understand the influence of particle injection on the in-flight characteristics, widely different combinations of the plasma forming parameters as shown in Table 5-1 have been chosen for experiment. Three-dimensional simulations have been performed using the same process conditions as experiments. In each case, the carrier gas was increased from a low to high level by a step size of 0.5 SLM. The plume and particles were characterized using an integrated sensor setup as shown in Figure 1-3.

Plume intensity profiles were obtained from SPT, based on which the plume centroid location and plume width can be obtained. IPP was used to measure ensemble temperature [45, 47, 151]. The characteristics of each single particle, such as temperature, velocity and size, were measured by DPV-2000 (Tecnar Ltée, St-Bruno, QC, CA) both at the flux center and the entire cross section of the plume, in the form of symmetric 7×7 grid covering 30 mm^2, at the chosen spray distance of 130 mm. To avoid the reflection from sensor heads, the DPV-2000 was located 30 mm away from SPT sensor with the same horizontal level.

A brief discussion of computational model for air plasma spray process has been provided in Chapter 3 to help understanding our modeling approach. Solution to the equations has been performed by using the program Lava-3D-P [38, 39]. The computational domain and some of the boundary conditions used in the plasma jet calculation have been shown in Figure 3-6.

3-D Simulations were performed at the same process conditions as the experiments (see Table 5-1) to enable comparison of results. The particle properties used in computation and feedstock size distribution of YSZ are provided in Table 4-2 and Figure 4-2, respectively.

Table 5-1 Process parameters for experiment and simulation during air plasma spraying of YSZ

Process Parameters	*Experiment*			*Simulation*		
Primary gas, Ar, SLM*	30	45	60	30	45	60
Secondary gas, H_2, SLM	5.0	5.0	5.0	4.0	5.0	5.0
Current, A	500	500	500	400	500	500
Voltage, V	45.8	50.5	54.5	40	50.5	54.5
Carrier gas flow, Ar, SLM	2.5-5.5	4.5-7.0	6.5-8.0	1.5-8.0	2.0-8.0	2.0-8.0
Spray distance, mm	130	130	130	10-150	10-150	10-150
Feeding rate, g/min	2.0	2.0	2.0	2.0	2.0	2.0

* SLM=standard liter per minute, 1 SLM=16.67 cm^3s^{-1}.

5.3 Results and Discussion

5.3.1 Effect of Process Parameters on In-flight Particle Behavior and Injection Optimization

The influence of carrier gas flow rates on the in-flight particle behavior has been investigated under three different sets of process conditions(see Table 5-1). For each set, while keeping all the other operating conditions unchanged, in experiments maximum particle temperature and velocity is achieved by increasing the carrier gas flow rate from a low level to a high level. For the spray distance of 130 mm, a corresponding optimum spray position at which the in-flight particles have the highest temperature and velocity was identified. It is found that the measured particle temperature and velocity are strongly dependent of the plume and particle conditions. To cross compare the experiment data under different set of conditions, Figure 5-2 depicts the complete range of particle status obtained under different primary, secondary and carrier gas flow rates. It should be noted that measurements were made at the maximum flux location of the spray plume. The circles marked on the chart represent particle status for the optimum injection position.

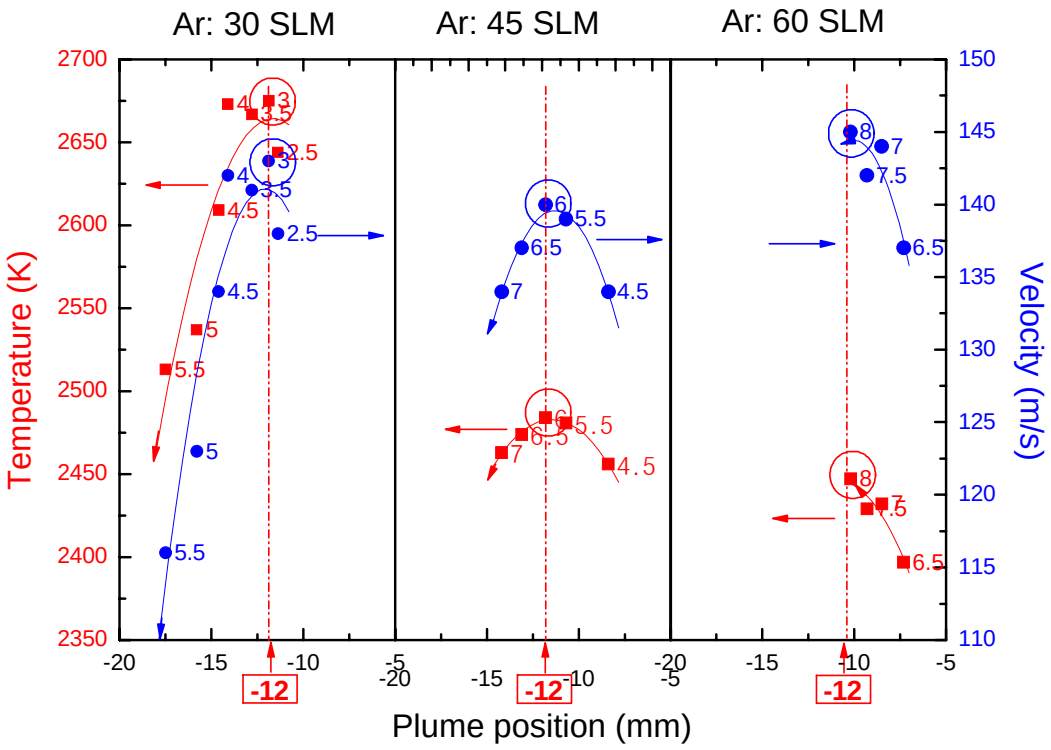

Figure 5-2 Mean particle temperature and velocity (from 10,000 particles measured using DPV 2000) as a function of plume position for different primary gas (Ar) flows. Maxima could be observed in both T and V in each case. The plume position of the maximum is the same in each case

It is clearly seen in Figure 5-2 that, by increasing the primary gas flow rate from 30 SLM to 45 SLM and to 60 SLM while keeping the secondary gas flow rate unchanged, the optimum particle temperature, i.e. the highest particle temperature achieved, decreases. For the optimum particle velocity (highest particle velocity achieved), it firstly decreases and then increases when the primary gas flow rate increases. The above observation can be explained as follows. For the plasma jet, increasing primary gas flow rate will increase the total mass flow rate and momentum of the jet. The optimum particle velocity should therefore be increased. On the other hand, if the secondary gas flow rate is kept at constant, the generated heat will not change much while the primary flow rate is increased. The temperature of the plume will therefore drop, causing the reduction of the volume flow rate of the plasma. This means that optimum particle velocity should decrease while increasing primary gas flow rate. The above two effects compete with each other while increasing primary gas flow rate. At first the velocity drop due to temperature decrease is more prominent than velocity increase caused by total mass flow rate increase, so the optimum particle velocity firstly decreases. After a certain point the mass flow rate increase effect becomes dominant, so the optimum velocity starts to pick up. The optimum particle temperature, however,

decreases monotonically due to the plume temperature decrease caused by mass flow rate increase.

For each tested primary flow rate, temperature and velocity of the in-flight particles exhibit similar behavior: when increasing the carrier gas from a low level to a high level, both the temperature and velocity firstly increase. After reaching a maximum value, they start to decrease. It is believed that, when the carrier gas flow rate is increased, the particles have more chance to go into the high speed/temperature plasma plume. Further increasing the carrier gas flow rate therefore increases particles' chance to be heated and accelerated. On the other hand, if the carrier gas flow rate is too big, the particles get high momentum and they penetrate through the plasma plume quickly. This explains the particle temperature and velocity decrease when the carrier gas flow rate is over a certain level.

The plume position is shown in Figure 5-3. For a given spray distance the corresponding optimum plume position can be found from the SPT sensor. Optimum plume position is defined as the position where the in-flight particles have the maximum temperature and velocity. As seen from Figure 5-2, the optimum plume position (vertical position to the substrate) is about 12mm at the spray distance of 130mm, which is true for all the primary and secondary flow rates tested in experiments.

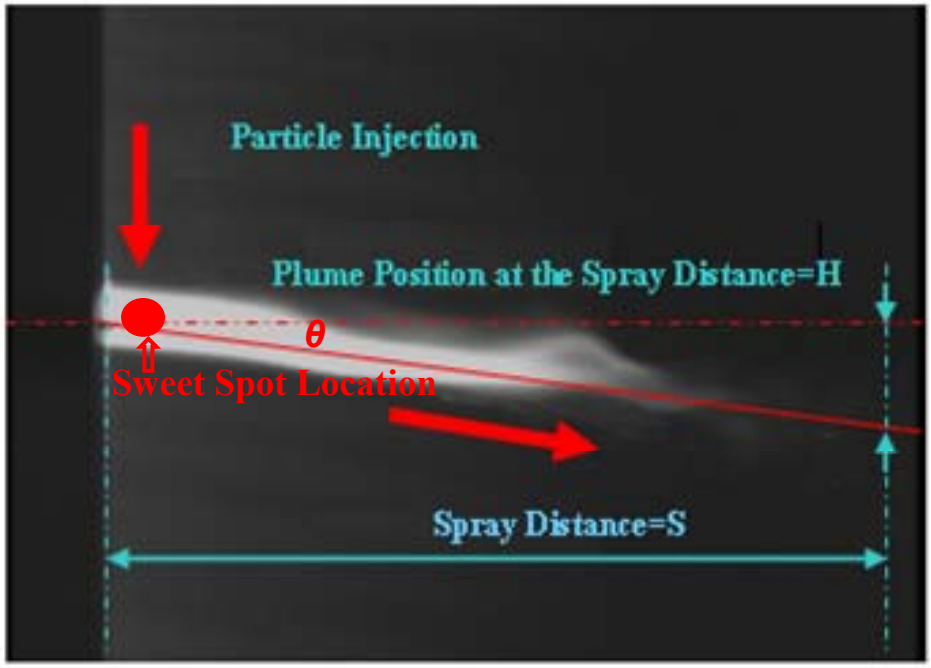

Figure 5-3 Plume position and definition of plume angle

If we define the angle between the torch axis and the plume center line to be the plume angle, the value of the plume angle should be as follows:

$$\tan(\theta) = H / S \tag{5-1}$$

where H is the plume position and S is the spray distance. For the cases tested, the optimum plume angle corresponding to the optimum plume position is found to be 5 degrees. It is obvious that if the particle trajectory is close to the 5 degrees red solid line shown in Figure 5-3, optimum particle velocity and temperature can be achieved. Also defined in Figure 5-3 is the so called 'sweet spot'. The 'sweet spot' is defined as an area in the center of the plasma jet. It is believed that proper carrier gas flow rate should be used to inject the particles into the sweet spot. The particles therefore will be heated and accelerated following the 5 degrees red solid line, and optimum velocity and temperature upon impact are therefore achieved.

Numerical simulation results are presented here to further explain the above theoretical analysis based on experiment observations. Simulation results provide trajectories for different sized particles as shown in Figure 5-4. Since the average particle diameter is 55 μm, the trajectory for particles with diameters of 30 μm, 50 μm, and 70 μm are obtained through simulation. Similar shaped trajectory can be found for different sized particles, except that large particles go far more downwards due to a large vertical momentum.

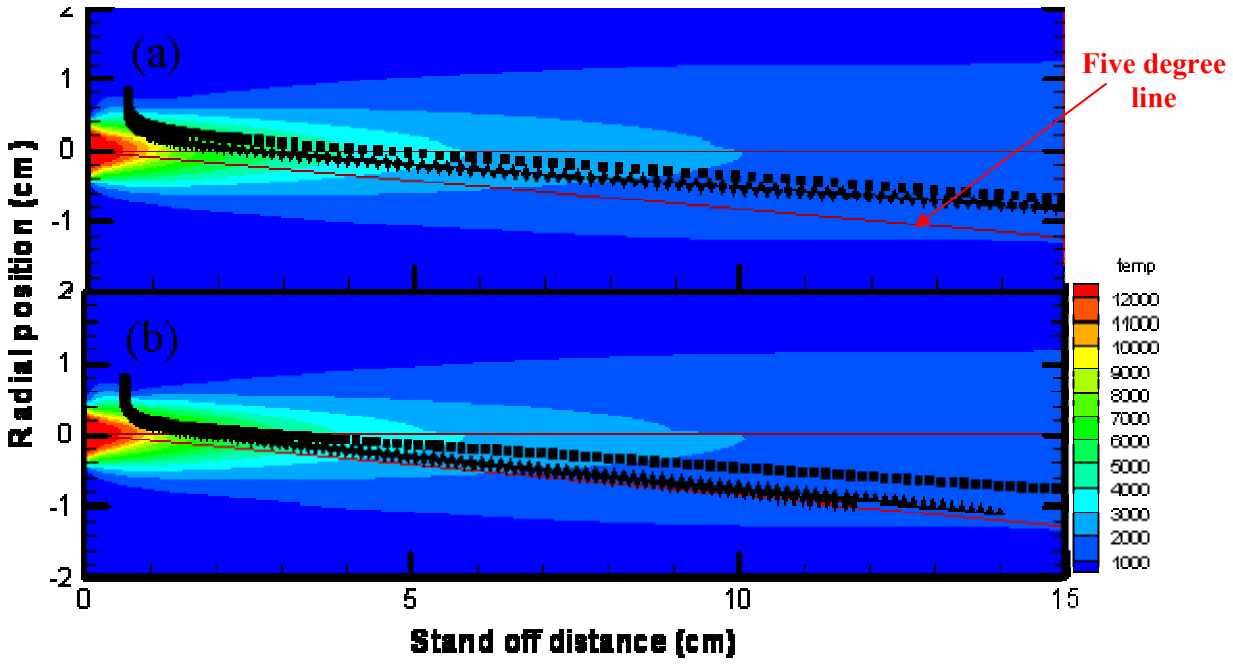

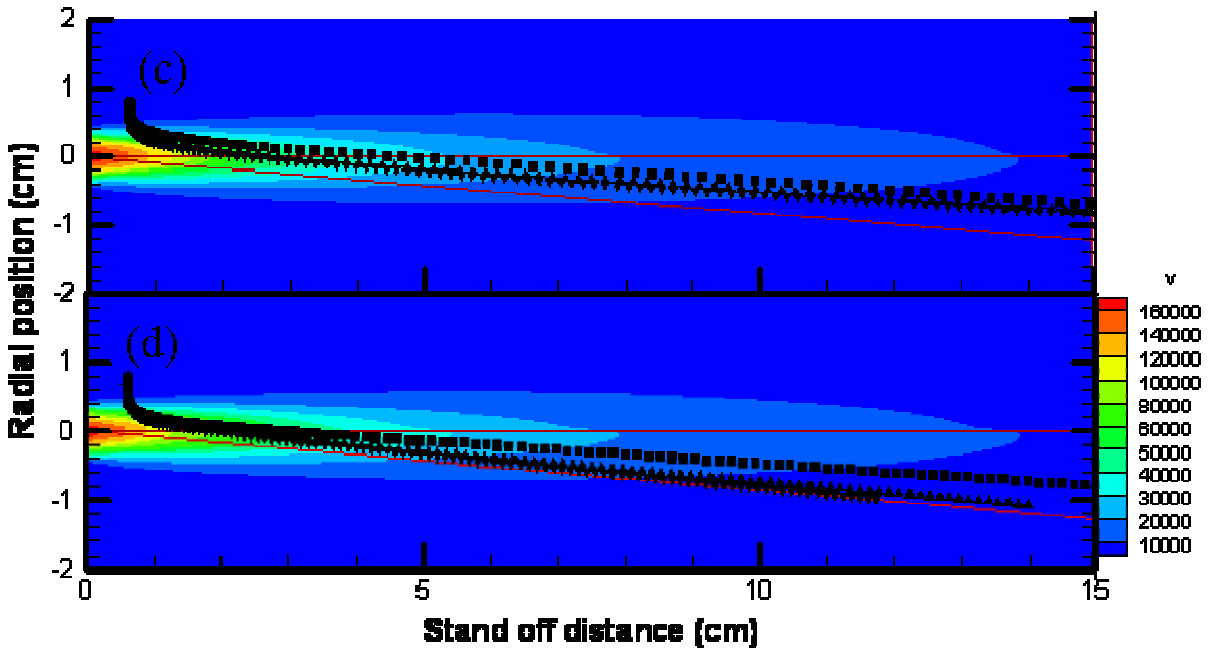

Figure 5-4 Carrier gas effect on different sized particles. Particle trajectory for a carrier gas flow rate of 2.5 SLM (a) temperature profile (c) velocity field; for a arrier gas flow rate of 4.0 SLM (b) temperature profile, and (d) velocity field. ■: d=30 μm, ▼: d=50 μm, ◄: d=70 μm

The existence of the optimum angle for each given spray distance can be explained as such: a high carrier gas flow rate increases the probability of particles to penetrate into the hottest and fastest part of the plasma plume. When they penetrate the plume faster, the particles will have less time to be heated and accelerated. In addition, plasma plume can be cooled down, decelerated and pushed far more downwards by the carrier gas with a high velocity. As shown in Figure 5-4, the optimum temperature and velocity can be obtained by simulations with a carrier gas flow rate of 4 SLM. This agrees well with the experiment results with same operating conditions. According to the trajectory of different sized particles shown in Figure 5-4, it is revealed that the particle trajectory under a carrier gas flow rate of 4 SLM is much closer to the red reference line which represents the 5-degree optimum plume angle.

The existence of the optimum position is due to the maximized heat and momentum transfer to particles and also indicating the particle trajectory around the plume axis. To examine whether carrier gas influences the plume center location, we have also calculated the ratio of average particle and carrier gas velocity at the exit of the injector to the plasma jet average velocity along the nozzle axis at its horizontal location just before the injector. The calculated velocity ratios at the standoff distance of 0.6 cm are shown in Figure 5-5 (a) by blue circle together with experimental result of Eq. (5-1) for plume angle by red square. It is noted that for the primary Ar gas flow rates of 30, 45 and 60 slm, the carrier gas flow rates to obtain maximum temperature and velocity at

plume center are 3.5, 6, 8 SLM, respectively, whereas the same velocity ratio as well as the same plume angle have been obtained from simulation and experiment respectively as discussed above (shown in Figure 5-5 (b)). This finding allows us to estimate and pre-identify the process condition and the achieved optimum plume location.

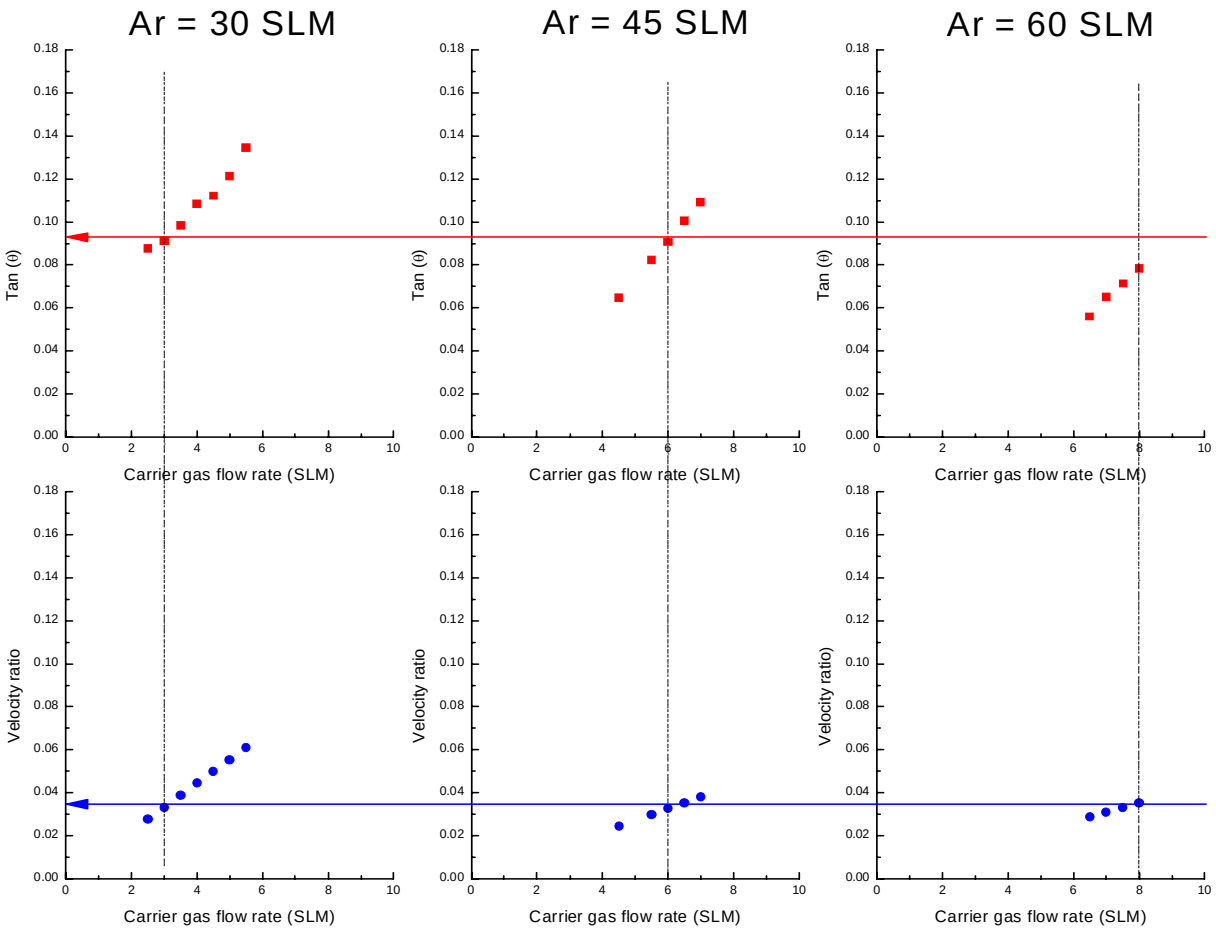

(a)

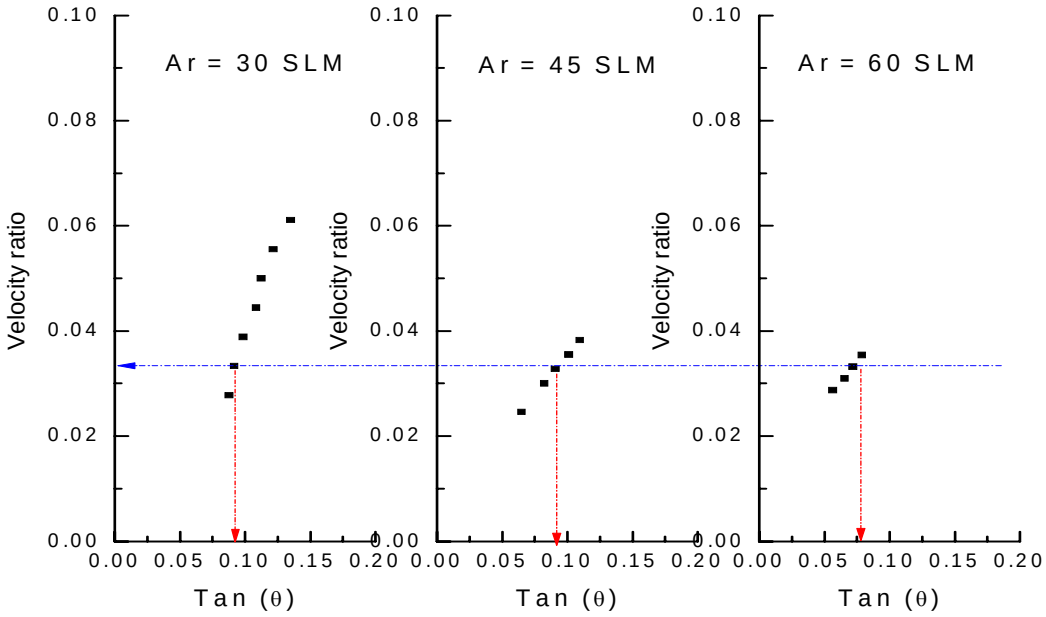

(b)

Figure 5-5 (a) Tan of plume angle and ratio of initial vertical velocity to the horizontal velocity at the spray distance as a function of carrier gas flow for different primary gas flows. The vertical black lines correspond to the optimum injection. Blue horizontal line intersecting the velocity ratio axis shows that optimum injection occurs at the same value of velocity ratio. The red horizontal line intersecting the tan (θ) axis shows that the optimum occurs at the same plume angle (b) Relationship between Tan of plume angle and velocity ratio (at optimum injection, identical plume angle as well as velocity has been obtained respectively)

5.3.2 Influence of Plume Angle on the In-flight Particle Behavior as A Function of Stand-off Distance

To examine the effect of stand-off distance on the in-flight particle state, the carrier gas, Ar, is injected from the side injector located at 8mm above plasma central axis to vary the plume angle, with the carrier gas flow rate varying from 1.5 SLM to 8 SLM in simulations and 2.5 SLM to 8 SLM in experiments.

Figure 5-6(a) shows the average particle surface temperature under different carrier gas flow rates at different spray distances. The corresponding average velocities are shown in Figure 5-6(b). The same trend has been obtained for all the spray distances. When increasing carrier gas flow rate from a lower level to a higher level, both the temperature and velocity will initially increase and then decrease after reaching a maximum value. The reason of this observation has been given in the previous section. For all the spray distances tested, particles get optimum temperature and velocity at 4 SLM carrier gas flow rate (corresponding to 5 degree plume angle), which agrees well with the experimental results. Also, it is clearly shown that this optimum plume angle is independent of spray distance.

It is also shown in Figure 5-6 that, by increasing the spray distance the particle temperature keeps decreasing. The particle velocity, however, firstly increases and then decreases. The above observations are explained as following. Once the plasma jet reaches its highest temperature, temperature and velocity of the plasma plume decrease with increasing spray distance. This is because that, while increasing the spray distance, the ambient cool air has more chance to exchange heat with the plume as well as the particles. This explains the decreased particle surface temperature with increasing spray distance. For the velocity part, on the one hand, the plasma plume accelerates the in-flight particles. On the other hand, the ambient air decelerates the particles. The combination of these two effects can explain the velocity trend with spray distance. The particle velocity keeps increasing for shorter spray distance where the plume accelerating effect is more prominent. It decreases for a longer spray distance where the particle deceleration caused by the ambient air is more prominent.

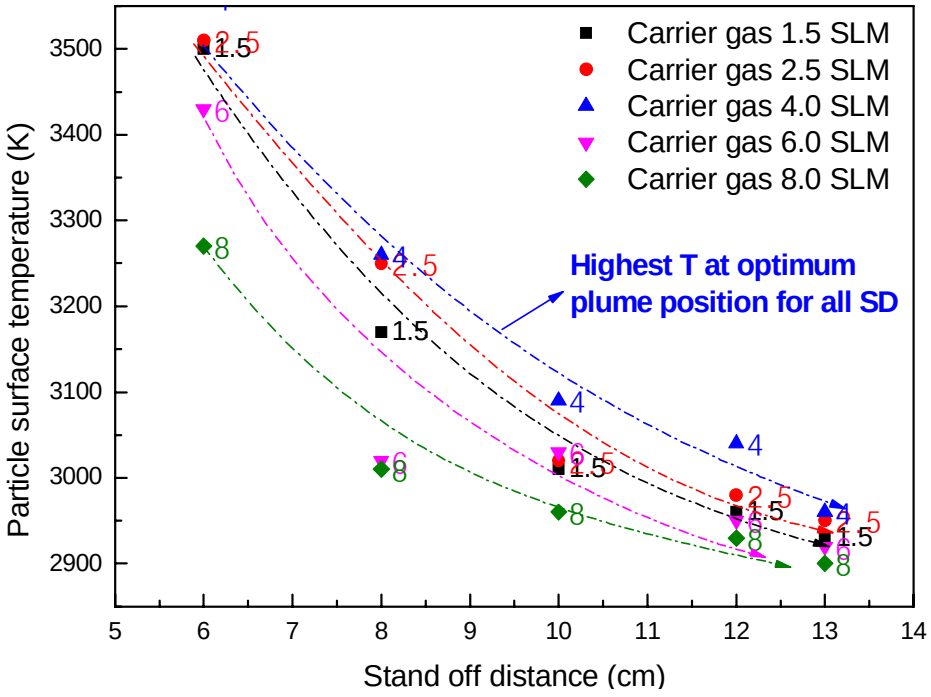

(a)

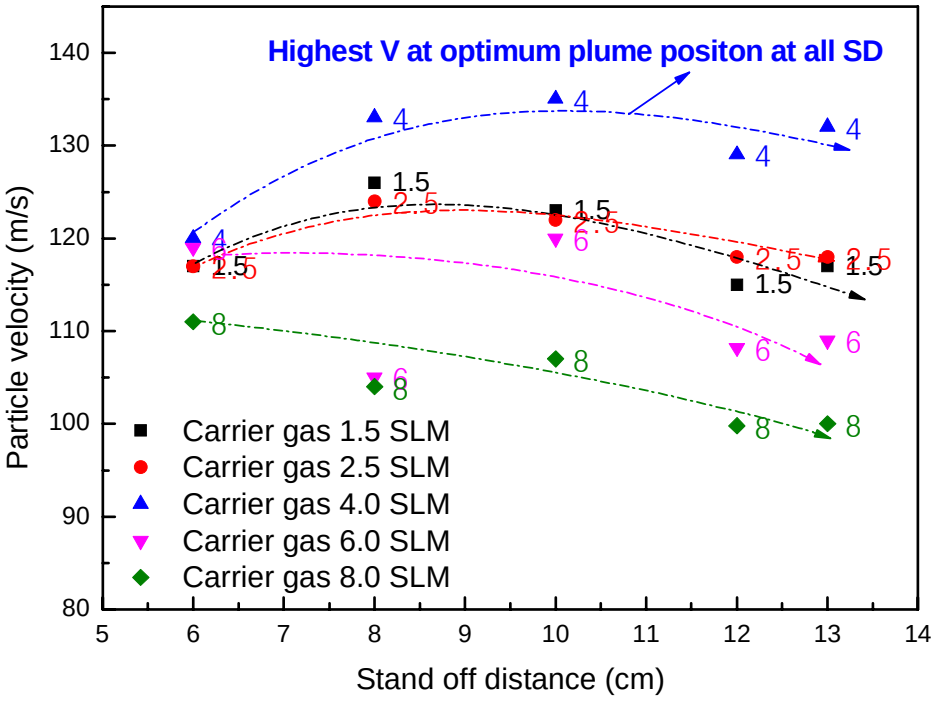

(b)

Figure 5-6 Mean values of (a) temperature, and (b) velocity at different stand off distances for carrier gas flow rate varying from 1.5 SLM to 8.0 SLM, highest T and V have been obtain at 4 SLM carrier gas flow corresponding to optimum plume angle

5.3.3 Effect of In-flight Particles on Plasma Plume

In experiments, it is difficult to observe the influence of in-flight particles on the plasma plume even though the particle status can be obtained from diagnostic sensors for certain spray distances. In chapter 4, particle injection caused plume temperature change has been identified in simulation. Here, with the help of simulation, this effect will be quantified in detail from the source terms coupling the particle to the gas equations.

To investigate the effect of in-flight particles on plasma plume, simulations were performed for the cases with or without particle injection. Figure 5-7 shows the temperature profiles for plasma plume under different particle feeding rates. Figure 5-7(a) shows the plume temperature profile for the case without carrier gas and particle injection. It is seen that the temperature field of plasma plume is symmetric about the torch axis. Figure 5-7(b) and Figure 5-7(c) show the temperature profiles for the cases with the carrier gas flow rate of 4 SLM and the feeding rate of 2g/min and 20g/min, respectively. The predicted plume temperature profile shifts downwards with the

injection of carrier gas and particles. Particle heating affects temperature change dramatically (see ellipses in Figure 5-7). It can be concluded that increasing particle feeding rate results in larger extended isothermal lines due to the particle heating effect.

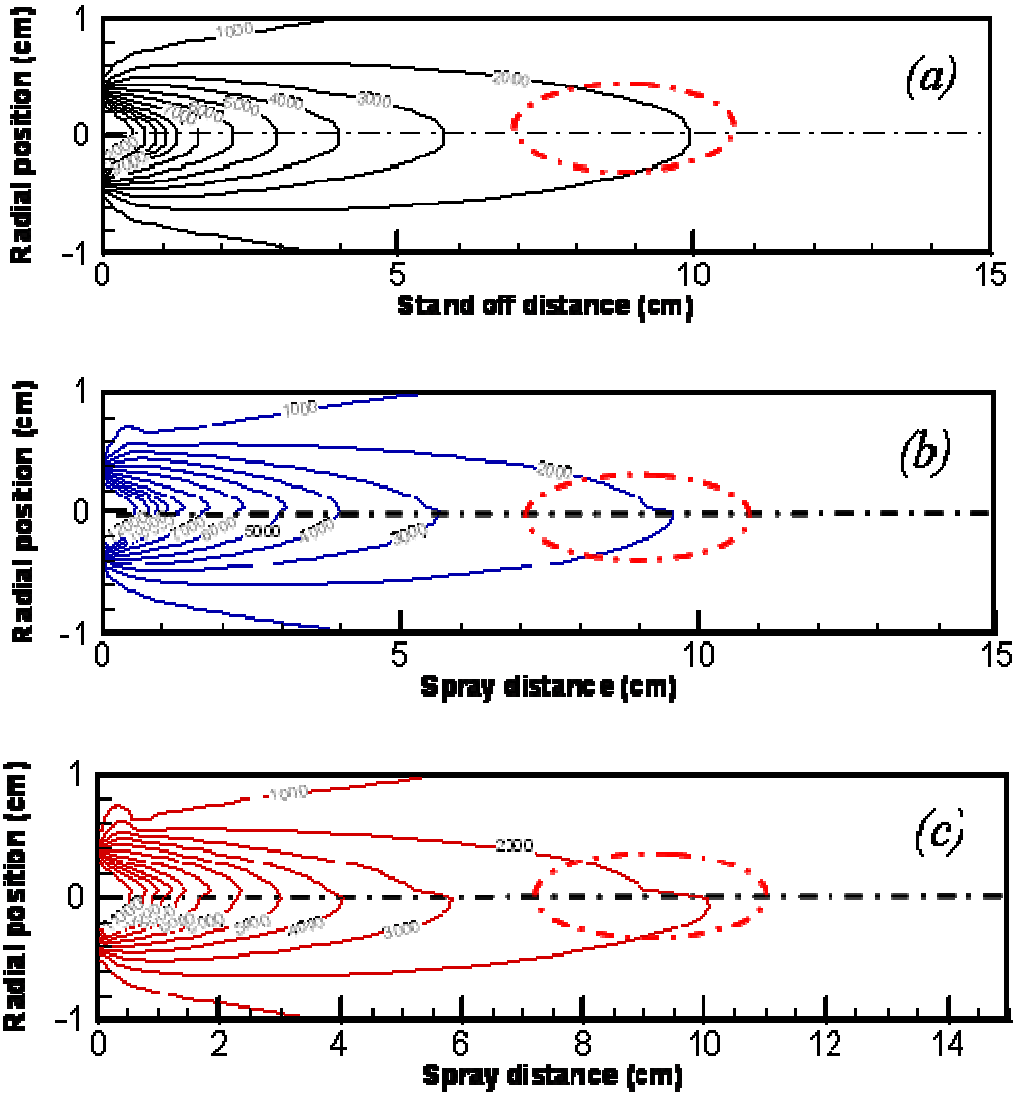

Figure 5-7 Temperature profiles of plasma plume for 30 SLM primary gas flow case: (a) without carrier gas and particle feeding, (b) 2 g/min feeding rate and (c) 20 g/min feeding rate

5.4 Conclusion

Experiments and simulations have been conducted to investigate the effects of process parameters on the characteristics of plasma jet and in-flight particles. It is observed in experiment and simulation that increasing primary gas flow rate results in firstly decreased then increased particle velocity, while particle temperature reduces

monotonically. This phenomenon has been explained in detail by considering interaction of plume temperature and velocity due to primary gas flow rate change. Maximum average temperature and velocity at any given spray distance has been studied experimentally and numerically. It is found that particle temperature decreases with increasing spray distance, while particle velocity first increases and then decreases.

Both experiment and simulation results show that particle temperature and velocity will initially increase with increasing plume angle and then decrease after reaching a maximum value. This trend has been observed at the same plume angle for different combinations of process parameters. Theoretical analysis shows that the plume angle is related to the velocity ratio of vertical contribution from carrier gas to the horizontal one from primary and secondary gas. Effect of particle injection on plasma plume has been further studied numerically. The effect of particle feeding rate on plume temperature has been studied. It is shown that studies in this chapter enable better understanding of influence of processing parameters on particle in-flight characteristics, which will help to realize process optimization.

Chapter 6 Generic Correlation of Spray Distance with In-flight Particle Behavior for Different Kinds of Materials in APS

6.1 Introduction

Optimizing the process parameters involved in plasma spraying is complex due to the large number of parameters (about 60) involved in this process[70, 101]. Significant efforts have been directed to understand the influence of process parameters (primary and secondary gas, plasma power) and their relationships with morphology and properties of molten particles upon impact, and eventual coating properties. Even though experiments have revealed the dramatic influence of spray distance on particles in-flight behavior and subsequent coating quality[55, 114-117], understanding the correlation between spray distance and in-flight particle status for different feeding stocks is insufficient due to the following reasons:

- Firstly even though diagnostic sensors realized on-line monitoring and control of the particle in-flight behavior, stable and repeatable experimental data for multi-spray distances is still insufficient due to the time, feeding stock consuming and erosion of spray nozzles.
- Secondly, it is also not safe to perform diagnostic experiments at a short spray distance (less than 50mm in APS).
- Finally, the direct measurement of particle molten status is difficult in the experiments. The average particle surface temperature is not a good indicator for particle molten status, especially for ceramic particles. Zhao et al. [143] found that the APS Al_2O_3 particles are not fully melted even though the average particle surface temperature is much higher than the melting point. Zhang et al. [152] introduced melting index to quantify the particle melting status and validated the theory with experiments. Recently, both experiment [53] and simulation [39] revealed that the statistical particle temperature distribution provided more information on particle molten status [11-13].

Modeling of plasma spray process has received considerable attention during the last few decades [64, 71, 141, 153-156]. Approaches to optimize the plasma spray processes have been tried through combining numerical simulations and experiments [70, 117-119]. However, no systematic study was carried out to examine the statistical distributions of in flight particle characteristics for different kinds of materials.

This chapter will investigate the influence of spray distance on in-flight particle status experimentally and numerically for Yttria Stabilized Zirconia (YSZ), Mo and NiCrAlY spray powders in Ar-H_2 plasma. The distributions of individual particle characteristics such as temperature, velocity and size at the point of the maximum particle flux were measured for a few plume cross-sections using DPV-2000. Numerical

simulations were performed using the same conditions applied in experiments. The in-flight particle characteristics and their distributions were studied for different spray distances to reveal the heating and melting process of different kinds of materials, such as metal, alloy and ceramics powders. The correlations between powder properties and spray conditions have been established.

6.2 Experiment and Simulation Setups

The plasma spray process has been illustrated in Figure 1-1. The feed stock powders are injected radically by an Ar carrier gas into the Ar-H_2 DC plasma flame, using a 9 MB plasma torch (Sulzer Metco). The operating conditions used in the modeling and experiments are listed in Table 6-1. The injector is located at 8 mm above the plasma central axis, and 6 mm from the plasma torch exit. The commercial available YSZ, Mo and NiCrAlY powders are used. The size distributions are measured by a Beckman Coulter 2 LS 13 320 Laser Diffraction Particle Size Analyzer [157], as shown in Figure 6-1. The particles selected exhibits spherical morphology. For each kind of powder, the plasma torch moves from 130mm to 100mm, 80mm and 60mm spray distance, respectively. The torch is moved from a longer distance to a shorter one in the consideration of safety. The chosen of spray distance is based on experience that the longer one favors resolidification of molten particles while the shorter one may cause the substrate melting.

Plasma plume characteristic and particles in-flight status such as temperature, velocity and diameter are measured by the diagnostic system [53, 151, 158], which includes the commercially available 'Tecnar DPV 2000' [45, 151] for particle in-flight states (temperature, velocity and size for 'single particle'), IPP (In-flight Particle Pyrometer) for particle average temperature in the ensemble volume and SPT (Spray Position Trajectory) for the plasma plume profiles. For each spray distance, diagnostic data was collected in a single point measurement mode from DPV 2000, which means the sensor head 'auto-centers' to the maximum particle flux location ('flux center') and makes measurements of particle velocity, temperature and size.

The detailed computational domain and boundary conditions used in the plasma jet calculation can be found in Chapter 3 and in literature [141].

As listed in Table 6-1, same operating conditions have been used in experiments and 3-D simulations. The particle conditions and thermo-physical properties of feeding stocks are presented in Table 6-2.

Table 6-1 Operating conditions used in the experiments and modeling

Processing parameters	Experiment			Simulation		
Feedstocks	YSZ	NiCrAlY	Mo	YSZ	NiCrAlY	Mo
Primary gas, Ar, SLM[a]	40	40	47		40	
Secondary gas, H_2, SLM	8	8	6		8	
Current, A	600	600	575		600	
Voltage, V	64.0	64.0	60		64.0	
Carrier gas flow rate, Ar, SLM	4.0	4.0	3.0		4.0	
Spray distance, mm	YSZ & NiCrAlY: 60, 80, 100, 130 Mo: 50, 70, 100, 130				10-150	

[a] SLM means standard liter per minute; 1slm=16.67 $cm^3 s^{-1}$

Table 6-2 Operating conditions and properties of the feedstocks

Parameters	Values		
Feeding stocks	YSZ	NiCrAlY	Mo
Feeding rate, g min^{-1}	2.0	2.0	3.7
Mean size, μ m	55	50	24
K_s, $Wm^{-1}K^{-1}$	2.0	74	84
K_l, $Wm^{-1}K^{-1}$	2.32	43	46
$C_{p,s}$, $JKg^{-1}K^{-1}$	580	448	339
$C_{p,l}$, $JKg^{-1}K^{-1}$	713	448	570
ρ_s, g cm^{-3}	5.89	8.1	10.2
ρ_l, g cm^{-3}	5.89	8.1	9.35
Minimum T_m, K	2950	1360	2895.1
Maximum T_m, K	2950	1411	2895.1
L_m, $KJKg^{-1}$	707	299	375.3
L_{evap}, $KJKg^{-1}$	6000	7330	6150

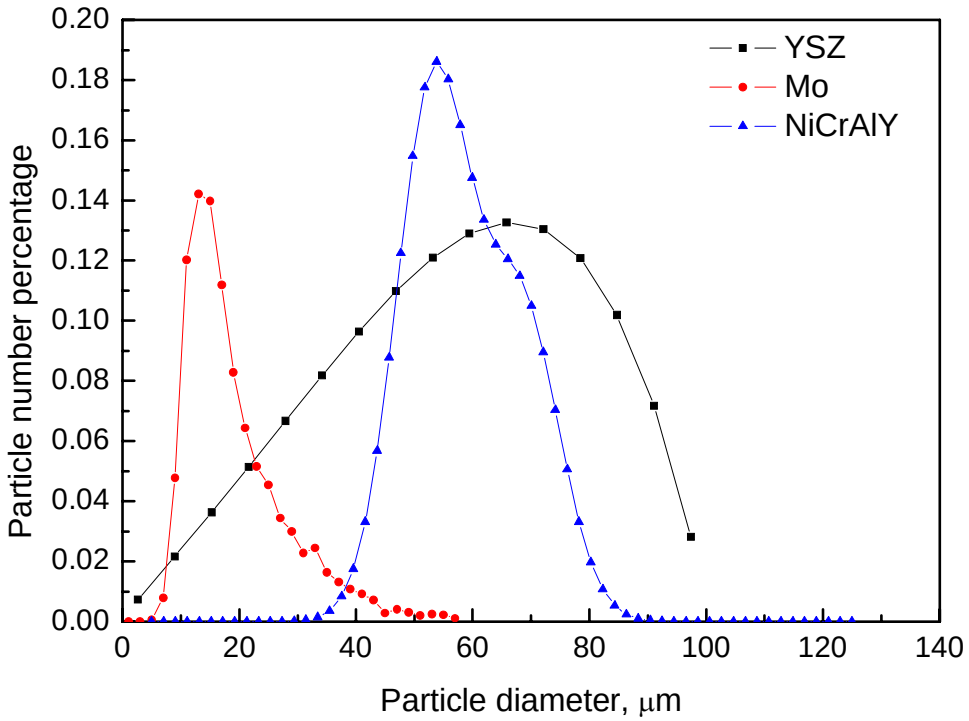

Figure 6-1 Initial size distribution for the feeding stocks in experiment and simulation

6.3 Results and Discussions

6.3.1 Experimental Observation of Particle State at Multiple Spray Distances

In tradition, the average values are measured to represent the in-flight particle characteristics such as temperature, velocity, and size. The average values, however, cannot provide sufficient information representing the real status of particles. With the help of DPV-2000, in-flight characteristics for each single particle can be measured. The statistical distributions of the particle status can be obtained as presented in the flowing sessions.

6.3.1.1 Evolution of Particle Size with Spray Distance

Figure 6-2 shows the particle size distributions at different spray distances for YSZ. With the increasing spray distance the particle size appears to increase. The same trend can also be found for Mo and NiCrAlY when checking their size distributions at multiple spray distances. This effect can be clearly seen from the decreasing peak values for small sized particles (trend shown as red arrow in Figure 6-2) and shifting of the peaks to larger sizes when increasing spray distance. It is difficult to explain this observation based on experiments. However, it has been speculated that the maximum flux location that sensor reads shifts to the large particle size region. Another interesting phenomenon can be observed from Figure 6-3 when checking the average particle size

(at DPV flux center) for multiple materials at different spray distances. The mean particle sizes increase with spray distance with various slopes (YSZ the highest, NiCrAlY in the middle while Mo the lowest). It is difficult to explain these effects only based on experimental work, numerical simulation has been carried out for scientific understanding of these phenomena. The details can be found in the following sessions.

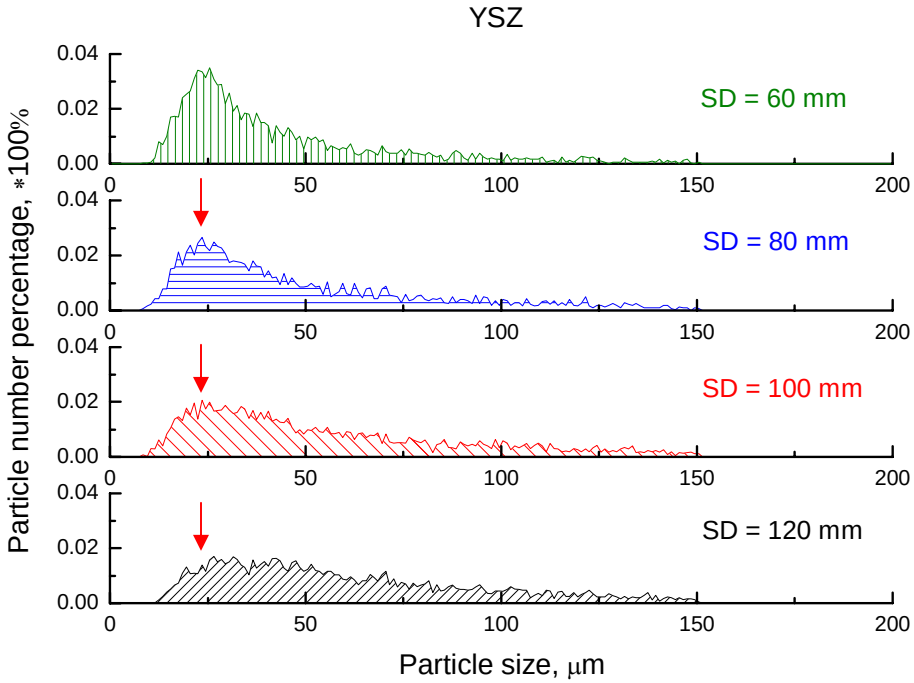

Figure 6-2 Statistical particle size distributions for YSZ at multiple spray distances (at flux center from DPV 2000)

6.3.1.2 Change of Particle Velocity with Spray Distance

Particle velocity distributions at different spray distances for YSZ, Mo and NiCrAlY have been studied experimental. Same statistical particle velocity distribution trend has been observed for the three tested materials. Figure 6-4 shows the statistical particle velocity distribution of Mo at different spray distances. It is observed that the whole velocity distribution moves to larger values initially and then moved back to small ones (trend is shown by the red arrows) when the spray distance increases. The mechanism behind this observation will be identified with numerical simulation results later in this chapter.

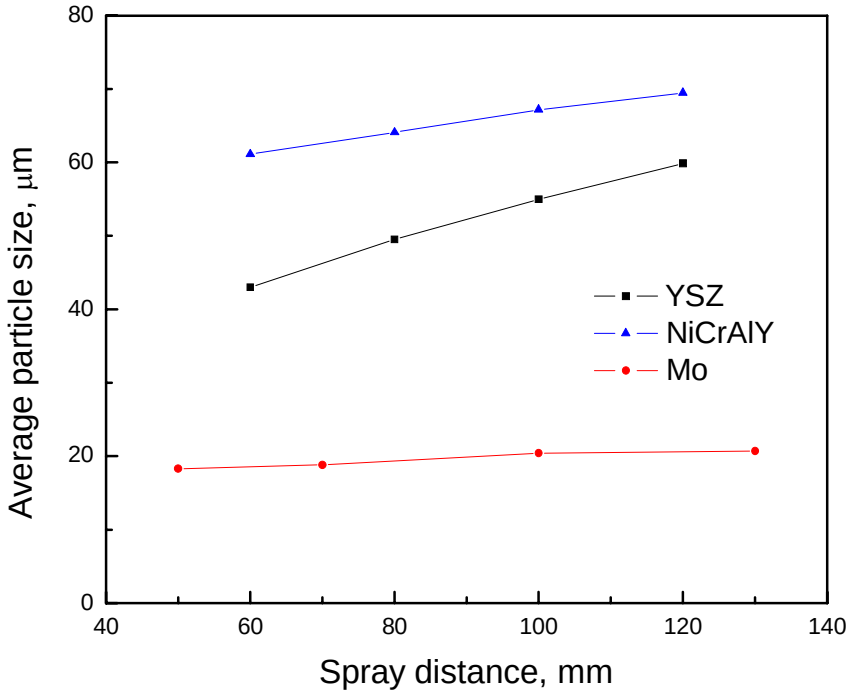

Figure 6-3 Average particle size for YSZ, Mo and NiCrAlY at multiple spray distances (at flux center from DPV 2000)

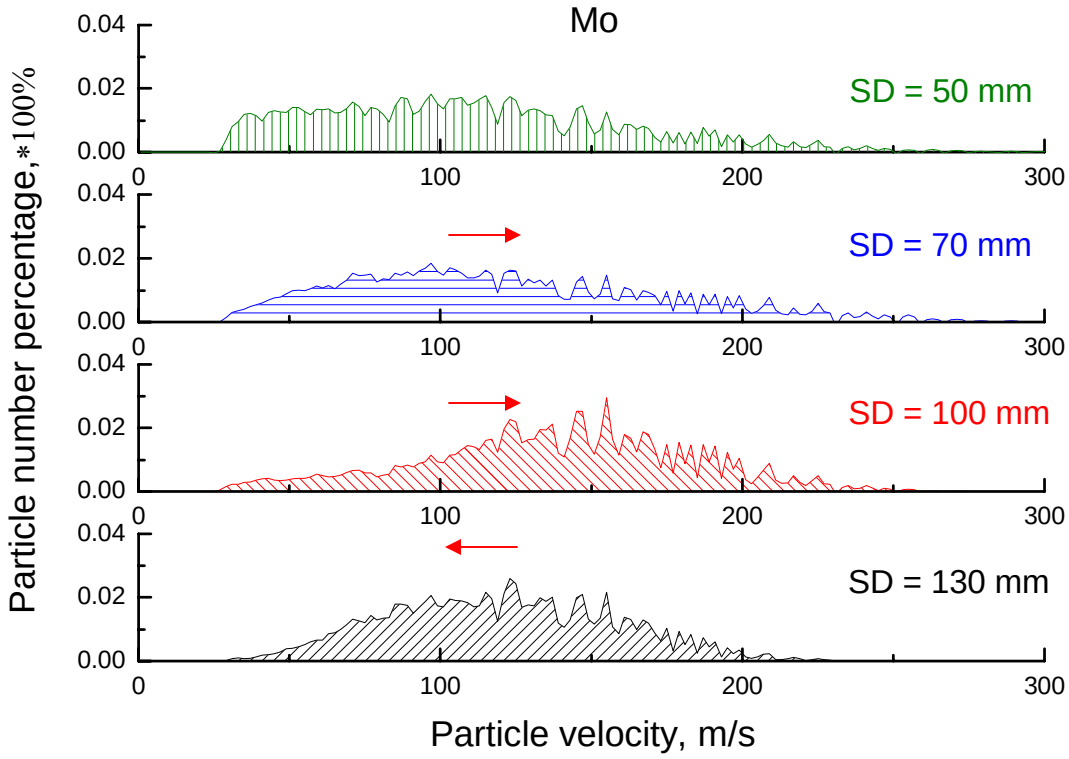

Figure 6-4 Statistical distributions of particle velocity for Mo, with increasing spray distance, the whole distribution initially shifts to large values and then shifts back to small ones

6.3.1.3 Particle Temperature at Multiple Spray Distances

Particle surface temperatures measured for YSZ, Mo and NiCrAlY are shown in Figure 6-5 (a)-(c) respectively. It is observed that, by increasing the spray distance, the peaks moved from high temperature to low temperature for all the three materials. The shapes of the statistical distributions for YSZ, NiCrAlY and Mo tend to change from wide distributions to the narrow peaks (the trend has been shown as the red arrows in Figure 6-5). To understand these experimental observations, numerical simulations are performed and results will be compared.

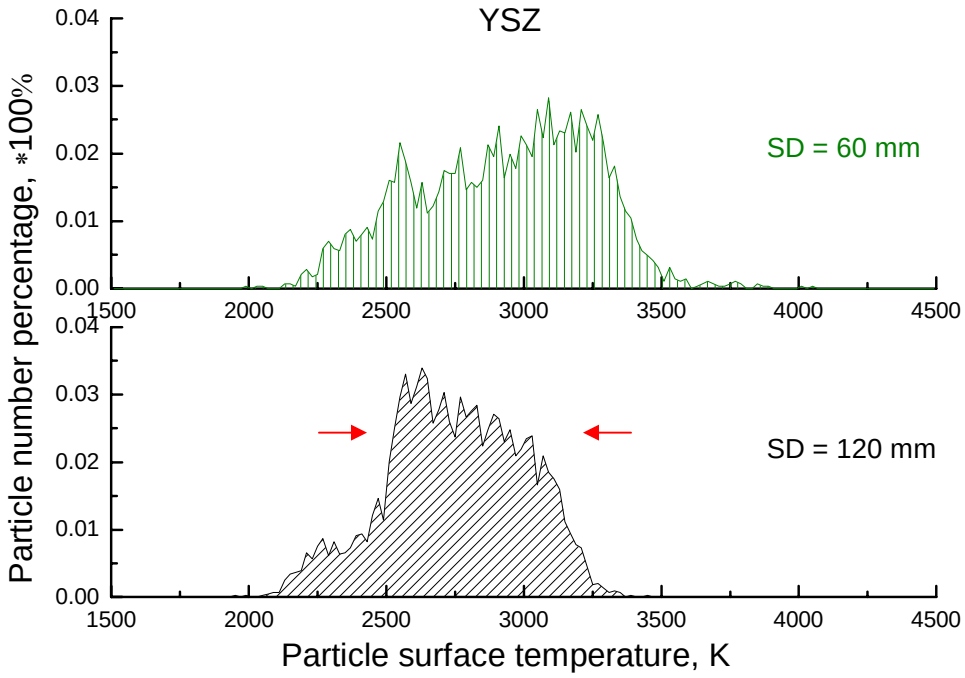

(a)

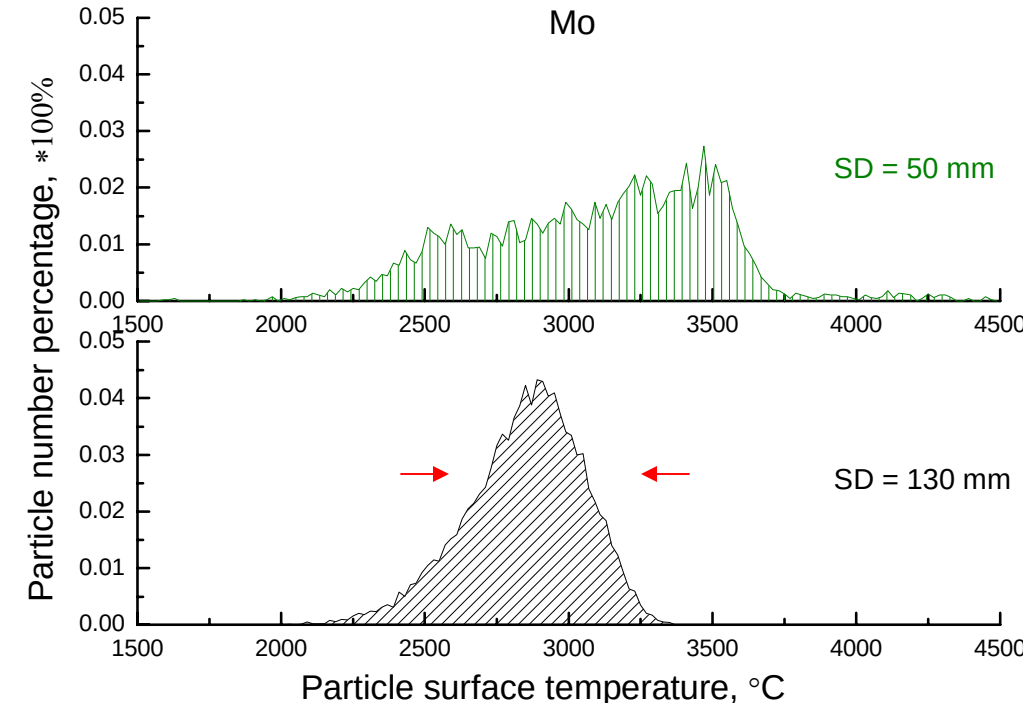

(b)

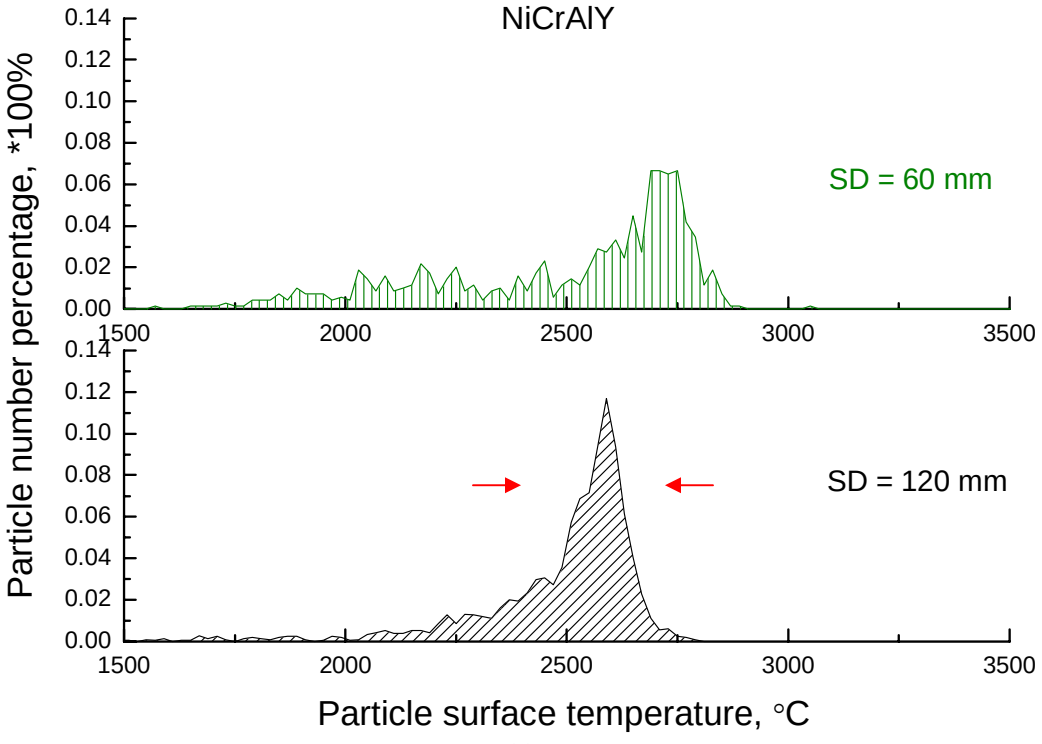

(c)

Figure 6-5 Statistical distributions of particle surface temperature for (a) YSZ, (b) Mo and (c) NiCrAlY

6.3.2 Simulation Results

6.3.2.1 Particle Trajectory and Particle Size Evolution with Spray Distance

The particle trajectory in plasma jet carries information of particle heating and acceleration history, which determines the particle molten status and kinetic energy at impact. Figure 6-6 shows the trajectories of different sized YSZ particles in temperature and velocity fields of plasma plume. It is evident that, at each spray distance, larger sized particles have more chance to penetrate through plasma plume. By increasing spray distance, large sized particles go far more downwards and penetrate through plasma jet due to their high momentum. In the mean time, the small sized particles got separated from the large ones with increasing spray distance. Figure 6-6 (c) shows the maximum flux location and trajectories of different sized particles at different spray distances. From the trajectories of different sized particles it is clearly shown that different sized particles separate more and more with increasing spray distances. It is also revealed that the maximum flux location moves downward into the large particle region. Table 6-3 shows the statistical temperature and velocity at the 'Flux center' for different spray distances. Here, the temperature and velocity show the same trend as those distributions obtained from experiment (see Figure 6-4 and Figure 6-5). In experiments, DPV2000 will find the maximum flux location and do the measurement. As spray distance increases, it is clear that DPV2000 will read the region of large sized particle since that is the maximum flux location. This explains the increasing particle size with spray distance in Figure 6-2(small sized particles have already separated from large seized ones at large spray distance). Considering the wider initial size distribution for YSZ shown in Figure 6-1, the size separation effect becomes more prominent with increasing spray distance for YSZ. This explains the difference in the slopes as shown in Figure 6-3(with the one for YSZ the largest slope, NiCrAlY in the middle, and Mo the lowest).

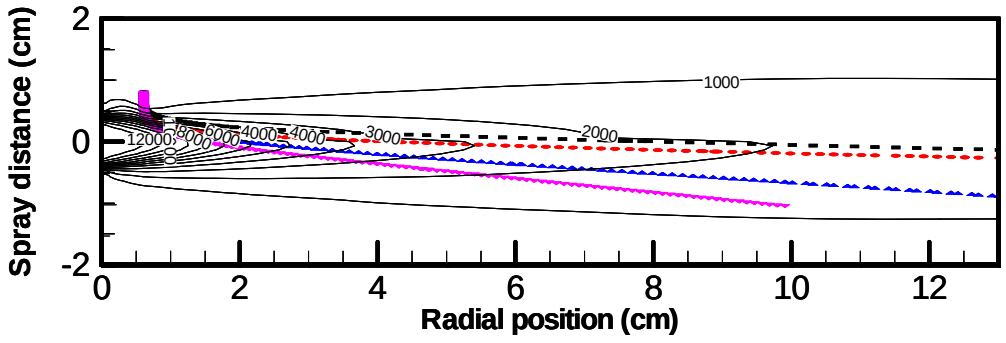

(a)

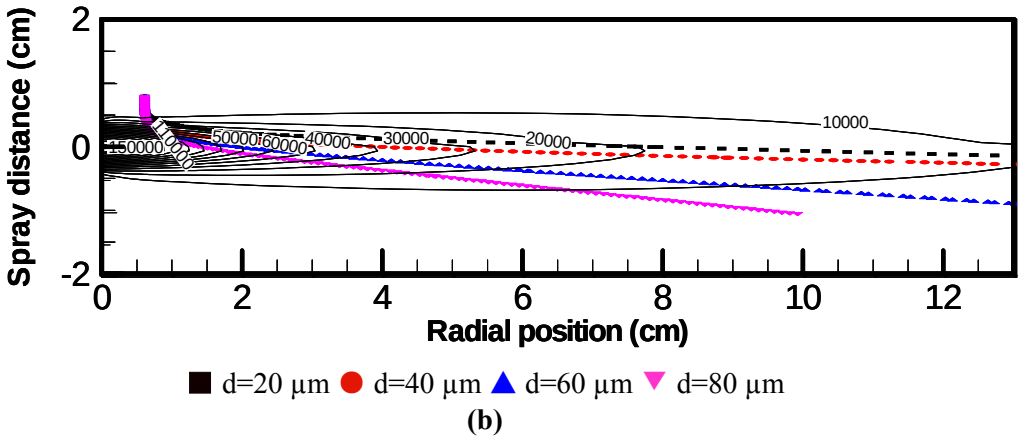

(b)

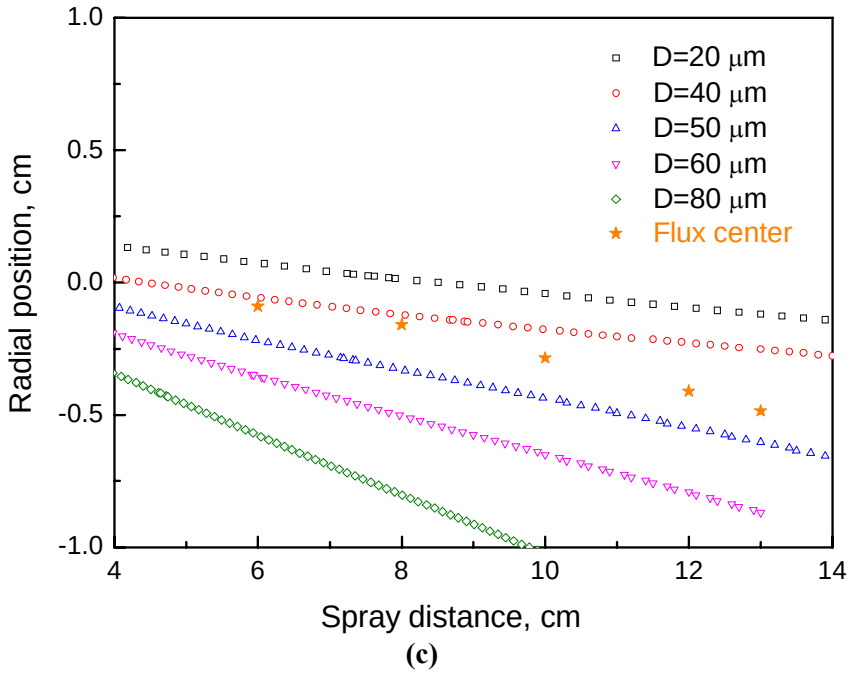

(c)

Figure 6-6 Trajectories of different sized ZrO_2 in (a) temperature and (b) velocity fields. (c) maximum flux location and particle trajectory for different sized particles at different spray distances

Table 6-3 Statistical values at 'Flux Center' for (a) temperature at different spray distance

SD, mm \ T, K	*40 μm*	*50 μm*	*Flux center*
60	4090	3895	4060
80	3860	3730	3820
100	3650	3580	3610

120	3550	3465	3490
130	3440	3410	3418

(b) Statistical velocity for 'Flux Center' at different spray distance

SD, mm \ V, m/s	*40 μm*	*50 μm*	*Flux center*
60	95	81	91.7
80	100	83	95
100	103	86	94.3
120	104	86	91.3
130	104	86	90.8

6.3.2.2 Change of Particle Temperature and Velocity with Spray Distance

From the contours of plasma plume temperature and velocity shown in Figure 6-6(a) and (b), it is clearly revealed that the high temperature region is much shorter than the high velocity zone in the plasma flume. Simulations show that particles can be heated to a very high temperature in a short spray distance, out of which they will be cooled down. On the other hand, for particle velocity, since the high velocity jet is comparatively long, particles can be accelerated in a longer spray distance before they are decelerated by ambient gases. The length difference of high temperature and velocity region explains the decreasing particle surface temperature and the initially increased and then decreased particle velocity as the spray distance increases, which explains the trend obtained from experiment as shown in Figure 6-4 and Figure 6-5.

Figure 6-7 shows the particle surface temperature and plasma gas temperature adjacent to the particle for YSZ and Mo. It is clearly shown that, for both ceramic and metal particles, small sized particles are heated up to a higher temperature than large ones for spray distance less than 5cm. When the spray distance is larger than 5cm, the flame temperature becomes lower than the particle surface temperature. Small sized particle is therefore cooled down quicker due to its low heat capacity and high surface-volume ratio that favor its heat exchange with the environment. This explains the reduced temperature difference for different sized particles as spray distance increases. This also explains the observation in Figure 6-5, i.e., with the increasing spray distance, the statistical temperature distribution becomes narrower.

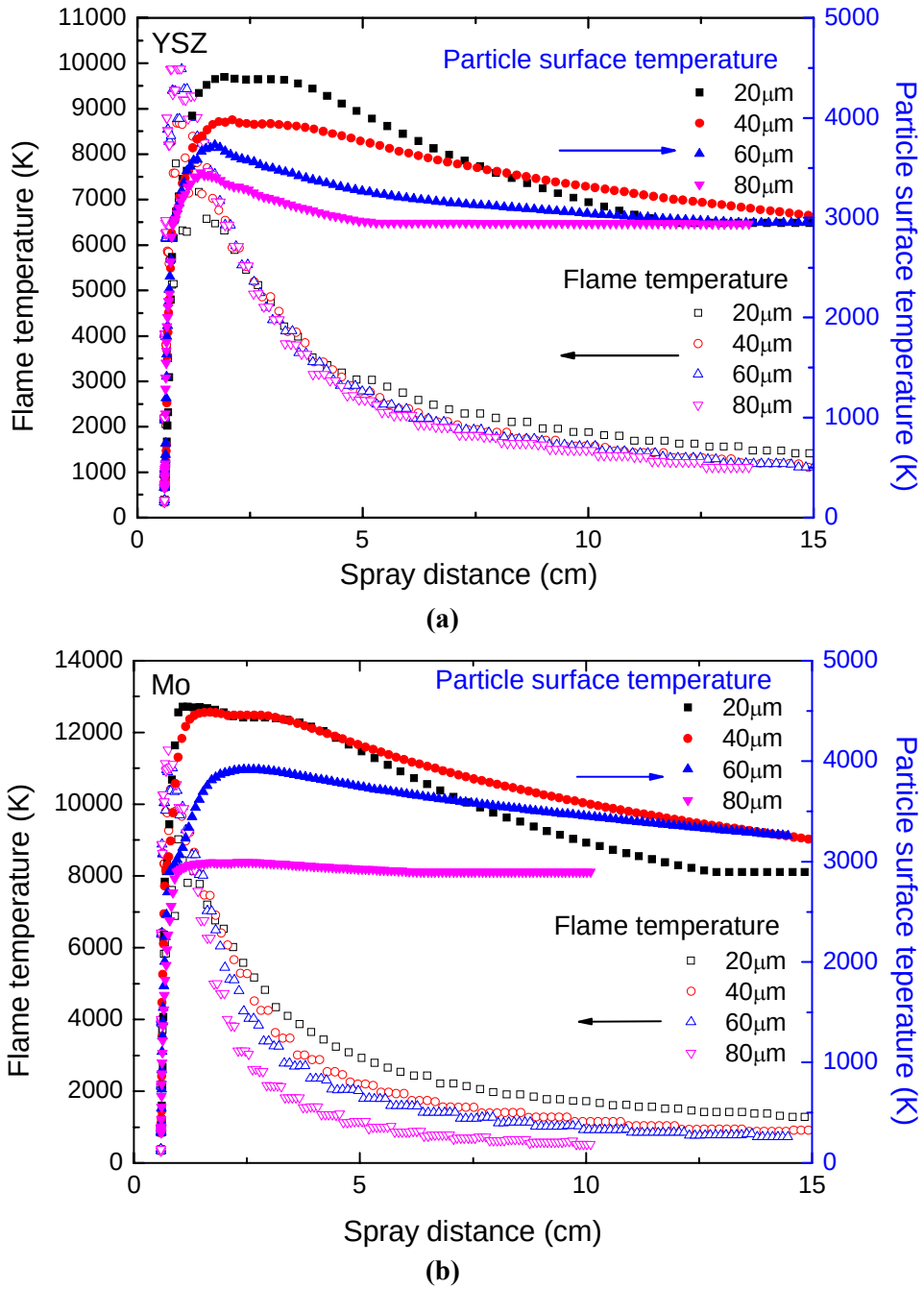

Figure 6-7 Flame temperature and Particle surface temperature for (a) YSZ and (b) Mo

6.3.2.3 Variation of Particle Molten Status with Spray Distance

It is difficult to obtain particle molten content directly from experiment. With the help of numerical simulation, single particle can be traced during the in-flight process. Not only plasma properties in vicinity of particles but the particle molten status can be successfully obtained by numerical simulation. Figure 6-8 shows the particle molten status (defined as the volume percentage of molten portion for each single particle) for

YSZ and Mo at different spray distances. It shows that Mo particles melt much faster than YSZ particles. The difference is even more obvious when comparing large sized Mo particles with the corresponding YSZ ones. Figure 6-8 (a) reveals that the large sized YSZ particles are difficult to melt. It is also found that, at a short spray distance, even though the surface temperature of YSZ particle is much higher then its melting point, as shown in Figure 6-7 (a), it is not fully melted, as shown in Figure 6-8 (a). At a long spray distance, the molten status decreases due to particle re-solidification. It is shown in Figure 6-8 (b) that, for metal particles, as long as the particle surface temperature is higher than melting point, they will be fully melted. The molten status difference between YSZ and Mo particles can be explained by the large difference of thermal conductivity between ceramics and metals (in this case, the value for Mo and NiCrAlY is 20 times larger than the one for YSZ). The particle Biot numbers therefore differ greatly between metal and ceramic materials. Since Mo and NiCrAlY particles have a small Biot number, temperature distribution inside the particles are expected to be uniform. While for YSZ particles, a large temperature difference is expected in the particles, especially for the large sized ones.

Based on the above observations, it is concluded that, for metal and alloy, particle surface temperature is a good indicator for particle molten status. While for ceramics, due to high Biot number, particle molten status is difficult to measure. Also re-solidification may occur in the semi-molten particles, especially for the larger sized ones.

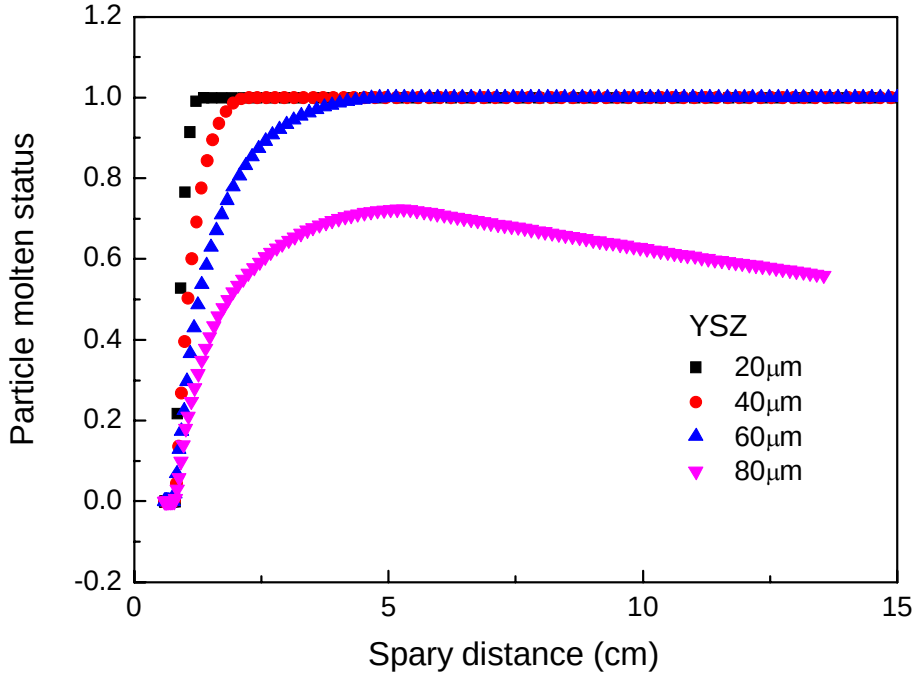

(a)

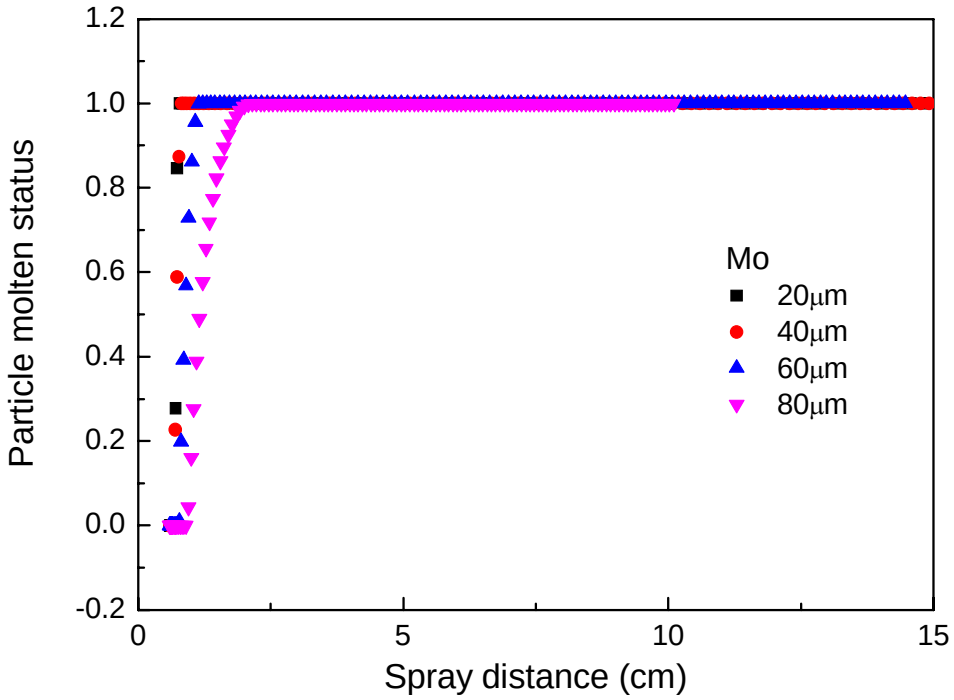

(b)

Figure 6-8 Numerical simulation results of particle molten status for (a) YSZ and (b) Mo

6.4 Conclusion

Experiments and simulations have been performed to investigate the influence of spray distance on in-flight particle status for Yttria Stabilized Zirconia (YSZ), Mo and NiCrAlY in air plasma spray process.

To reveal the heating and melting process of metal, alloy and ceramics powders, experiments were conducted to study the in-flight particle characteristics and their distributions at different spray distances. By analyzing the particle size, velocity and temperature distributions at different spray distances, the maximum particle velocity and temperature at a certain spray distance can be determined for ceramic, metal and alloy powders. It is revealed that the statistical distribution for particle temperature becomes narrower as spray distance increases.

Numerical simulations were conducted and results have been used to explain the particle behaviors observed in experiments. The location of the maximum flux is shifted from small to large particle size, which explains the increase of particle size reading in the experiments as spray distance increases. Rapid cooling down of small sized particles at a long spray distance explains the narrowing of statistical temperature distribution as spray distance increases. It is also revealed that particle surface temperature is a good

indicator for metal and alloy particle molten status. For ceramics, however, due to the low thermal conductivity and large heat capacity, determination of particle molten status becomes more complicated. Also, re-solidification may occur for semi-molten particles, especially for the larger sized ones.

Chapter 7 A Universal Method for Representation of In-Flight Particle Characteristics in Thermal Spray Processes

7.1 Introduction

In recent years, the advent of user-friendly process and particle diagnostic tools has percolated the thermal spray industry. These devices have played a pivotal role in enhancing not only our ability to comprehend the complexities in thermal spray processes, but also allows for minimizing variability and enhancing reliability. A variety of diagnostic strategies are available to measure particle parameters in the thermal spray processes. They range from sophisticated to rudimentary based on the measurement method, interpretation and analysis. Many of these sensors have now been successfully utilized within the harsh confines of the spray booth.

The principle objectives of these diagnostic devices are to measure the spray plume characteristics: namely the particle velocities, temperatures, trajectories and size distributions. The basis of this interest relies on a widespread appreciation that the in-flight particle velocity, temperature, and size, to a first approximation, determine the nature of the microstructure and properties of sprayed coatings [47, 69, 120-122]. Different strategies are employed to meet these requirements. They include measurement of *individual particle* parameters within the spray stream (e.g. Tecnar DPV 2000 and Inflight™ integrated particle sensor) as well as *ensemble particle* sensors for group measurements of particle velocities and temperatures (e.g. Tecnar Accuraspray, Oseir Spraywatch, Inflight Particle Pyrometer, Stratonics Thermaviz etc.)[45, 47, 53, 123-125]. Many of these sensors measure particle temperatures through the use of thermal emission emanating from a molten/semi-molten traveling particle, and, use time-of-flight measurements to extract the particle velocities. Generally the velocity measurements can be measured with reasonable accuracy. However, the estimation of particle temperatures introduces inaccuracies as they rely on knowledge of emissivity of a material[45]. Furthermore, given the dynamic nature of the process, with associated gradients in chemistry and temperature within a given particle, true determination of particle temperatures continues to offer significant challenges. Nevertheless comparative representation due to effect of process parameters provides opportunities for both process design and reliability assessment.

A direct measurement of particle melting status is extremely difficult since pyrometric technique only provides access to the particle surface temperature. For temperature measurements, the measured emission is principally from the surface of a particle and, in general, does not provide information on the bulk temperature of an entire particle. This is particularly important for widely used refractory ceramics such as yttria stabilized zirconia (YSZ), due to its low thermal conductivity resulting in large

temperature gradient along the radial direction. For instance, the particle surface may begin to evaporate even before the core melts, which means surface temperature is not adequate to describe the melting status. For metallic materials sprayed under atmospheric conditions, in-flight oxidation of the particle can affect the reported temperature reading, and the applicable emissivity values can potentially be erroneous. Most sensors measure temperature at a given location and does not take into account in-flight time for a traveling particle. Given large differences in melting points, it is difficult to cross-correlate across a variety of materials systems.

In recent years, a number of efforts are underway to enhance the utilization of the diagnostic sensors across the spectrum of thermal spray materials and processes. Vaidya et al [61, 159] first introduced the concept of *Melting Index* (M.I.) to describe the molten state of a given particle by normalizing the measured surface temperature with the dwell time and size. In its simplest rendition this is assessed as:

$$M.I. = \frac{T \Delta t_{fly}}{D} \tag{7-1}$$

where T is the measured particle surface temperature, K, D is the particle size, m, and ΔT_{fly} is the particle in-flight time, s, which has the following expression:

$$\Delta T_{fly} = \frac{2L}{V} \tag{7-2}$$

In which, L is the spray distance, m, and V is the particle velocity, m/s

Through this approach and using the output of DPV 2000 (individual particle velocity, temperature and size), it is possible to cross compare melting status for a given material across different process conditions. It, however, does not allow comparisons amongst a wide array of materials within a given process. In addition, Equation (7-1) does not revel whether or when a particle will start to melt, since it does not contain the information of materials' melting points as well as other properties. Zhang et al [73] significantly enhanced the scientific description of melting index through the thermal resistance and energy balance analysis. They define M.I. as the ratio of particle residence time in the flame, ΔT_{fly} , to the total melting time (the total time needed to melt the particle), ΔT_{melt}, e.g.,

$$M.I. = \frac{\Delta t_{fly}}{\Delta t_{melt}} = \frac{24k}{\rho h_{fg}} \cdot \frac{1}{1 + 4/Bi} \cdot \frac{(T_f - T_m) \cdot \Delta t_{fly}}{D^2} \tag{7-3}$$

where k is the thermal conductivity, W/mK, ρ is the density of the material in liquid state, kg/m^3, h_{fg} is the enthalpy of fusion, J/kg, and T_f is the flame temperature near the in-flight particle, K. T_m is the melting point of the material, K, D is the particle size, m, and B_i is the Biot number, defined as:

$$B_i = hr_p / k \tag{7-4}$$

where h is the heat transfer coefficient, W/m^{2}K.

An advantage of the Zhang's approach is its non-dimensionality, which allows for cross-comparison of melting state among a range of materials. This is a very valuable tool in process diagnostics since a range of thermal spray processes are available. From Equation (7-3) it can be clearly seen that, if the flame temperature is higher than the melting point of the material, the particle begins to melt and a positive M.I. value will be obtained. Otherwise, the material will not be molten. A M.I. value of 1 means that the in-flight time equals to the time needed to get the particle fully molten. A M.I. equals to or higher than 1 corresponds to fully molten particles. It is therefore clear that, from the value of M.I. one can judge if the particle is partially molten ($0 \leq$ M.I. < 1), fully molten (M.I.>=1) or unmolten (M.I.<0). By comparing the M.I. values of different particles for either different process conditions or multiple materials, one can determine how well the particles have been melted (positive M.I. values) or how far are the particles from the onset of melting (negative M.I. values). Certain uncertainties, however, do remain in Equation (7-3). For instance, the heat transfer coefficient in Equation (7-3) can only be obtained from numerical modeling[73]. In addition, particle surface temperature, T, has been used to calculate M.I. considering the integration of thermal energy exchange history between the in-flight particles and their environment, since it is difficult to monitor the real time flame temperature in the vicinity of the flying particles.

Similar to M.I., Vaidya et al [159] also used particle *Reynolds number* as another non-dimensional method for describing the kinetic state of a particle.

$$\mathrm{Re} = DV\rho / \mu \tag{7-5}$$

where μ is the dynamic viscosity, kg/ms.

It has been shown both experimentally and theoretically that Re has significant effect on particle impact, spreading and splat formation during thermal spray due to the fact that the parameter considers both the particle in-flight status and the material properties essential to droplet impact and splat flattening[122, 160-163]. Again, this has the advantage that it is non-dimensional and non-material specific, which provides a powerful approach to compare among multiple materials and processes. It does, however, require knowledge or estimation of material viscosity in the melting state, which can be obtained from handbooks and open publications. Deposition efficiency (DE) and splat and coating qualities are significantly affected by molten status. It is essential to represent particle status at impact using the material viscosity in the molten state due to the fact that the studied object in this case is the molten particles, i.e. the fluid that is moving with a certain speed.

It should be noted that in Equation (7-5) the particle Reynolds number in stead of the fluid Reynolds number is used. The fluid Reynolds number which is used for calculation of the drag force exerted on the in-flight particles takes the form as:

$$\mathrm{Re} = \frac{\rho_f D_p \left| \widetilde{V} + V' - V_p \right|}{\mu_f} \tag{7-6}$$

where D_p is particle diameter, V' is the velocity fluctuation, $\widetilde{V}$, ρ_f and μ_f are the velocity, density and viscosity of gas phase around the particle, respectively, and V_p is the particle velocity. Since the drag force of a particle is caused by the gas surrounding it, the dynamic viscosity of the gas is used in the above equation to calculate the *Re*. This parameter plays essential role for in-flight particle drag force calculation as well as the transport properties[141]. It is, however, not relevant to the particle status at impact.

In addition to Reynolds number, the in-flight particle kinetic energy can be used to capture the velocity component. In the kinetic energy equation

$$KE = \frac{1}{2} m V^2 \tag{7-7}$$

where m is the mass of particle, which can be calculated from the in-flight particle size estimation from single particle sensors relating to $m = \frac{1}{6}\pi\rho D^3$. This realizes the consideration of process from the stand point of kinetic energy, which is an important component at impact determining the extent of spreading, flattening and the nature of splat-substrate and splat-splat contact [86, 164, 165]. The advantage of using kinetic energy over Reynolds number is the square component of the velocity, which is a better descriptor of the energy state. The disadvantage is that it is not non-dimensional.

In contrast to ceramics, oxidation is an important attribute of metallic particle in-flight behavior.[78, 126-128]. Not withstanding issues with coating properties, in-flight oxidation can affect diagnostic measurement itself due to changes in particle state. Furthermore, oxidation reactions are exothermic and can boost the metallic particle temperature well beyond the thermal spray imparted heating zone. Zhang et al employed an order-of-magnitude analysis and one dimensional thermal network model to investigate the heat and mass transport from the plasma flame to the particles. They derived a dimensionless parameter, *Oxidation Index(O.I.)*, to characterize the oxide content of the in-flight particles[73].

$$O.I. \approx \frac{6\left(Y_{o,f} - Y_{o,c}\right)}{\rho_l} \frac{W_{ox}}{W_o} \frac{\mathrm{Sh}\,\rho_f D_{o,f}}{d_p} \frac{S}{V_P d_p} \propto \frac{S}{V_P d_p^2} \tag{7-8}$$

where $Y_{o,f}$ and $Y_{o,c}$ are the oxygen concentration in the gas phase and in the particle center, respectively, W_o and W_{ox} are the atomic weight of the oxidant and the oxide product, respectively, *Sh* is the Sherwood number and it is defined as $Sh = \frac{2h_m r_p}{\rho_f D_{o,f}}$, $D_{o,f}$ is the diffusion coefficient of the oxygen in the plasma flame, ρ_f is the Favre-averaged gas density around the particle and h_m is the mass transfer coefficient between the particle surface and the environment. It should be noted that the mass transfer coefficient and

the oxygen concentration surrounding the particles, which are critical in the O.I. calculation, can only be estimated from numerical simulation, since it is difficult to measure the real time values in experiments. Equation (7-7) also reveals that the oxide content increases monotonically with the spray distance, and decreases with increasing particle size and velocity. Instead of using the explicit equation provided earlier, values of $\frac{S}{V_P d_p^2}$ can be used to approximate O.I. [73, 166]. It has been shown that plotting the experimentally measured oxide content against the O.I. calculated based on S, V_p and d_p provides reasonable agreement. This method, however, can be only used to compare oxidation level of a certain feed material under different torch operating conditions, but nevertheless represent another valuable representation tool as part of the overall process map strategy.

As discussed in the previous chapters, splat thickness is an important parameter for splat cooling and grain size, which relates to coating properties. Various models have been developed to predict the splat geometry or flattening ratio in the literature. Wan et al.[167] correlated the splat-flattening ratio with the particle and the substrate parameters based on the mechanical energy balance between the kinetic energy, potential energy and the work done by the frictional force. The splat flattening ratio can be calculated from the Reynolds and Jakob numbers and has the following expression:

$$\xi = \left[\sqrt{\frac{Ja}{2\,\mathrm{Pr}} \frac{k_s}{k_l} + 1} - \sqrt{\frac{Ja}{2\,\mathrm{Pr}} \frac{k_s}{k_l}} \right]^{0.4} \left(1.18\,\mathrm{Re}^{0.2} \right) \tag{7-9}$$

Equation (7-9) is only true when the substrate temperature remains constant or thermal conductivity of the substrate is much higher than that of the impact particle. Zhang et al.[107] modified Eq. (7-9) to include temperature distribution in the substrate by re-defining the Jakob number:

$$Ja = c_{pl} \left(T_m - T_B \right) / h_f \tag{7-10}$$

In which T_m is the equilibrium freezing temperature, K and T_B is the splat bottom temperature, K, which can be represented as the following,

$$T_B = \frac{k_l T_l / \sqrt{\alpha_l} + k_{sub} T_{sub} / \sqrt{\alpha_{sub}}}{k_l / \sqrt{\alpha_l} + k_{sub} / \sqrt{\alpha_{sub}}} \tag{7-11}$$

The objective of this chapter is to examine and extend the applicability of these group parameters to enable a universal description of particle state in thermal spray. Both averages and distributions in the data have been analyzed and illustrated through the concept of 1st order process maps. Considerations have been provided for both plasma spray and HVOF processes for ceramics and metallic alloys. It is envisioned that these maps will provide not only insights into the process-particle conditions but enable a fundamental methodology for description of particle states in thermal spray processes.

7.2 Materials and Experimental Methods

The concept of process map envisages a common platform to represent and cross compare data, properties and mechanisms. Even for a single process, for example plasma spraying, there are many hardware configurations available from different manufacturers. In addition, there are different processes such as HVOF, wire arc spray and flame spray that also could beneficially be investigated by the same methodology. Vaidya et al. [151, 168] successfully carried out experiments covering different equipments and processes for Ni-5Al and YSZ.

The following spraying systems have been used in this investigation:

Air plasma spray 7MB torch (Sulzer Metco, Westbury, NY) with an 8 mm 'G' nozzle was used with the non-swirl gas distribution. A mixture of nitrogen (N_2) and hydrogen (H_2) gas was used for plasma generation. The powder injector with inner diameter of 1.8 mm was externally located at a 90° orientation with respect to the anode axis.

An integrated diagnostic sensor set up was utilized for the particle state measurement and is shown in Figure 4-3 in chapter 4[39]. Detailed diagnostic characterization of the spray plume has been carried out using multiple sensors that are set up in a 3D manner. The sensors used are Spray Position Trajectory sensor 'SPT' (In-flight Ltd, Idaho Falls, ID), In-flight particle pyrometer 'IPP' (In-flight Ltd, Idaho Falls, ID), and 'DPV 2000' (Tecnar Automation Ltd, Quebec, Canada). Detailed description of these sensors are available in the literature[123, 151, 169]. A large number of particle measurements were acquired (>10,000) with the DPV 2000 at the 'flux center', which was determined using the 'auto centering' algorithm of DPV 2000. Particle in-flight characteristics (position, temperature, velocity and size) were collected from 'good particles' within a measurement volume of $1.95 \times 0.5 \times 0.5$ mm^3 at the 'flux center' of the spray stream. Spray stream position was measured using SPT sensor and ensemble temperature was measured using IPP. IPP 'looks' at a cylinder (5 mm in diameter and 50mm in depth) in the spray stream from the top. Due to the large depth of focus ($\pm$25mm), the spray stream was within the measurement volume at all times. This integrated diagnostic sensor set-up provides redundancy, complementary data acquisition and the opportunity to cross correlate data from different instruments. Data from the SPT and IPP ensemble sensors are not presented in this chapter. However, it is essential to mention that the quick feed back from these sensors helps to assess data fidelity[58].

Previous studies have revealed that the plume position of the particles at injection is critical in determining the heat and momentum transfer for external injection DC plasma spray processes. As one scans through the radial plume position at the point of injection (through stepwise changes in carrier gas flow rate), there is a maxima observed in temperature and velocity of the particles at a fixed plume position for a given torch/nozzle combination. The existence of this "sweet spot" is discussed in detail

elsewhere[58]. With such an injection strategy, one can achieve the optimum particle state for a given material under a set of parametric conditions. It is pointed out that such an injection optimization step was carried out for most of the materials/process conditions described in this chapter particularly those comparing different materials. An added benefit of this strategy is better data fidelity from diagnostics as the particle position in the plume is more appropriately captured.

7.3 Results and Discussion

7.3.1 Development of 1st Order Process Maps Across A Spectrum of Materials for A Single Process

Process maps are science based representations of interrelationships among control parameters and measured responses. Such maps provide integrated set of relationships that link processing to properties and ultimately to performance. The map can consist of both experimental and computational data and illustrated to identify key response attributes. Process maps are useful not only because they allow visualization of the process variables but also enable intelligent control of the process. For example, in a production environment, a well developed process map can enhance stability and reliability. Process maps also allow one to validate theoretical models and enable model guided design of experiments. The knowledge obtained in the development of process maps can be both fundamental and practical in nature.

Several past studies have defined and synthesized process maps for thermal spray. Given the multi-dimensional nature of the thermal spray process, process maps are developed based on torch parameter-particle state relations (referred to as a 1st order map) and particle state – coating property responses (referred to as a 2nd order process map). Details on the synthesis and application of these maps are provided in references[151, 164]. These earlier focused studies have been limited to a single material and/or process and provide a framework for coating design, process parameterization and property assessment for such a system. The focus of the present investigation is to explore 1st order maps with multiple materials and processes. Figure 7-1 presents a generalized 1st order map based on large number of process diagnostic results obtained from multiple materials, and processed through a typical air plasma spray torch at one or more process conditions (as mentioned earlier injection was optimized for each material so as to have maximum heat and momentum transfer for that particular condition). A variety of materials with widely different physical properties have been investigated including metals, ceramics and cermets. Figure 7-1(a) is a traditional 1st order temperature-velocity representation based on the DPV generated single particle data. At first glance it is clear that simply using T and V data does not provide an adequate representation of the material behavior within the plasma spray especially to capture the effective energy/temperature gradient within a particle. Aluminum falls on

the bottom of the plot while Molybdenum and Tungsten are on top due to their higher surface temperatures. Furthermore it is inappropriate to compare particle molten status (thermal energy) based only on the surface temperature. For metal particles, the temperature is generally expected to be uniform throughout the particle due to its high thermal conductivity. Thus, the particle surface temperature can be used (to a first approximation) to identify the phase status of the particle [noted that oxidation is an important issue which is considered later in this study]. For a ceramic particle, especially those with low thermal conductivity, the particle temperature can potentially differ from a high value at its surface to the center core. A high particle surface temperature above the melting point therefore does not guarantee the particle is fully melted. The melting percentage of the particle depends on its size, thermal conductivity, latent heat, and residence time in the plasma flame. Furthermore, particle velocity cannot provide sufficient information for particle kinetic status at impact considering different physical properties of materials and particle size at impact.

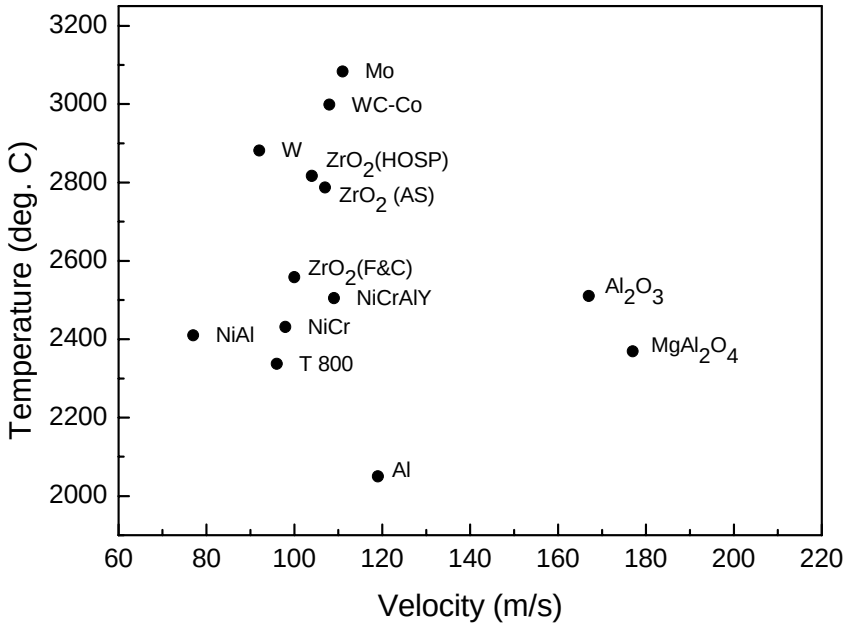

(a)

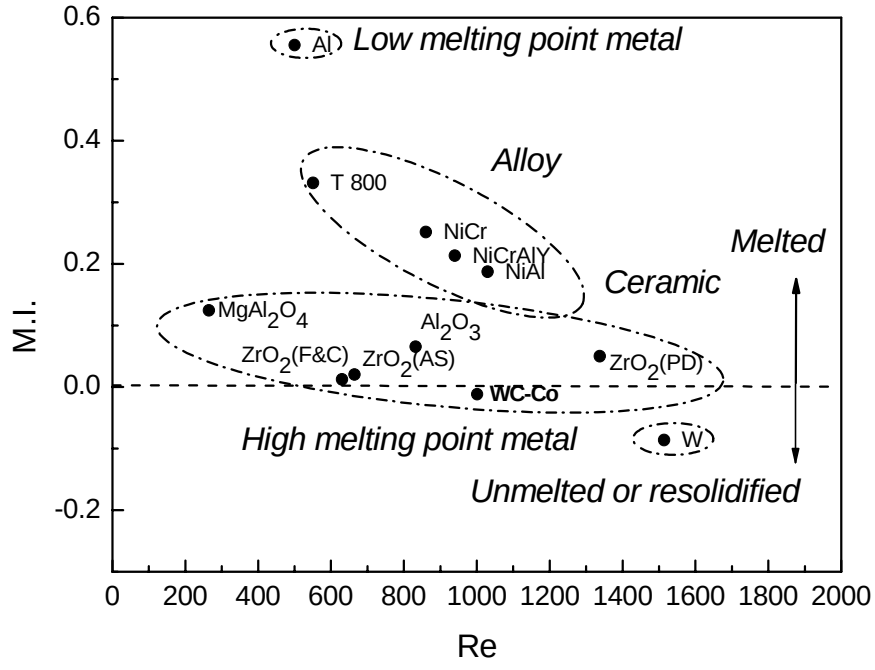

(b)

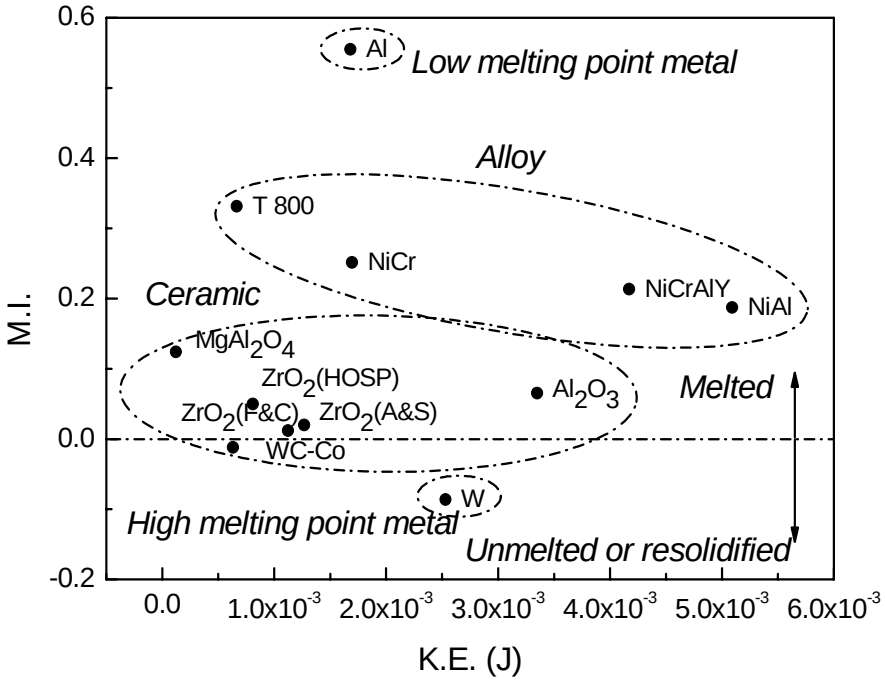

(c)

Figure 7-1 (a) T-V global process map, (b) M.I.-Re global process map and (c) M.I.-K.E. global process map

As discussed earlier, group parameters, Melting Index and Reynolds number, provide a novel strategy for a more comprehensive description of particle states. The DPV generated single particle data was used to calculate the individual particle's M.I.

and Re numbers, and average values based on these measurements for each of the materials. This is represented in Figure 7-1(b) from the T, V and diameter data obtained for materials in Figure 7-1(a). Several important observations can be made.

In the M.I.-RE based 1st order process map, it is clearly seen that low melting point Al shows the highest melting state (value of M.I.) while W shows the lowest value of M.I. despite representing a much higher temperature in the T-V based 1st order process map.

Since M.I. is a non-dimensional group parameter, it is now possible to demarcate a singular melting point (at M.I.=0) for all the materials in a single map, i.e. the boundary between molten and un-molten or re-solidified materials. As such the 1st order process map can now be used to represent materials that are nominally molten and superheated versus those that are at the cusp of melting.

Most metallic alloys have better molten status compared to oxide ceramics, due to their higher thermal conductivity and lower melting points. By considering these two non-dimensional group parameters, M.I. and Re, the global M.I.-Re process map successfully represents molten and kinetic status for multiple materials in a single map and as such provides a universal representation methodology for 1st order process maps based on DPV 2000 single particle data.

Similar to the development of M.I.-Re process map, M.I.-K.E. process map can be developed based on the single particle data as shown in Figure 7-1(c). The cubic component of particle size and square component of particle velocity in K.E. equation provide a better way to describe the particle energy state. For example, the K.E. value for the HOSP ZrO_2 shown in Figure 7-1(c) is much smaller than those of F&C and A&S particles, which is opposite to the trend of kinetic status shown in Figure 7-1(a) and (b). Considering the fact that the density of the HOSP particles is much smaller than those dense ones, different trends for kinetic status shown by velocity, Re and K.E. are expected. Thus, this M.I.-K.E. process map realizes the consideration of process from the stand point of actual kinetic energy. It also carries most information revealed by a M.I.-Re map. The disadvantages of the MI-KE maps are, first, it is not non-dimensional, and second, the material viscosity which is important for determining the extent of spreading, flattening and splat-splat contact is not included in the K.E. description.

7.3.2 Expanded Process Maps: Comparison Across Processes and Materials

A large group of process and materials have been examined by Sampath and Vaidya et al. [86, 151, 164]. Figure 7-2(a) shows an overview of the 'atlas' presenting the process window for multiple processes and materials in a T-V map. This kind of an 'atlas' would be useful to understand process limitations. Within each process, considerable details can be nested in terms of the effects of various control factors that go into the process. Such a map can provide a method to compare operational zones, limits and variabilities for these spraying systems. For identical materials which can be used in

different systems, this process map can provide the range of particle characteristics over which it can vary.

Figure 7-2(b) provides the process window for multiple processes and materials in a M.I.-Re space. This provides a more fundamental approach to represent particle status using dimensionless scales, which realizes the comparison among multiple materials. The most significant difference in conditions is depicted for the Ni-5Al material for which the data are spread over a very large range in M.I.-Re space for different spraying systems. This difference is not clear in the T-V space due to the fact that the particle size difference in the TWA and APS processes is not visible. As shown in Figure 7-2(b), the lower M.I. and larger Re for the TWA process result from larger particles. The M.I.-Re process map therefore provides an improved basis for understanding the in-flight particle status.

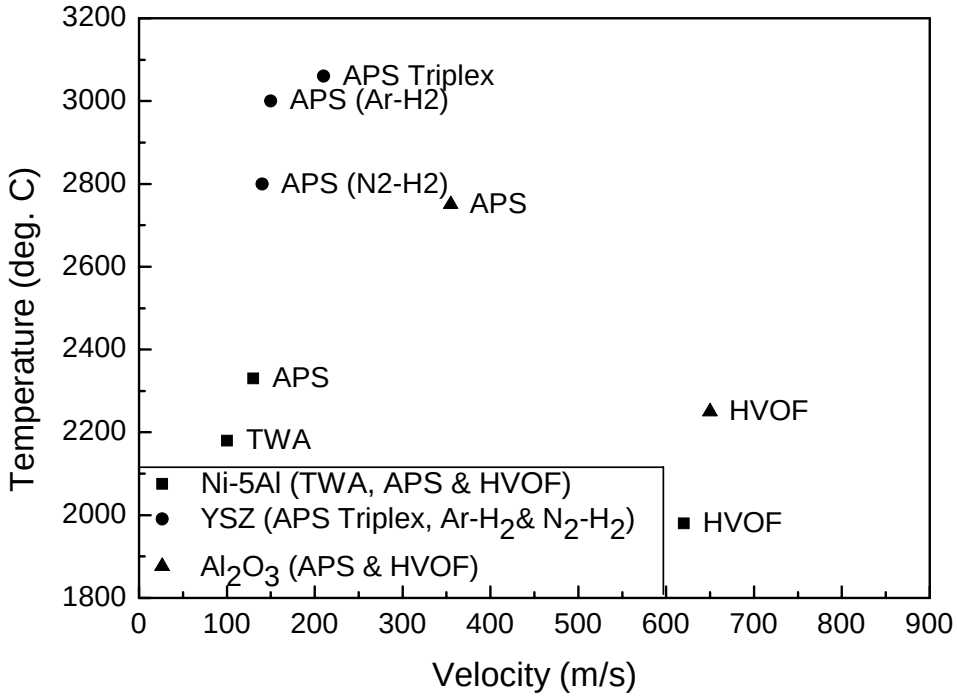

(a)

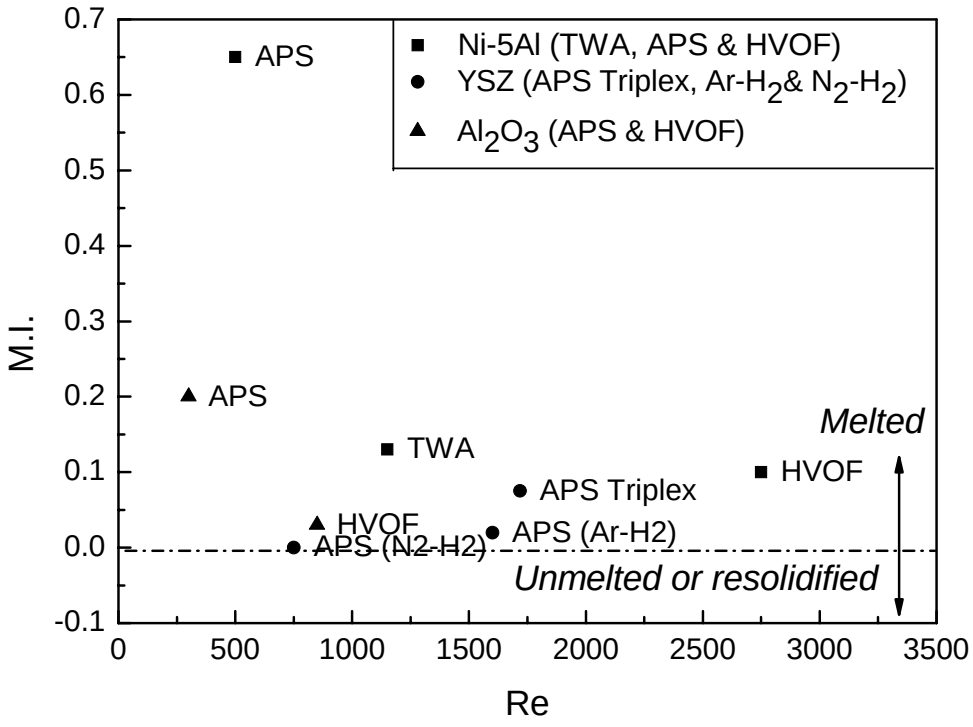

(b)

Figure 7-2 Global process map for multiple process and materials (a) T-V map and (b) M.I.-Re map

7.3.3 Implications of Group Parameters on Materials and Process Assessment: Particle Size Effect in YSZ

Benefits of selecting group parameters are evident for single material with different process or feedstock combinations. Figure 7-3 shows a first order process map for plasma spraying of two types of YSZ powders using two types of nozzles. Both powders were of the plasma dandified variety comprising to two size distributions: a fine and a coarse size cuts. Each of the powders was subjected to a variety of plasma spray process conditions using a 6 mm and an 8 mm nozzle diameter. As expected, Figure 7-3(a) shows that the 8 mm nozzle produces slower and hotter particles compared to faster and cooler ones. The ellipses represent envelope of T-V response for a given feedstock-nozzle combination for a variety of spray parameters (torch current, hydrogen and primary flow rate). A 1st order T-V map at first glance suggests that the coarser powder is at higher particle temperatures. This can be attributed to the fact that the reported DPV measurements are primarily from a particle surface and fail to represent the volume thermal energy of the particle.

Replotting the same 1st order data through a M.I.-Re map in Figure 7-3(b) clarifies these issues and yields expected results. The M.I. for coarser powder is somewhat lower than the finer powder while the Re is higher for the coarser powder due to the larger

particle diameter. Figure 7-3 demonstrates the utility of group parameters in accurately capturing the process-material responses in the 1st order maps.

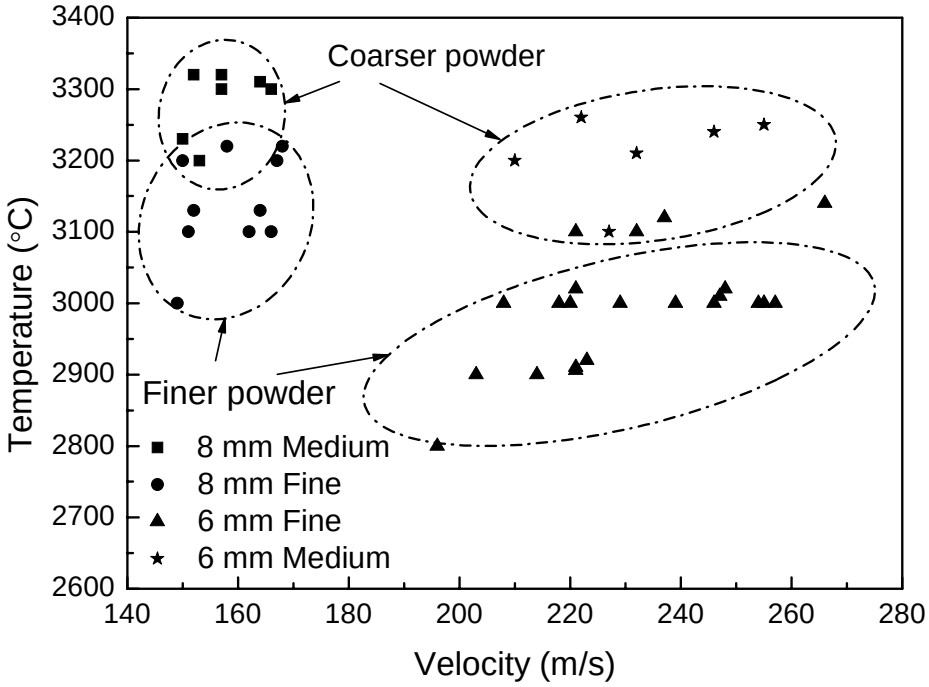

(a)

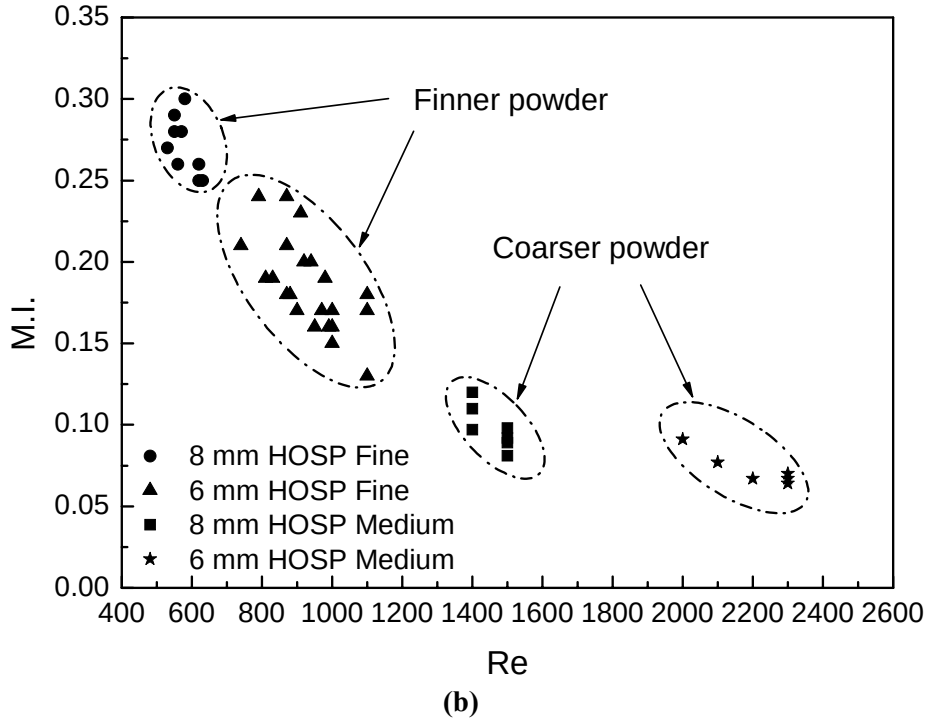

(b)

Figure 7-3 Nozzle and particle size effect on process window for YSZ (a) T-V map, (b) M.I.-Re map

7.3.4 Discussion on Distribution

1st order process maps has been reported so far based on average values of DPV measured single particle data. For the case of M.I., calculations were made at the single particle level and then averaged. Average values of the particle conditions, however, are insufficient to completely describe the process. Earlier work has shown that considerations of temperature distributions are important as they enable identification of the melting state of the materials particularly for refractory oxides [53].

Another straight forward way to visualize the particle state is to display the entire DPV measured distribution in the 1st order map. Figure 7-4(a) examines such a T-V space for several of the materials identified in Figure 7-1 encompassing entire DPV output of several thousand spray particles. Each ellipse represents the distribution for each group of particles (same material) in the T-V space (the data is truncated to eliminate the outliers which represents < 5% of the total data set). Again simply comparing the temperature-velocity distributions doesn't adequately capture the observed effects. Figure 7-4(b) is the corresponding comparison of the M.I.-RE 1st order maps. Superimposing the isomelting line representing the zero value of M.I., one can easily discern the effective molten status for the whole group of particles. This is uniquely made possible through our non-dimensional mapping strategy. Figure 7-4(b) captures the material response as well as the melting state and as such provides a more significant method of process visualization.

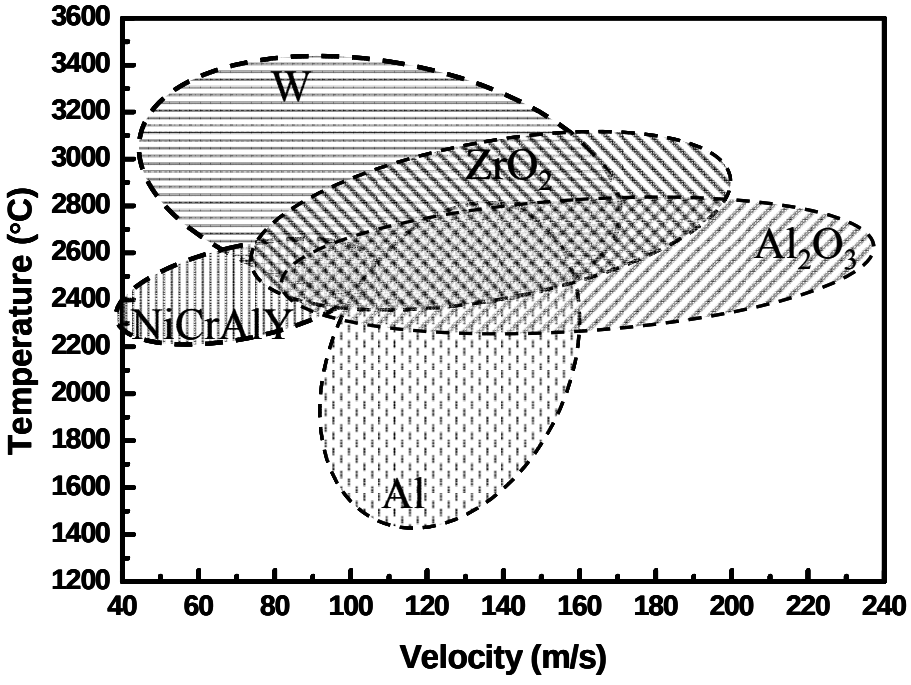

(a)

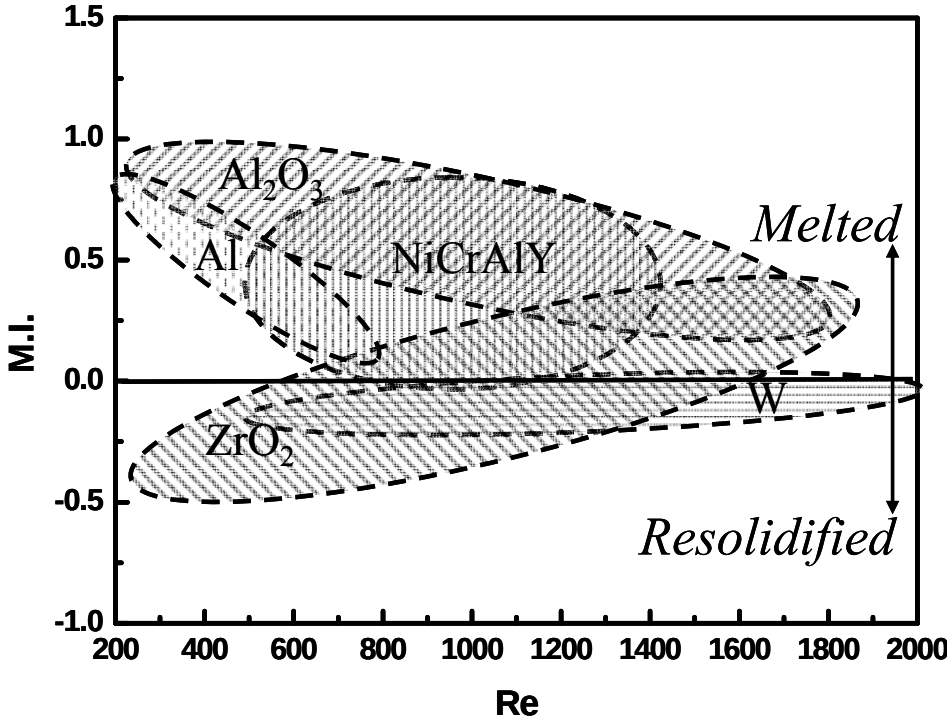

(b)

Figure 7-4 (a) global process map considering temperature and velocity distribution; (b) global process map considering M.I. and Re distribution

M.I. represents the molten status of each single particle and allows for comparison of molten status among multiple materials subjected to similar plasma spray conditions. A quantitative extension to Figure 7-4(b) is to calculate the number density of the particles above and below the melting threshold represented by the M.I.=0 isotherm for a given material/process condition. This enables calculation of the number density of molten particles. The results presented in Figure 7-5 indicate that 32% of the YSZ particles are molten from this specific measured parametric set. Also, based on the value of M.I. of the single particles, one can further compare molten status directly_among various materials and processes. As shown in Figure 7-6, the updated global process maps (from Figure 7-1) consider distributions in M.I. as per the above paragraph. Comparisons of molten status through different groups of particles for multiple materials are realized. For example, when comparing the M.I. distribution of ceramics with those of Al and NiCrAlY, it is revealed that most particles from the group of metals and alloys melt much more easily than the two ceramics, even though the whole group of the Al_2O_3 particles has started melting. This allows for a more elaborate comparison of molten status among multiple materials, which can not be obtained from the information of particle temperature alone. It is also shown in Figure 7-6 that, even though NiCrAlY has much higher average M.I. value (0.33) than that of Al_2O_3 (0.046),

the molten content for NiCrAlY (98%) is smaller than that for Al_2O_3 (100%), which means the whole group of Al_2O_3 and 98% of NiCrAlY have been melted to some extent. For ZrO_2, the Mean M.I. is 0.012, which is similar to that of Al_2O_3. However, it is clearly shown that only 32% of the ZrO_2 particles have been melted as shown by the statistical distribution for Melting Index. Checking the distribution provides detailed information for the molten status for a whole group of particles, which cannot be obtained from average of M.I. for the whole group of particles.

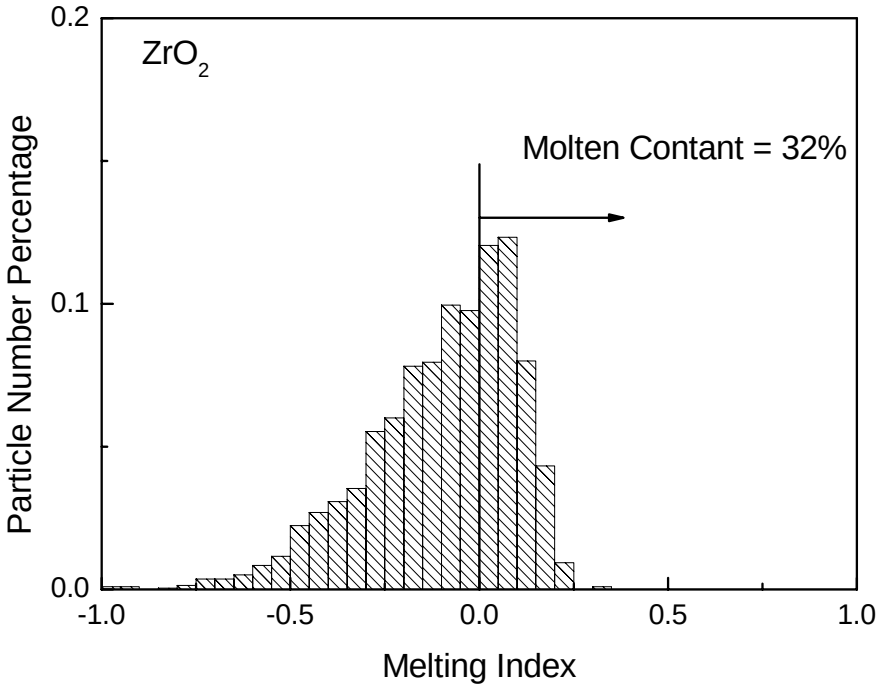

Figure 7-5 Molten Content: Number percentage of molten particles

Figure 7-7 shows the M.I.-Re distribution maps for YSZ subjected to a variety of processing conditions. The ellipses represent the M.I. and Re distribution for the whole group of particles under each extreme condition. The average values are also noted within the distribution ellipses.

The DPV sensor can provide information for each single particle, which can be used for each corresponding splat flatten ratio calculated by Eqs. (7-9)-(7-11). The splat thickness distributions under different spraying conditions are shown in Figure 7-7(b), from which the 'thickness per pass' for each operating conditions can be successfully predicted. Also, the important parameters relating to coating quality such as deposition efficiency has also been listed in this figure. It is clearly shown that with increasing M.I. and Re, the 'thickness per pass' keeps decreasing corresponding to increasing flattening ratios while the relative deposition efficiency keeps increasing. Increased thermal and kinetic energy will favor the flattening and spreading of droplets

which will favor the formation of dense coatings corresponding to increasing thermal conductivity as shown in Figure 7-7 (b).

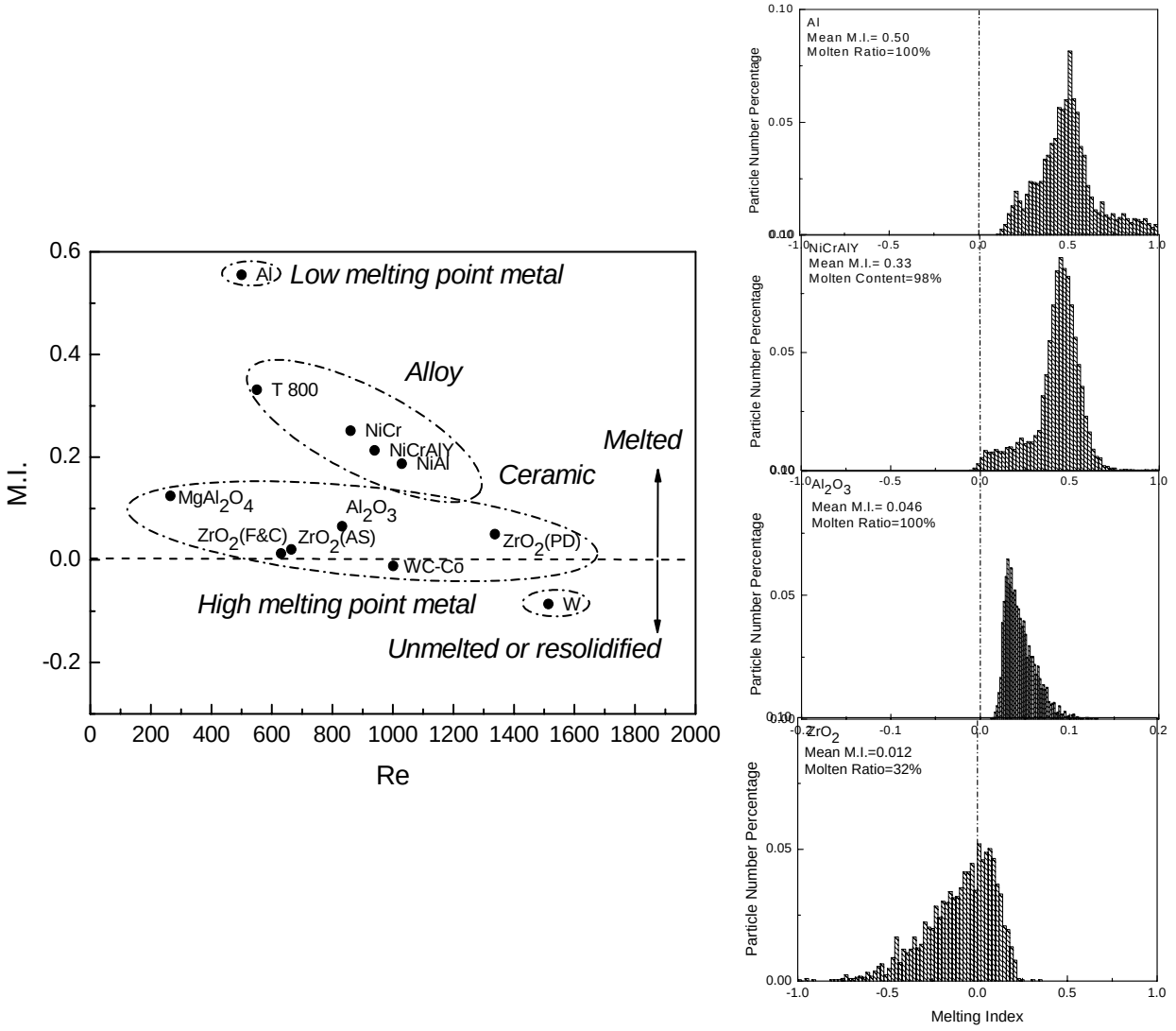

Figure 7-6 Statistical representation of global process map

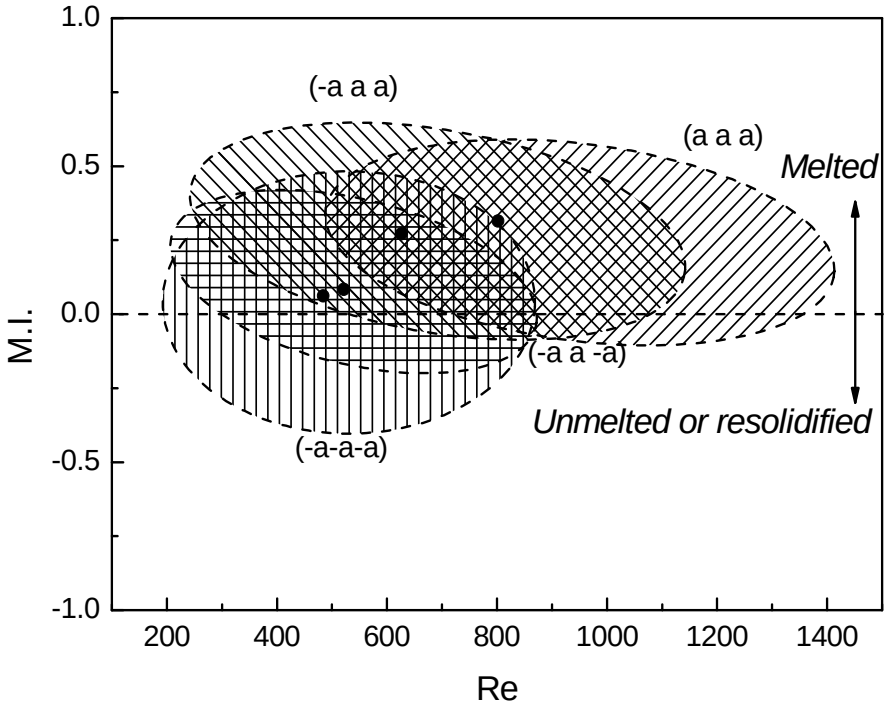

(a)

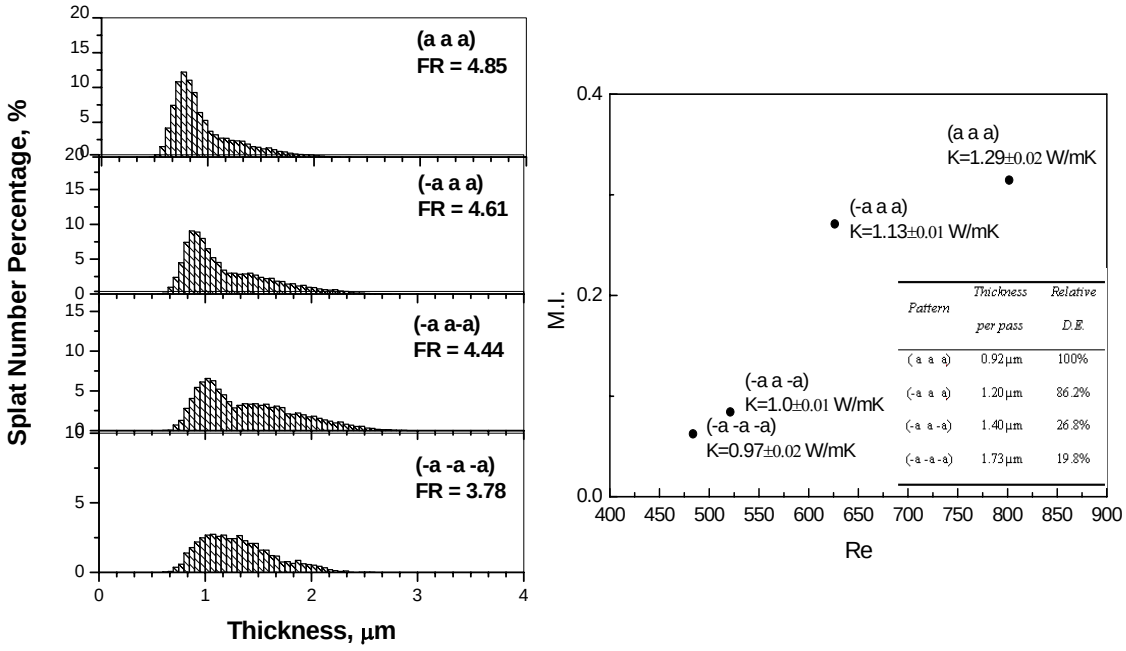

(b)

Figure 7-7 (a) YSZ process map considering M.I. and Re distribution and (b) Correlation of average *M.I.*, *Re* and predicted splat thickness distribution

1st order process maps can also be used to compare across processes. Figure 7-8 compares plasma and HVOF process maps for alumina. Since only a single material is compared, the isomelting line can be identified in this T-V map. It is clear that the APS Al_2O_3 has much higher molten status than its HVOF counterpart, while the HVOF particles have much higher kinetic energy. The M.I.-RE map also shows a similar trend although the differences in Re is not as substantial. This relates to the significantly smaller particle size distribution of the HVOF powder feedstock. Both high thermal and high kinetic energy favor the spreading and flattening of droplet impacting on substrate, which explains similar Flattening Ratio values for Al_2O_3 in different spraying systems.

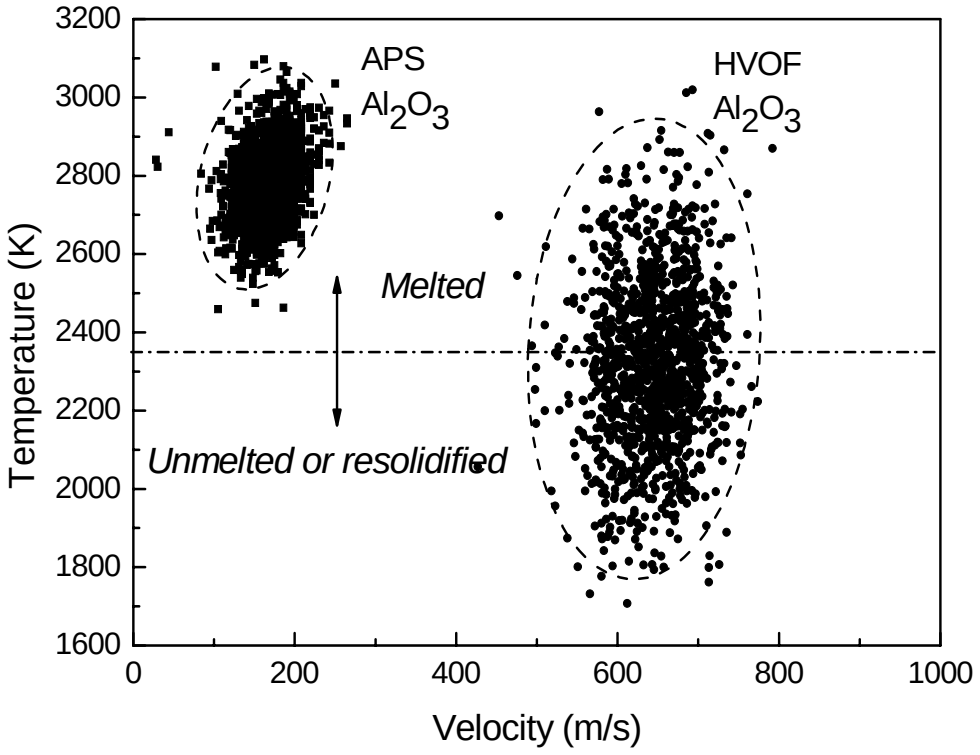

(a)

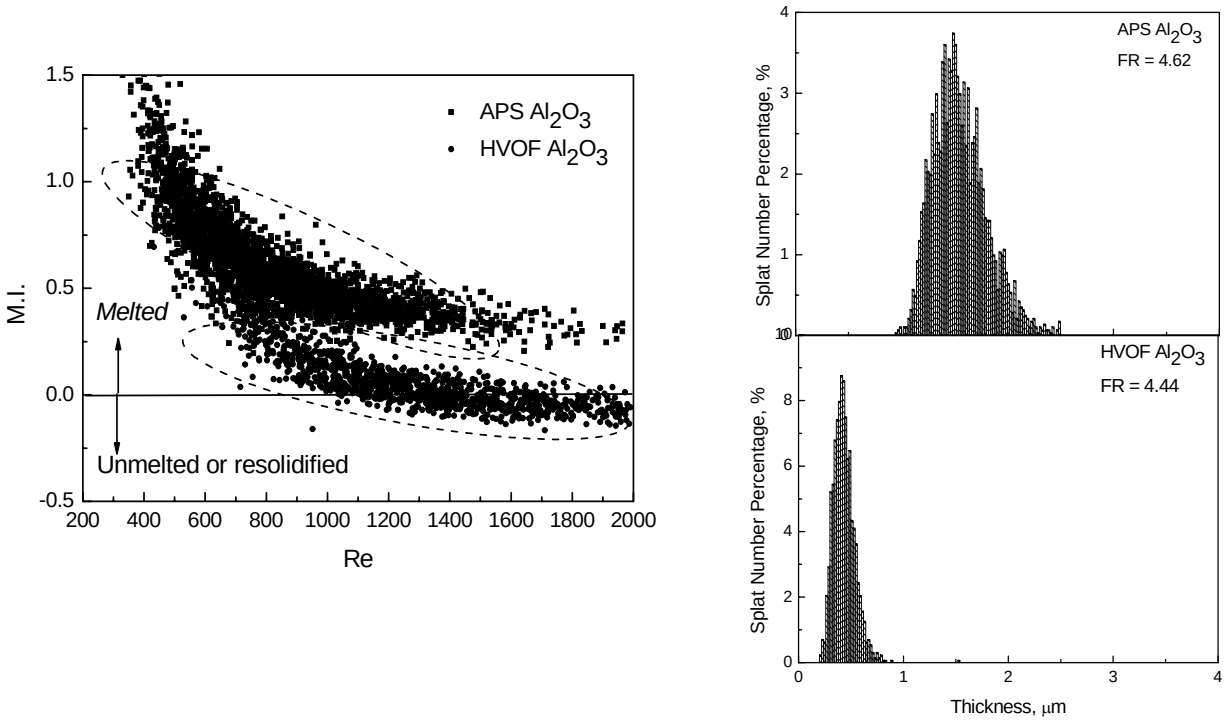

(b)

Figure 7-8 Al_2O_3 process map considering different processes and (a) temperature, velocity distribution;(b) M.I., Re distribution

7.3.5 Discussion on Particle Oxidation Status

An important consideration during thermal spraying of metallic particles is in-flight oxidation. In-flight oxidation can introduce both physical changes to the metallic particles (such as extended heating due to exothermic reaction) and chemical changes in terms of the material. The former change needs to be considered in the interpretation of the process-particle state data and will be manifested in some form in the first order process map, while the latter one can affect the emissivity of the particle and can introduce uncertainties in temperature measurements.

7.3.5.1 Implication of Oxidation on Particle Temperature

To understand the contribution of the exothermic oxidation on particle temperature, a comprehensive process model, LAVA-3D P, was utilized. Description of the model has been presented in Chapter3. Meanwhile there are extensive peer reviewed literatures on the subject [73, 78]. Suffice to note that this model allows us to track individual particles during traditional DC plasma spraying in-flight and enables incorporation of physical mechanisms into the model. Figure 7-9 compares the particle

temperature data for Mo particles with and without oxidation contribution. It is clear that under typical thermal spray conditions the particles undergo substantial increase in temperature due to exothermic oxidation.

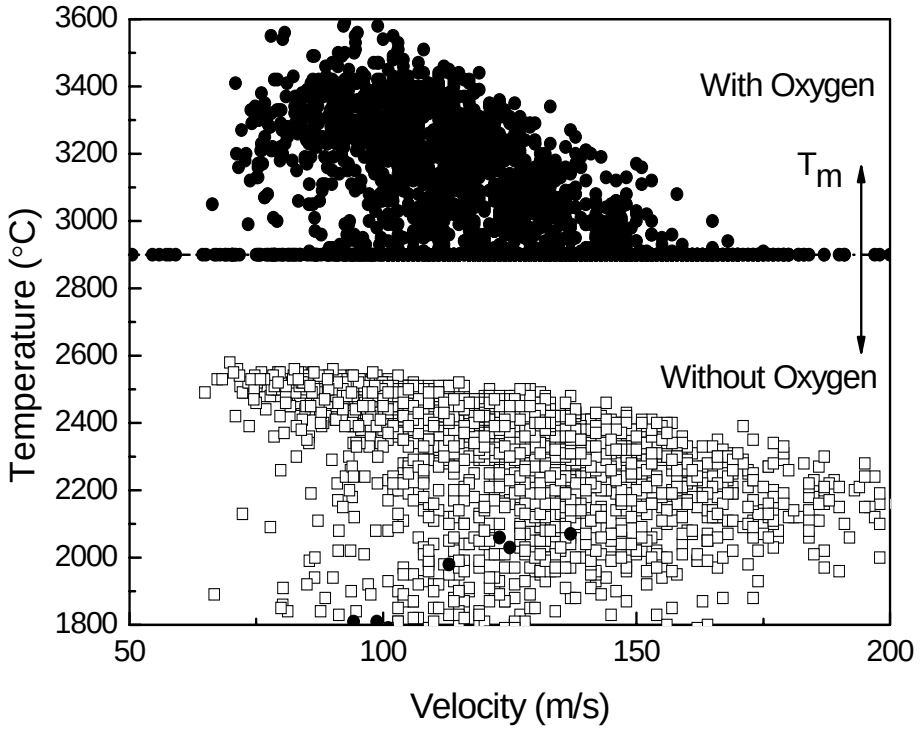

Figure 7-9 Oxygen effect on particle in-flight status from simulation

7.3.5.2 Discussion on Oxidation Index (O.I.)

As it is the goal of this chapter to develop mapping strategies for particle diagnostic results, additional methods of data representation for metals and metal laden composite particles during atmospheric thermal spraying are explored here. As discussed earlier oxidation index is a means to capture these effects and trends. With the help of single particle sensor, the relative oxide content can be calculated and compared through the same materials. Figure 7-10(a) and (b) show the O.I.-M.I. and O.I.-Re process maps for Molybdenum particles, respectively. As shown in Figure 7-10(a), for the same particle size distribution, larger sized nozzle will generate slower plasma jet providing enough dwell time for the in-flight particles to be heated up and to have more chance to react with oxygen in the environment, which corresponds to high O.I. and M.I. values. On the other hand, the generation of enthalpy for the oxide provides considerable amount of thermal energy to enhance the particle melting. For the same nozzle size, smaller

sized particles has less total heat capacity and high specific area, which favors the heat and mass transfer between the particles and their environment, and results higher values of M.I. and O.I.

Figure 7-10(b) reveals the correlation between the oxidation status and the kinetic energy. For the same initial particle size distribution, decreasing nozzle size dramatically increases the plasma jet velocity as well as the in-flight particle velocity. This reduces the particle dwell time and thus the oxidation content. For the same nozzle size, smaller sized particles have much larger specific area for oxidation reaction, which results higher oxidation content.

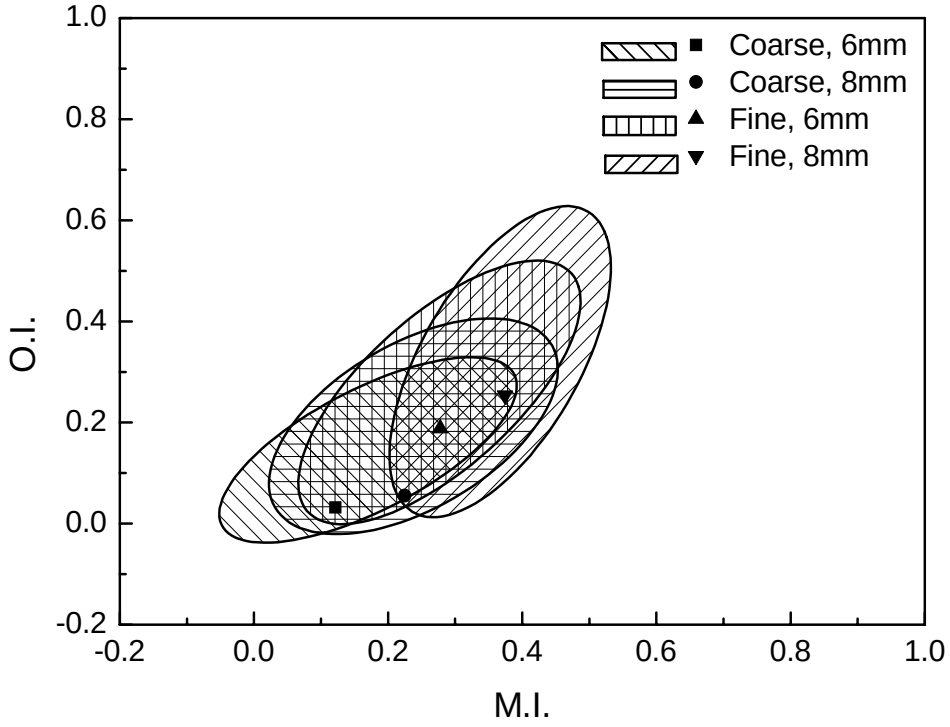

(a)

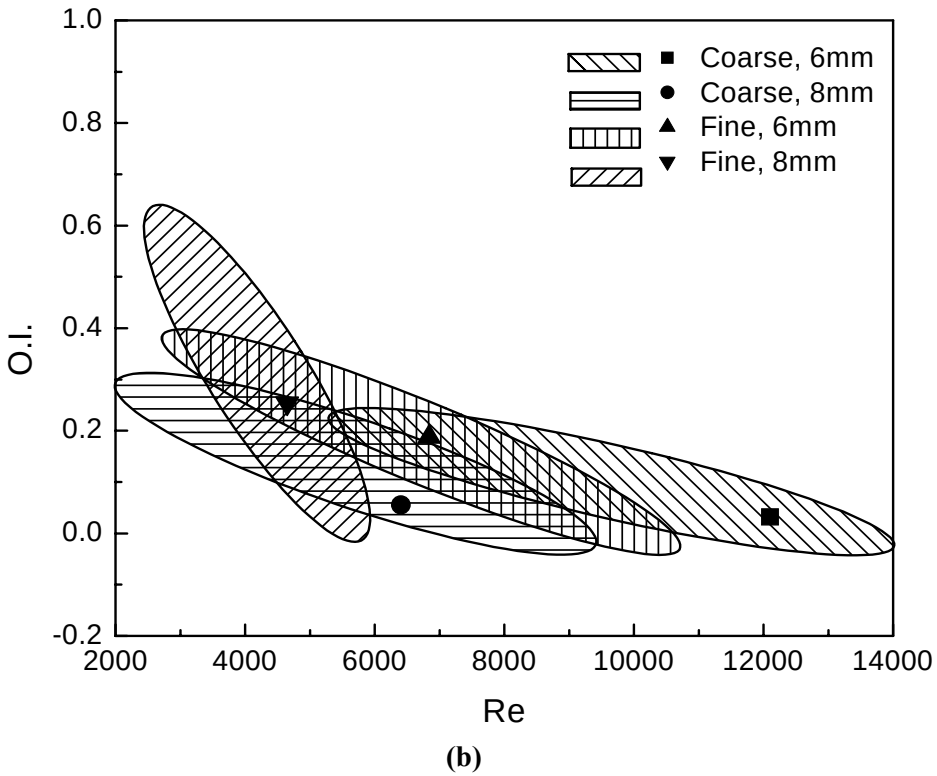

(b)

Figure 7-10 (a) O.I.-M.I. and (b) O.I.-Re map for Molybdenum particles under different combination of nozzle and particle sizes combinations

7.3.6 1st Order Maps Based on Ensemble Particle Diagnostics

The calculation of non-dimensional M.I.-Re maps are enabled in large part due to the availability of single particle type diagnostic sensors such as DPV 2000. In many industrial settings, single particle diagnostics are either not available or not used due to the instrument complexity. Ensemble sensors such an Accurapray, IPP or SprayWatch are more widely used. This limits the ability to calculate group parameters. Under these circumstances, a simple modification to the T-V diagram is to represent the temperature data qualified to the melting point (i.e. T-Tm). Figure 7-11 displays these results for a number of APS and HVOF sprayed metals, ceramics and cermets. The difference between particle surface temperature and the melting point for that corresponding material has been used to represent the particle molten status. The super-imposed dashed line represents the position at which particle surface temperature equals to its melting point. Figure 7-11 also compares statistical distribution for Al_2O_3 molten status from different spraying systems. Comparing with HVOF process, APS Al_2O_3 particles obtain much higher thermal energy and thus molten status with 100% molten ratio. Again this figure quantifies the fact that the APS process provides higher thermal

energy compared with the HVOF process, while lower kinetic energy than its counter part.

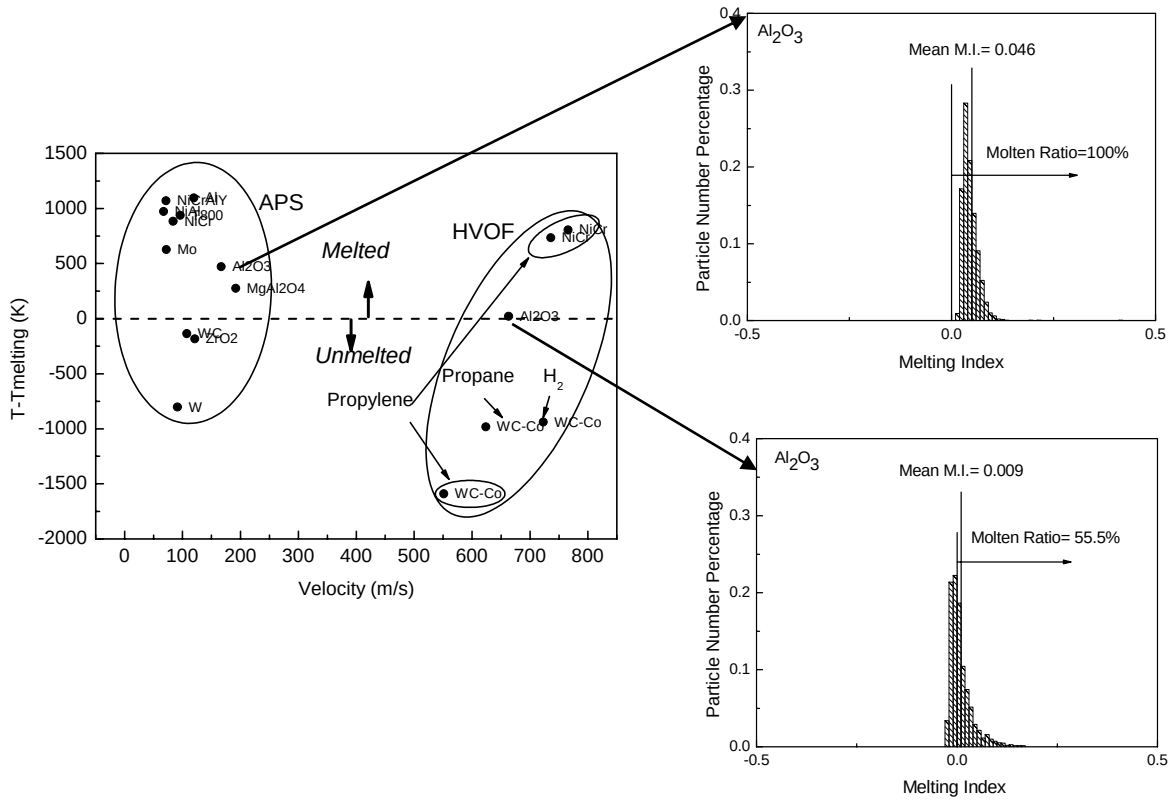

Figure 7-11 Global process map considering different processes

7.4 Conclusions

This chapter describes a new strategy for visualization and representation of particle diagnostic results for thermal spray processes. The definition and physical interpretation of non-dimensional group parameters, Melting Index and Reynolds number, are described and the advantages of using these parameters to represent particle in-flight status are discussed. Another group parameter, oxidation index, has been defined and used to represent a measurement of in-flight oxidation of metallic particles for various parametric conditions. The outcome of such a strategy is a universal method for representation of in-flight particle characteristics in thermal spray processes. This results in a global 1st order process map, comparing across a spectrum of materials for air plasma spray process. This new approach offers significant advantages over traditional T-V based 1st order maps. These maps also allow for representation of

molten and kinetic status of multiple materials and can be successfully represented in a unified map.

By expanding the maps to include entire distributions of the M.I.-Re space, a more comprehensive comparison of molten status among multiple materials can be realized enabling critical cross-comparison of process-material interactions amongst different spraying systems and different materials. O.I.-M.I. and O.I.-Re process maps are used to further reveal particle in-flight status for a certain material under various process conditions. Finally, approximations to the new mapping strategies are proposed in circumstances where only ensemble particle diagnostics are available.

Chapter 8 Synthesis

To obtain reliable and predictable coating microstructure and properties during plasma spray, spray process needs to be controlled and coatings need to be tailored. In order to achieve that, the complexities of the process in terms of the various sub-processes (particle injection, development of in-flight particle characteristics, splat formation, and coating build-up) and interrelated variables need to be broken down, understood and re-integrated into perspective to enable complete understanding. The critical issues influencing coating build-up and property development (in-flight state of the process, deposition conditions and substrate conditions) need to be identified, understood, and controlled.

This dissertation focuses on the integration of process diagnostic and three-dimensional simulation in thermal spraying. Effects of injection angle and carrier gas flow rate on in-flight particle characteristics are studied experimentally and interpreted through numerical simulation. Plasma jet perturbation by particle injection angle, carrier gas, and particle loading are also identified. Maximum particle average temperature and velocity at any given spray distance has been systematically quantified. Optimum plasma plume position for particle injection observed in experiments was verified numerically along with description of physical mechanisms. Correlation of spray distance with in-flight particle behavior for various kinds of materials has been revealed. A new universal method for visualization and representation of particle diagnostic results has been presented. Several interesting observations have been pointed out during this study, which will be discussed in this chapter to enable integrated understanding of the individual studies.

8.1 Discussion on Salient Results

8.1.1 Radial Injection of Particles into DC Plasma Jet

In Chapter 5, an intriguing phenomenon was presented – injection 'sweet-spot'. It has been observed to be invariant with respect to a host of process variables that significantly influence particle injection. It is clear that such an optimum will occur with the maximum heat and momentum transfer between the particle and the plasma plume in the close vicinity. Since most of the critical plasma-particle interactions occur in the hot zone where experimental measurements are limited, numerical simulation has been carried out to examine the phenomenon.

As shown in Figure 8-1, there are primarily two zones in the plasma jet that the in-flight particles will experience during flight, i.e. the hot plasma zone where the particles receive most of the thermal and kinetic energy and the hot gas zone where melting continues and both thermal and kinetic energy of the particles keep decreasing which could result in particle re-solidification. Particles following trajectory marked by '1' in

Figure 8-1 is a case of under injection in which improper penetration results in smaller dwell times of particles in both the plasma zone and the hot gas zone. The opposite extreme is over injection marked by '3' in Figure 8-1, where most of the particles are over injected resulting in their quick penetration through the plasma zone and less dwell time in the hot gas zone.

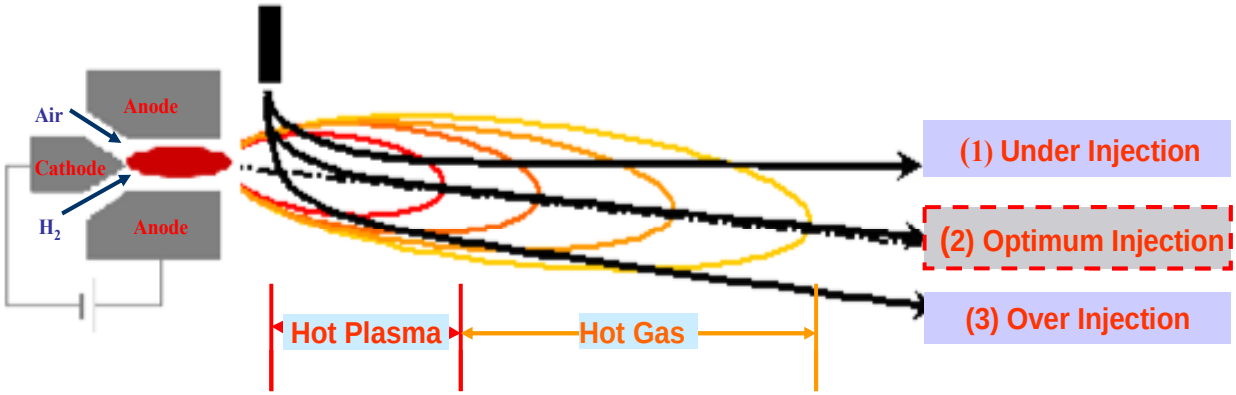

Figure 8-1 Schematic of plasma plume and particle injection

An optimum carrier gas jet speed therefore should be used to inject the particles into the hot plasma jet center, which is marked by trajectory 2 in Figure 8-1. Once the particles reach the center, their vertical momentum should have been mostly consumed and the relative vertical velocity between the plasma jet and the injection particle should to be very small. It is believed that with such an optimized injection speed, the particles can gain maximized heating and speeding. It has been proved experimentally and numerically that in the current experiment set up the optimized plasma plume trajectory is about 5 degree (see Figure 8-2).

If the flow rate of primary and secondary gas flow rate is changed, i.e. the plasma jet speed changed, it is obvious that the carrier gas flow rate should be adjusted accordingly so as to achieve optimized injection. In order to explain the plume angle is always 5 degree when optimized injection is achieved, the concept of 'Sweet Spot' is introduced here. The 'Sweet Spot', as shown in Figure 8-2, is defined as a small area in the center of the plasma jet. It is believed that, whatever the flow rate of primary and secondary gas flow rate is, a proper carrier gas flow rate should be used to inject the particles into the 'Sweet Spot'. The flow rate of the carrier gas should be controlled in a way such that, on one hand, it should provide enough vertical momentum for the particles to enter the 'Sweet Spot'. On the other hand, the vertical momentum that the particles gained from carrier gas flow rate should be consumed mostly by the time they reach the 'Sweet Spot', so that the particles will follow the trajectory of the plasma plume thereafter. Otherwise the particles will quickly penetrate through the plasma jet

vertically since they still have plenty of vertical momentum after they reach the 'Sweet Spot'.

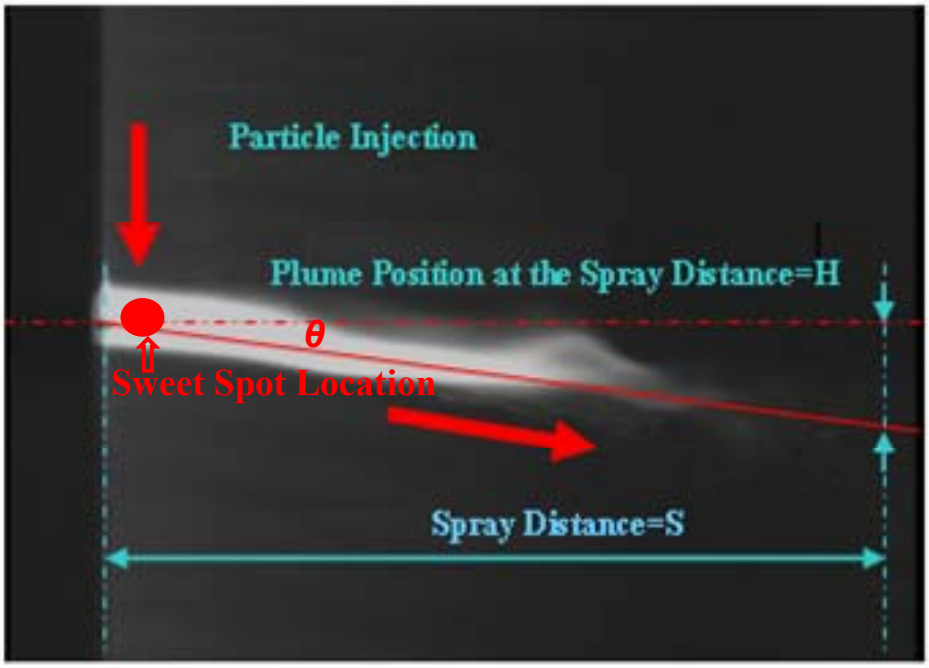

Figure 8-2 Schematic of the so called 'Sweet Spot Location'

It is believed that the 'Sweet Spot' location is almost fixed regardless of the primary, secondary and carrier gas flow rates. Accordingly, the velocity ratio of the carrier gas to the plasma jet should be maintained the same when optimized injection is achieved as shown in Figure 8-3. At the same velocity ratio of plasma jet and the carrier gas jet, the plasma plume trajectory after impinging should be the same. This explains the unchanged 5 degree plume angle when optimized injection is achieved.

It can be seen in Figure 8-3 that the plume angle and the velocity ratio at the optimum (maximum temperature and velocity) are comparable across the different primary gas flows. This suggests that the velocity ratio governs both the angle of the spray stream and the momentum transfer to the particles and that there exists a velocity ratio where momentum transfer reaches maximum. This agrees well with the observation in Chapter 4 that, for each injection angle, the optimum plume position corresponding to the highest temperature and velocity can be obtained by changing injection velocity (carrier gas flow rate). In this case, the vertical contribution of injection velocity should be used when considering velocity ratio.

This integration of experiment and numerical simulation enabled the understanding of the plasma-particle interaction during particle injection and the existence of the 'Sweet Spot' as well as the resultant in-flight particle state as a function of the velocity ratio.

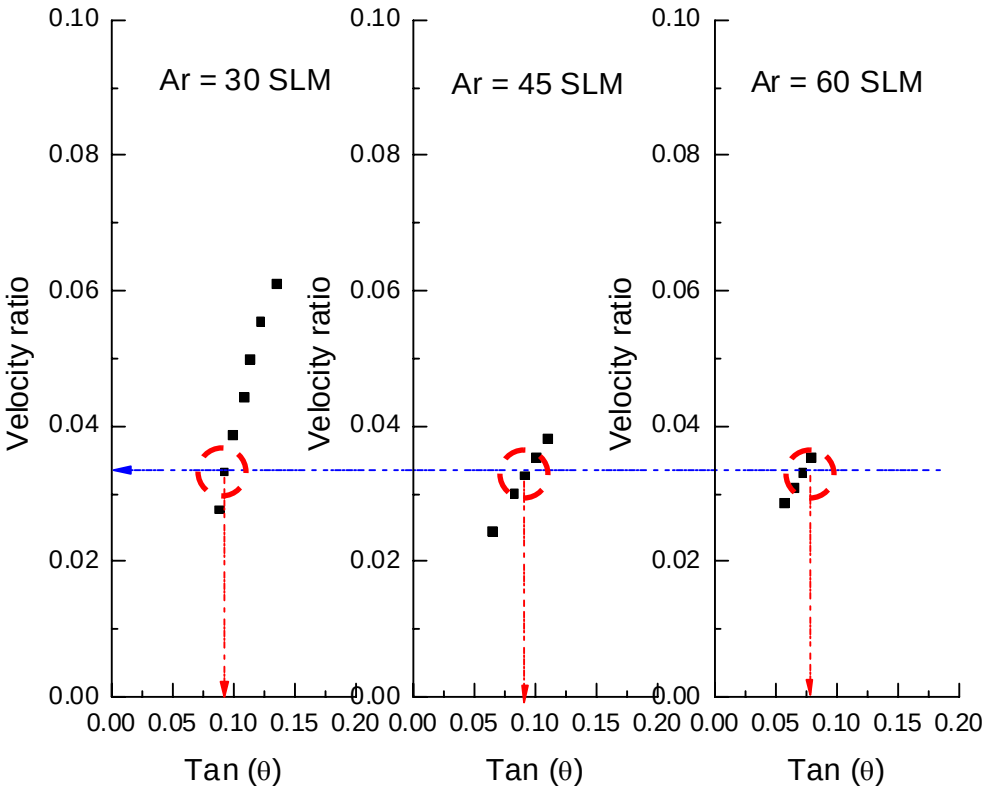

Figure 8-3 Tan of plume angle and ratio of initial vertical velocity to the horizontal velocity at the spray distance for different primary gas flows. The red circles correspond to the optimum injection. Blue horizontal line intersecting the velocity ratio axis shows that optimum injection occurs at the same value of velocity ratio. The red vertical line intersecting the tan (θ) axis shows that the optimum occurs at the same plume angle

8.1.2 Correlation of Spray Distance with In-flight Particle Behavior for Different Kinds of Materials

The particle trajectory in the plasma jet carries information of particle heating and acceleration history, which determines the particle molten status and kinetic energy at impact. Figure 8-4 shows the trajectories of different sized YSZ particles in temperature and velocity fields of plasma plume. It is evident that, at each spray distance, larger sized particles have more chance to penetrate through plasma plume. By increasing spray distance, large sized particles go far more downwards and penetrate through plasma jet due to their high momentum. In the mean time, the small sized particles got more and more separated from the large ones with increasing spray distance. It has also been revealed that the maximum flux location moves downward into the large particle region.

As shown in Figure 8-4 temperature of plasma jet changes drastically with spray distance. For various materials, the region for heating up and melting are different. For

example, as shown in Figure 8-4, because of the high melting point of YSZ (2950K) and Mo (2895K), the heating zone for these two materials is only about 5 cm with optimized injection (optimum particle trajectory). After particles fly out of this zone, they actually will be cooled down by the jet and re-solidification may occur. On the other hand, materials with low melting point such as NiCrAlY can be heated up at much longer spray distance (about 10 cm as shown in Figure 8-4) and keep the molten status correspondingly. This provides explanation for the combined effects of injection angle and spray distance (shown in Figure 4-6) on the behavior of in-flight particles in the injection optimization study (shown in Figure 5-6).

To study the effect of spray distance on particle molten status, not only the particle heating and acceleration history but also the particle properties need to be taken into consideration. As discussed in Chapter 6, different materials show drastically different molten status and re-solidification may occur (shown in Figure 6-8).

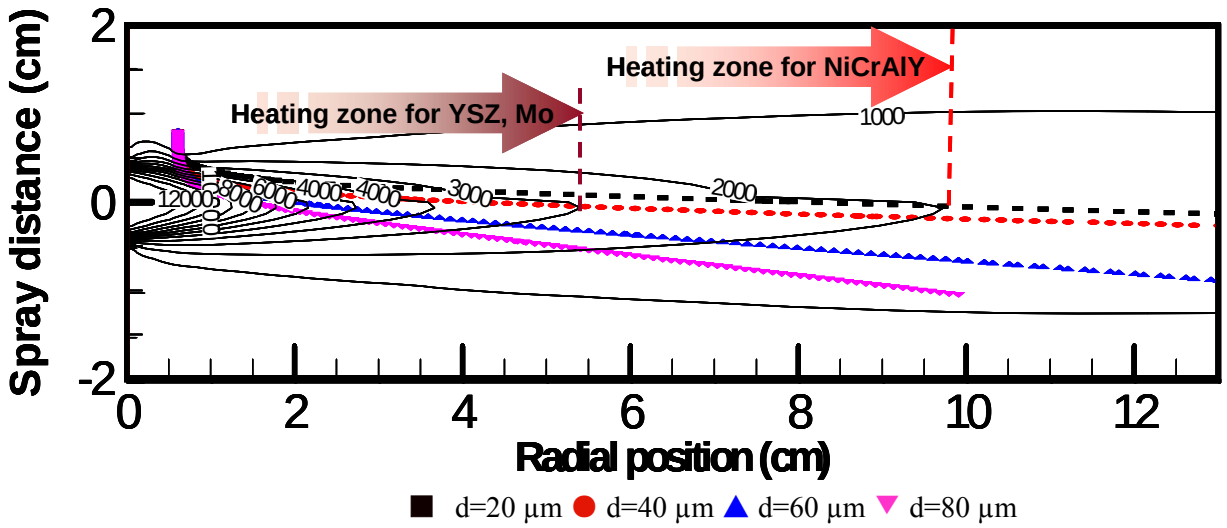

Figure 8-4 Trajectories of different sized YSZ in temperature profile of plasma plume

8.1.3 Representation of Particle In-flight Status

In Chapter 7, the definition and physical interpretation of non-dimensional group parameters, Melting Index, Reynolds number, Kinetic energy and Oxidation Index had been described and the advantages of using these parameters to represent particle in-flight status had been discussed. The outcome of such a strategy is a universal method for representation of in-flight particle characteristics in thermal spray processes. As discussed in Chapter 7, this new approach offers significant advantages over traditional T-V based 1st order maps. These maps also allow for representation of molten and kinetic status of multiple materials in a unified map.

Figure 8-5 shows the combined effect of injection angle and spray distance on particle molten and kinetic energy status. It can be concluded that, for all the tested spray distances, both the K.E. and M.I. of particle decrease with the increase of the injection angle. When the injection angle is fixed, the particle M.I. will decrease with the spray distance, while the particle K.E. will also decrease with the spray distance. The injection angle effect is found to be independent of spray distance. As discussed in Chapter 7, these group parameters provide better representation for particle status at impact. Meanwhile these results further confirmed the discussions on the evaluation of particle status during in-flight process in Chapter 4.

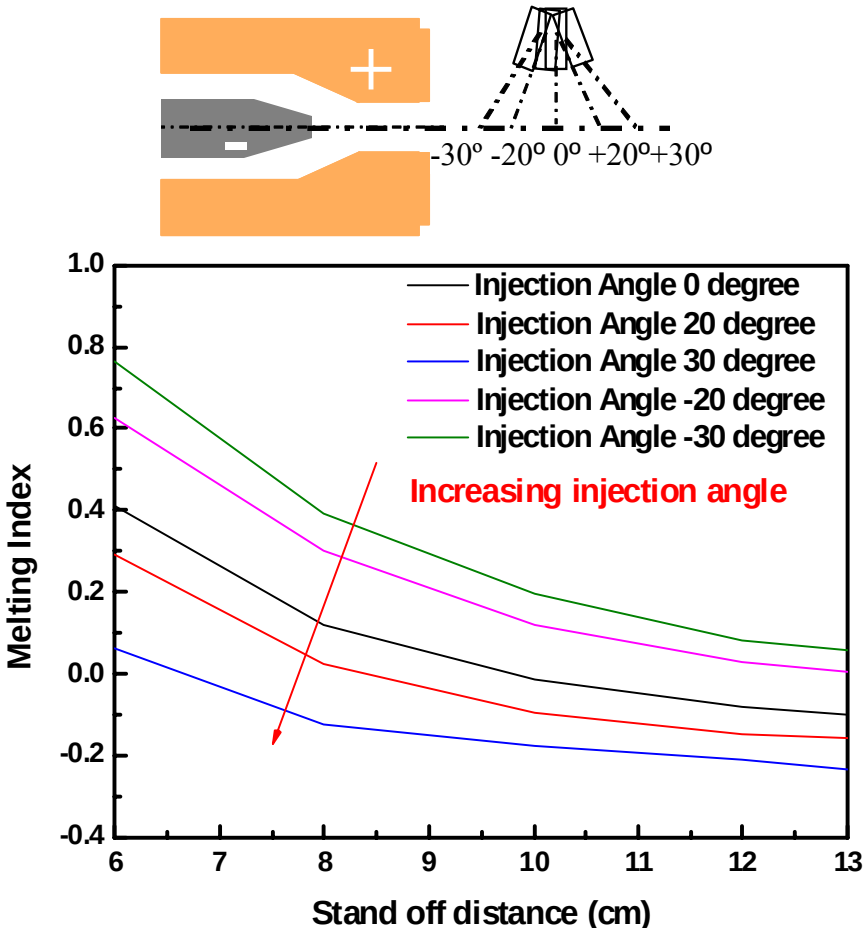

(a)

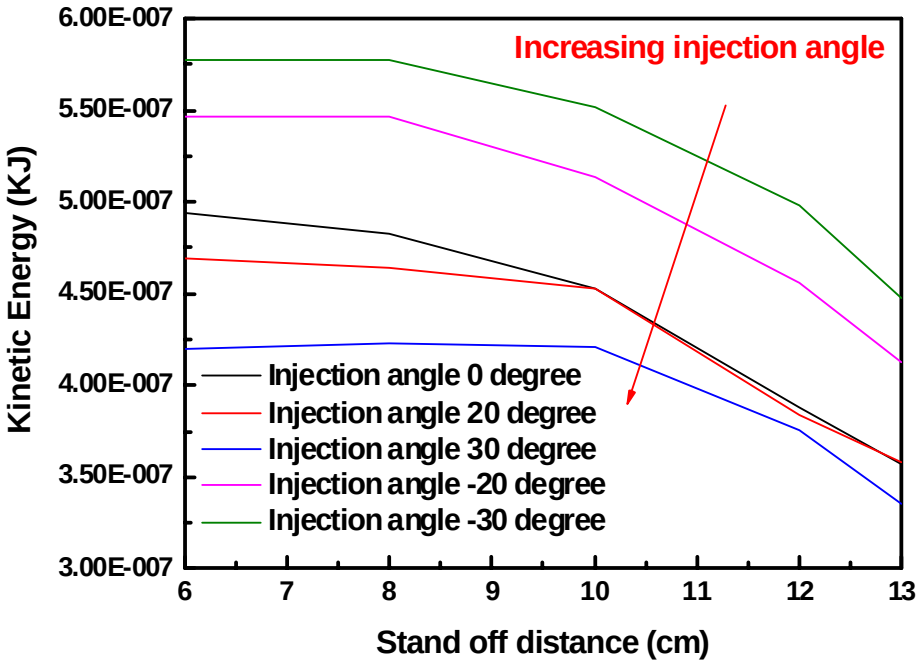

(b)

Figure 8-5 Effect of injection angle and spray distance on (a) particle Melting Index (M.I.), and (b) particle Kinetic Energy (K.E.)

8.2 Integration of Results

This dissertation focuses on the integration of process diagnostic and three-dimensional simulation in thermal spraying. Particle injection, plasma/particle interaction as well as in-flight particle status representation for multiple materials and processes have been systemically investigated through the integration of experiment and numerical simulation. The particle impact, flattening, spreading and mechanism of their evaluation which correlate strongly with the in-flight particle status have also been investigated.

Particle injection is a critical first step, which once controlled results in a more stable process and allows for critical examination of the real influence of plasma characteristics on the in-flight particle state. It is known that different hardware configurations will result in different in-flight particle states. This calls for complete description of spray stream (the in-flight state of the process as a whole). The insufficiency of average particle temperature and velocity has been investigated in this study. Particle characteristics (temperature, velocity, size, etc.) distributions have been examined critically for multiple materials under various process conditions in order to provide better understanding towards complete description of spray stream. Group parameters (M.I., Re, K.E. and O.I.) have been used to describe the particle state and

their relation to coating properties has been established using the concept of process maps. This allows for identification of process windows to achieve the desired combination of design relevant properties.

Through the integration of process diagnostics and numerical simulation, key issues concerning in-flight particle status as well as the controlling physical mechanisms have been analyzed. A scientific and intellectual strategy for universal description of particle characteristics has been successfully developed.

Chapter 9 Conclusions

This dissertation research focuses on the integration of process diagnostic and three-dimensional simulation in thermal spraying. The splat formation, substrate melting and mechanism of their evaluation which correlate strongly with the in-flight particle status have also been investigated. Some of the key results are summarized as followings:

9.1 Particle Radial Injection into Plasma Jet

9.1.1 Injection Angle and Carrier gas Flow Rate on In-flight Particle Characteristics

- Influence of injection angle on particle in-flight behaviors and characteristics has been investigated through an integrated modeling and experimental approach. It is found that experiment and simulation results agree every well with each other.
- Injection angle and carrier gas flow rate both have the significant impact on the plasma jet and in-flight particle trajectory, consequently, particle surface temperature and particle velocity. When the carrier gas flow rate is fixed, high particle surface temperature can be achieved at a small injection angle while the high particle speed can be achieved at a large injection angle. This observation is independent of the primary and secondary gas flow rate and spray distance.
- In the case of both carrier gas flow and injection angle changing, a high carrier gas flow rate and a small injection angle should be used to ensure high particle temperature and velocity at a certain spray distance.

9.1.2 Plasma Forming Process Parameters Effect on Optimum Particle Injection

- Systematical investigation has been carried out to identify and quantify maximum average temperature and velocity at any given spray distance. Diagnostic tools have been used to measure the distributions of individual particle characteristics at particle flux center and at various points (square grid) in the plume cross-section.
- Particle temperature and velocity will initially increase with increasing plume angle and then decrease after reaching a maximum value. This trend has been observed at the same plume angle for different combinations of process parameters from both experiment and simulation.
- Theoretical analysis shows that the plume angle is related to the velocity ratio of vertical contribution from carrier gas to the horizontal one from primary

and secondary gas. The observation is essential to guide the injection optimization through various process conditions.

9.2 Generic Correlation of Spray Distance with In-flight Particle Behavior for Different Kinds of Materials

- Studies have been carried out to examine the statistical distributions of in-flight particle characteristics for different kinds of materials in a systematical way. To reveal the heating and melting process of metal, alloy and ceramics powders, experiments were conducted to study the in-flight particle characteristics and their distributions at different spray distances.
- By analyzing the distributions at multiple spay distances, ones with the highest particle thermal and kinetic energy can be determined.
- Statistical distribution for particle temperature becomes narrower as spray distance increases. Simulations were conducted and results have been used to explain the particle behaviors observed in the experiments. Rapid cooling down of small sized particles at a long spray distance explains the narrowing of statistical temperature distribution as spray distance increases.
- The location of the maximum flux is shifted from small to large particle size, which can be used to understand the increase of particle size reading in the experiments as spray distance increases.
- Particle surface temperature is a good indicator for metal and alloy particle molten status. For ceramics, due to the low thermal conductivity and large heat capacity, determination of particle molten status becomes more complicated. Also, re-solidification may occur for semi-molten particles, especially for the larger sized ones.

9.3 Universal Description of Particle Characteristics and Development of Global Process Map

- A new strategy for visualization and representation of particle diagnostic results for thermal spray processes has been presented. The definition and physical interpretation of non-dimensional group parameters, Melting Index and Reynolds number, have been described and the advantages of using these parameters to represent particle in-flight status have been discussed.
- An additional group parameter, Oxidation Index, has been defined and used to represent the measurement of in-flight oxidation of metallic particles under various parametric conditions. O.I.-M.I. and O.I.-Re process maps has been used to further reveal particle in-flight status for a certain material under various process conditions.

- This universal method for representation of in-flight particle characteristics in thermal spray processes results in a global 1st order process map, comparing across a spectrum of materials for air plasma spray process. This offers significant advantages over traditional T-V based 1st order maps. These maps also allow for representation of molten and kinetic status of multiple materials and can be successfully represented in a unified map.
- By expanding the maps to include entire distributions of the M.I.-Re space, a more comprehensive comparison of molten status among multiple materials can be realized by enabling critical cross-comparison of process-material interactions amongst different spraying systems and different materials.
- The new mapping strategies have also been proposed in circumstances where only ensemble particle diagnostics are available.

Chapter 10 Suggestions for Future Work

10.1 Improve Definition of Particle Molten Status

In the Melting Index definition, the flame temperature, T_f, and heat transfer coefficient, h, keep changing with environment. Different materials, even same material particles under different conditions, have different T_f and h, both of which can only be obtained from numerical simulation for real-time values. The particle surface temperature, T_s, has been used to calculate M.I. considering the integration of thermal energy exchange history between the in-flight particles and their environment, since it is difficult to monitor the real time flame temperature in the vicinity of the flying particles. The average heat transfer coefficient, h, between the in-flight particles and their vicinity in the whole plasma plume field has been used to calculate the *M.I.*. These procedures will inevitably introduce inaccuracies when presenting particle molten status.

In addition, the current definition of Melting Index only considers heating up process of in-flight particles. Re-solidification of particles, however, has not been considered, which means that the equation is only valid in the distance range of particles heating up. However the molten status at impact (usually at large stand off distances) is what one really cares about. With a large stand off distance the particle re-solidification is inevitable, especially for the refractory materials such as YSZ and Al_2O_3, etc.

In the future work, revision of the Melting Index definition should be conducted to take into account of the two issues mentioned above, so as to further improve the model accuracy and expand its application range.

10.2 Improve Representation of Particle Oxidation Status

The oxidation mechanism for Mo has been investigated by Xiong et al. [73] and included in the 3D Lava code. For other materials such as W, WC-Co, Ni etc., the corresponding oxidation mechanisms need to be investigated and included in the code to reveal the oxidation effect on the particle status.

Zhang et al derived a dimensionless parameter, *Oxidation Index(O.I.)*, to characterize the oxide content of the in-flight particles[73].

$$O.I. \approx \frac{6\left(Y_{o,f}-Y_{o,c}\right)}{\rho_l}\frac{W_{ox}}{W_o}\frac{\mathrm{Sh}\,\rho_f D_{o,f}}{d_p}\frac{S}{V_P d_p} \propto \frac{S}{V_P d_p^2} \tag{10-1}$$

where $Y_{o,f}$ and $Y_{o,c}$ are the oxygen concentration in the gas phase and in the particle center, respectively, W_o and W_{ox} are the atomic weight of the oxidant and the oxide product, respectively, *Sh* is the Sherwood number and it is defined as $Sh = \frac{2h_m r_p}{\rho_f D_{o,f}}$, $D_{o,f}$ is

the diffusion coefficient of the oxygen in the plasma flame, ρ_f is the Favre-averaged gas density around the particle and h_m is the mass transfer coefficient between the particle surface and the environment. It should be noted that the mass transfer coefficient and the oxygen concentration surrounding the particles, which are critical in the O.I. calculation, can only be estimated from numerical simulation, since it is difficult to measure the real time values in experiments. Equation (10-1) also reveals that the oxide content increases monotonically with the spray distance, and decreases with increasing particle size and velocity. Instead of using the explicit equation provided earlier, values of $\frac{S}{V_P d_p^2}$ has been used to approximate O.I. [73, 166]. It has been shown that plotting the experimentally measured oxide content against the O.I. calculated based on S, V_p and d_p provides reasonable agreement. This method, however, can be only used to compare oxidation level of a certain feed material under different torch operating conditions. More research efforts need to be focused on realizing the comparison of oxidation status among multiple materials and processes.

10.3 Continue Global Process Map Development

Based on the current universal method of particle in-flight status representation, second-order global process maps should also be further developed, in which the following issues might be addressed:

1. Studying the morphology of splats as well as coatings of different materials under multiple thermal spray processes;
2. Obtaining the splat flattening ratio through both experiment and modeling for multiple materials and processes;
3. Measuring the coating properties such as porosity, elastic modulus and thermal conductivity etc. and including the information to the global process map.

Through the suggested future works mentioned above, the Process-Property-Performance relationship will be better understood.

References:

1. A. Kulkarni, J. Gutleber, S. Sampath, A. Goland, W.B. Lindquist, H. Herman, A.J. Allen, and B. Dowd, *Studies of the microstructure and properties of dense ceramic coatings produced by high-velocity oxygen-fuel combustion spraying.* Materials Science and Engineering a-Structural Materials Properties Microstructure and Processing, 2004. **369**(1-2): p. 124-137.
2. H. Herman, S. Sampath, and R. McCune, *Thermal spray: Current status and future trends.* Mrs Bulletin, 2000. **25**(7): p. 17-25.
3. S.A. Dembovsky and E.A. Chechetkina, *Model for Photostructural Changes in Chalcogenide Glassy Semiconductors.* Materials Research Bulletin, 1985. **20**(3): p. 321-328.
4. G. Renouard-Vallet, L. Bianchi, P. Fauchais, M. Vardelle, M. Boulos, and F. Gitzhofer, *Influence of spray technology on ionic conductivity of yttria stabilized zirconia.* High Temperature Material Processes, 2005. **9**(2): p. 195-209.
5. A. Essoltani, P. Proulx, M.I. Boulos, and A. Gleizes, *Effect of the Presence of Iron Vapors on the Volumetric Emission of Ar/Fe and Ar/Fe/H2 Plasmas.* Plasma Chemistry and Plasma Processing, 1994. **14**(3): p. 301-315.
6. J.B. Cox and F.J. Weinberg, *Behavior of Enthalpy Probes in Fluctuationg Temperature Encironments.* Journal of Physics D-Applied Physics, 1971. **4**(7): p. 877-880.
7. G. Gouesbet, *A Review on Measurements of Particle Velocities and Diameters by Laser Techniques, with Emphasis on Thermal Plasmas.* Plasma Chemistry and Plasma Processing, 1985. **5**(2): p. 91-117.
8. J.F. Coudert, M.P. Planche, and P. Fauchais, *Velocity-Measurement of Dc Plasma Jets Based on Arc Root Fluctuations.* Plasma Chemistry and Plasma Processing, 1995. **15**(1): p. 47-70.
9. G. Soucy, J.W. Jurewicz, and M.I. Boulos, *Parametric Study of the Decomposition of Nh3 for an Induction Plasma Reactor Design.* Plasma Chemistry and Plasma Processing, 1995. **15**(4): p. 693-710.
10. M. Rahmane, G. Soucy, and M.I. Boulos, *Diffusion phenomena of a cold gas in a thermal plasma stream.* Plasma Chemistry and Plasma Processing, 1996. **16**(1): p. S169-S189.
11. J.S. Gold, J.M. Lannon, K.S. Ziemer, M. Guntu, V.L. Tolani, and C.D. Stinespring, *Characterization of a methyl radical source for ultrahigh vacuum thin film growth studies.* Journal of Vacuum Science & Technology A, 2006. **24**(4): p. 1044-1050.
12. T. Hoffman, *Real-Time Imaging for Process-Control.* Advanced Materials & Processes, 1991. **140**(3): p. 37-42.
13. Z. Duan, L. Beall, J. Schein, J. Heberlein, and M. Stachowicz, *Diagnostics and modeling of an argon/helium plasma spray process.* Journal of Thermal Spray Technology, 2000. **9**(2): p. 225-234.
14. A. Vardelle, M. Vardelle, and P. Fauchais, *Diagnostics for Particulate Vaporization and Interactions with Surfaces.* Pure and Applied Chemistry, 1992. **64**(5): p. 637-644.
15. J.D. Ramshaw and C.H. Chang, *Computational Fluid-Dynamics Modeling of Multicomponent Thermal Plasmas.* Plasma Chemistry and Plasma Processing, 1992. **12**(3): p. 299-325.

16. C.H. Chang and J.D. Ramshaw, *Numerical-Simulation of Nonequilibrium Effects in an Argon Plasma-Jet.* Physics of Plasmas, 1994. **1**(11): p. 3698-3708.
17. C.H. Chang and J.D. Ramshaw, *Modeling of nonequilibrium effects in a high-velocity nitrogen-hydrogen plasma jet.* Plasma Chemistry and Plasma Processing, 1996. **16**(1): p. S5-S17.
18. A. Vardelle, N.J. Themelis, B. Dussoubs, M. Vardelle, and P. Fauchais, *Transport and chemical rate phenomena in plasma sprays.* High Temperature Material Processes, 1997. **1**(3): p. 295-313.
19. M.Z. Tokar, D. Kalupin, and D. Pilipenko, *Numerical solution of transport equations for plasmas with transport barriers.* Computer Physics Communications, 2006. **175**(1): p. 30-35.
20. G. Mariauc, E. Legros, A. Vardelle, *Modeling of coating formation and heat flux to substrate by particles and plasma jet in plasma spraying.* Thermal Spray 2003: Advanceing the Science & applying the Technology, 2003: p. 895-903.
21. B. Jodoin and P. Proulx, *Mathematical modeling of the supersonic d.c. plasma spray torch: Influence of hydrogen and current intensity.* High Temperature Material Processes, 2000. **4**(1): p. 43-68.
22. K.D. Kang and S.H. Hong, *Numerical analysis of shroud gas effects on air entrainment into thermal plasma jet in ambient atmosphere of normal pressure.* Journal of Applied Physics, 1999. **85**(9): p. 6373-6380.
23. D.A. Dippolito, J.R. Myra, J. Jacquinot, and M. Bures, *Radio-Frequency-Sheath-Driven Edge Plasma Convection and Interaction with the H-Mode.* Physics of Fluids B-Plasma Physics, 1993. **5**(10): p. 3603-3617.
24. H.X. Wang, K. Cheng, X. Chen, and W.X. Pan, *Three-dimensional modeling of heat transfer and fluid flow in laminar-plasma material re-melting processing.* International Journal of Heat and Mass Transfer, 2006. **49**(13-14): p. 2254-2264.
25. K. Cheng, X. Chen, H.X. Wang, and W.X. Pan, *Modeling study of shrouding gas effects on a laminar argon plasma jet impinging upon a flat substrate in air surroundings.* Thin Solid Films, 2006. **506**: p. 724-728.
26. I. Ahmed and T.L. Bergman, *Simulation of thermal plasma spraying of partially molten ceramics: Effect of carrier gas on particle deposition and phase change phenomena.* Journal of Heat Transfer-Transactions of the ASME, 2001. **123**(1): p. 188-196.
27. G. Mariaux, P. Fauchais, A. Vardelle, and B. Pateyron, *Modeling of the plasma spray process : From powder injection to coating formation.* High Temperature Material Processes, 2001. **5**(1): p. 61-85.
28. H.P. Li and X. Chen, *Three-dimensional simulation of a plasma jet with transverse particle and carrier gas injection.* Thin Solid Films, 2001. **390**(1-2): p. 175-180.
29. J.F. Shaeffer, *Swirl Arc - Model for Swirling, Turbulent, Radiative Arc Heater Flowfields.* Aiaa Journal, 1978. **16**(10): p. 1068-1075.
30. J.J. Gonzalez, A. Gleizes, S. Vacquie, and P. Brunelot, *Modeling of the Cathode Jet of a High-Power Transferred Arc.* Plasma Chemistry and Plasma Processing, 1993. **13**(2): p. 237-271.
31. C.H. Chang and J.D. Ramshaw, *Numerical Simulations of Argon Plasma Jets Flowing into Cold-Air.* Plasma Chemistry and Plasma Processing, 1993. **13**(2): p. 189-209.

32. K. Cheng and X. Chen, *Prediction of the entrainment of ambient air into a turbulent argon plasma jet using a turbulence-enhanced combined-diffusion-coefficient method.* International Journal of Heat and Mass Transfer, 2004. **47**(23): p. 5139-5148.
33. H.P. Li and X. Chen, *Three-dimensional modeling of the turbulent plasma jet impinging upon a flat plate and with transverse particle and carrier-gas injection.* Plasma Chemistry and Plasma Processing, 2002. **22**(1): p. 27-58.
34. M.K. Shin, S.D. Lee, S.H. Joo, and J.K. Yoon, *A Numerical Study on the Combustion Phenomena Occurring at the Post Combustion Stage in Bath-Type Smelting Reduction Furnace.* Isij International, 1993. **33**(3): p. 369-375.
35. K. Cheng, X. Chen, and W.X. Pan, *Comparison of laminar and turbulent thermal plasma jet characteristics - A modeling study.* Plasma Chemistry and Plasma Processing, 2006. **26**(3): p. 211-235.
36. P.C. Huang, J. Heberlein, and E. Pfender, *A 2-Fluid Model of Turbulence for a Thermal Plasma-Jet.* Plasma Chemistry and Plasma Processing, 1995. **15**(1): p. 25-46.
37. Z.W. Lin, C.M. Ko, B.A. Li, B. Zhang, and S. Pal, *Multiphase transport model for relativistic heavy ion collisions.* Physical Review C, 2005. **72**(6).
38. H.-B. Xiong, L.-L. Zheng, S. Sampath, R.L. Williamson, and J.R. Fincke, *Three-dimensional simulation of plasma spray: effects of carrier gas flow and particle injection on plasma jet and entrained particle behavior.* International Journal of Heat and Mass Transfer, 2004. **47**(24): p. 5189-5200.
39. H.B. Xiong, L.L. Zheng, and T. Streibl, *A critical assessment of particle temperature distributions during plasma spraying: Numerical studies for YSZ.* Plasma Chemistry and Plasma Processing, 2006. **26**(1): p. 53-72.
40. J.D. Ramshaw and C.H. Chang, *Iteration Schemem for Implicit Calculations of Kinetic and Equilibrium Chemical-Reactions in Fluid-Dynamics.* Journal of Computational Physics, 1995. **116**(2): p. 359-364.
41. M. Vardelle, A. Vardelle, P. Fauchais, K.I. Li, B. Dussoubs, and N.J. Themelis, *Controlling particle injection in plasma spraying.* Journal of Thermal Spray Technology, 2001. **10**(2): p. 267-284.
42. A. Vardelle, P. Fauchais, B. Dussoubs, and N.J. Themelis, *Heat generation and particle injection in a thermal plasma torch.* Plasma Chemistry and Plasma Processing, 1998. **18**(4): p. 551-574.
43. C.C.H. Pfender E., *Plasma spray jets and plasma particulate interactions: modeling and experiment.* Coddest C. (Ed.), Proc. of ITSC 98, ASM International, 1998: p. 315-327.
44. F. Durst, A. Melling, and J.H. Whitelaw, *Principles and Practice of Laser Doppler Anemometry*. 1976, London, New York, San Francisco: Academic Press.
45. J.R. Fincke, D.C. Haggard, and W.D. Swank, *Particle temperature measurement in the thermal spray process.* Journal of Thermal Spray Technology, 2001. **10**(2): p. 255-266.
46. C. Moreau, M. Lamontagne, and P. Cielo, *Method and apparatus for monitoring the temperature and velocity of plasma sprayed particles*. 1991, National Research Council of Canada (Ottawa, CA): US.
47. J.R. Fincke, W.D. Swank, R.L. Bewley, D.C. Haggard, M. Gevelber, and D. Wroblewski, *Diagnostics and control in the thermal spray process.* Surface & Coatings Technology, 2001. **146**: p. 537-543.

48. J. Vattulainen, E. Hamalainen, R. Hernberg, P. Vuoristo, and T. Mantyla, *Novel method for in-flight particle temperature and velocity measurements in plasma spraying using a single CCD camera.* Journal of Thermal Spray Technology, 2001. **10**(1): p. 94-104.
49. T. Streibl, K.D. Landes, and G. Forster. *PSI : New Diagnostics For The Determination Of Particle Size And Shape In Thermal Spray Processes*. in *Thermal Spray : Surface Engineering via Applied Research (Proceedings of the 1st ITSC)*. 2000. Montreal, Canada: ASM International.
50. J. Zierhut, K.D. Landes, W. Krommer, and P. Heinrich. *Particle Flux Imaging (PFI) In-Situ Diagnostics for Thermal Coating Process*. in *Thermal Spray : Surface Engineering via Applied Research*. 2000. Montreal: ASM International.
51. A. Vardelle, M. Vardelle, H. Zhang, N.J. Themelis, and K. Gross, *Volatilization of metal powders in plasma sprays.* Journal of Thermal Spray Technology, 2002. **11**(2): p. 244-252.
52. K. Hollis and R. Neiser, *Particle temperature and flux measurement utilizing a nonthermal signal correction process.* Journal of Thermal Spray Technology, 1998. **7**(3): p. 392-402.
53. T. Streibl, A. Vaidya, M. Friis, V. Srinivasan, and S. Sampath, *A critical assessment of particle temperature distributions during plasma spraying: Experimental results for YSZ.* Plasma Chemistry and Plasma Processing, 2006. **26**(1): p. 73-102.
54. L. Li, A. Vaidya, S. Sampath, H.B. Xiong, and L.L. Zheng, *Particle characterization and splat formation of plasma sprayed zirconia.* Journal of Thermal Spray Technology, 2006. **15**(1): p. 97-105.
55. J.C. Fang, W.J. Xu, Z.Y. Zhao, and L. Wang, *Influence of in-flight particle characteristics on the forming quality*, in *Pricm 5: the Fifth Pacific Rim International Conference on Advanced Materials and Processing, Pts 1-5*. 2005. p. 2823-2826.
56. S. Guessasma, G. Montavon, and C. Coddet, *Velocity and temperature distributions of alumina-titania in-flight particles in the atmospheric plasma spray process.* Surface & Coatings Technology, 2005. **192**(1): p. 70-76.
57. E.J. Kubel, *Powders Dictate Thermal-Spray-Coating Properties.* Advanced Materials & Processes, 1990. **138**(6): p. 24-&.
58. V. Srinivasan, M. Friis, A. Vaidya, T. Streibl, and S. Sampath, *Particle injection in direct current air plasma spray: Salient observations and optimization strategies.* Plasma Chemistry and Plasma Processing, 2007. **27**(5): p. 609-623.
59. W. Zhang, L.L. Zheng, H. Zhang, and S. Sampath, *Study of injection angle and carrier gas flow rate effects on particles in-flight characteristics in plasma spray process: Modeling and experiments.* Plasma Chemistry and Plasma Processing, 2007. **27**: p. 701-716.
60. E.J. Kubel, *Powders Dictate Thermal-Spray-Coating Properties.* Advanced Materials & Processes, 1990. **138**(6): p. 24-29.
61. A. Vaidya, T. Streibl, L. Li, S. Sampath, O. Kovarik, and R. Greenlaw, *An integrated study of thermal spray process-structure-property correlations: A case study for plasma sprayed molybdenum coatings.* Materials Science and Engineering a-Structural Materials Properties Microstructure and Processing, 2005. **403**(1-2): p. 191-204.
62. A.A. Syed, A. Denoirjean, P. Fauchais, and J.C. Labbe, *On the oxidation of stainless steel particles in the plasma jet.* Surface & Coatings Technology, 2006. **200**(14-15): p. 4368-4382.

63. C. Lee and P.Y. Pac, *Heavy-Particle-Induced Effective Lagrangian in Spontaneously Broken Theories .1. the Sigma-Model.* Nuclear Physics B, 1981. **177**(1): p. 87-156.
64. Y.P. Wan, V. Prasad, G.X. Wang, S. Sampath, and J.R. Fincke, *Model and powder particle heating, melting, resolidification, and evaporation in plasma spraying processes.* Journal of Heat Transfer-Transactions of the Asme, 1999. **121**(3): p. 691-699.
65. Y.P. Wan, V. Gupta, Q. Deng, S. Sampath, V. Prasad, R. Williamson, and J.R. Fincke, *Modeling and visualization of plasma spraying of functionally graded materials and its application to the optimization of spray conditions.* Journal of Thermal Spray Technology, 2001. **10**(2): p. 382-389.
66. J. He, M. Ice, and E. Lavernia, *Particle melting behavior during high-velocity oxygen fuel thermal spraying.* Journal of Thermal Spray Technology, 2001. **10**(1): p. 83-93.
67. S. Dyshlovenko, B. Pateyron, L. Pawlowski, and D. Murano, *Numerical simulation of hydroxyapatite powder behaviour in plasma jet.* Surface & Coatings Technology, 2004. **179**(1): p. 110-117.
68. P. Fauchais and M. Vardelle, *Understanding the formation of DC plasma sprayed coatings*, in *Thermec'2003, Pts 1-5*. 2003. p. 2459-2465.
69. M. Prystay, P. Gougeon, and C. Moreau, *Structure of plasma-sprayed zirconia coatings tailored by controlling the temperature and velocity of the sprayed particles.* Journal of Thermal Spray Technology, 2001. **10**(1): p. 67-75.
70. I. Ahmed and T.L. Bergman, *Optimization of plasma spray processing parameters for deposition of nanostructured powders for coating formation.* Journal of Fluids Engineering-Transactions of the Asme, 2006. **128**(2): p. 394-401.
71. G. Delluc, H. Ageorges, B. Pateyron, and P. Fauchais, *Fast modelling of plasma jet and particle behaviours in spray conditions.* High Temperature Material Processes, 2005. **9**(2): p. 211-226.
72. H. Zhang, G. Wei, L. Zheng, L. Li, X.Y. Wang, and A. Vaidya, *Numerical and experimental studies of substrate melting and resolidification during thermal spraying.* Journal of Materials Science & Technology, 2003. **19**: p. 137-140.
73. H.B. Xiong, L.L. Zheng, L. Li, and A. Vaidya, *Melting and oxidation behavior of in-flight particles in plasma spray process.* International Journal of Heat and Mass Transfer, 2005. **48**(25-26): p. 5121-5133.
74. K. Volenik, V. Novak, J. Dubsky, P. Chraska, and K. Neufuss, *Properties of alloy steel coatings oxidized during plasma spraying.* Materials Science and Engineering a-Structural Materials Properties Microstructure and Processing, 1997. **234**: p. 493-496.
75. C.M. Hackett, and G.S. Settles, *Turbulent mixing of the HVOF thermal spray and coating oxidation* Thermal Spray Industry Applications, ASM International, Materials Park, 1994: p. 307-312.
76. M. Vardelle, A. Vardelle, A.C. Leger, P. Fauchais, and D. Gobin, *Influence of Particle Parameters at Impact on Splat Formation and Solidification in Plasma Spraying Processes.* Journal of Thermal Spray Technology, 1995. **4**(1): p. 50-58.
77. M.F. Smith, R.C. Dykhuizen, and R.A. Neise, *Thermal Spray: A United Forum for Scientific and Techynological Advances.* Proceeedings of the National Thermal Spray Conference, ASM International, 1997: p. 885-893.
78. Y.P. Wan, J.R. Fincke, X.Y. Jiang, S. Sampath, V. Prasad, and H. Herman, *Modeling of oxidation of molybdenum particles during plasma spray deposition.* Metallurgical and

Materials Transactions B-Process Metallurgy and Materials Processing Science, 2001. **32**(3): p. 475-481.
79. Y.P. Wan, J.R. Fincke, S. Sampath, V. Prasad, and H. Herman, *Modeling and experimental observation of evaporation from oxidizing molybdenum particles entrained in a thermal plasma jet.* International Journal of Heat and Mass Transfer, 2002. **45**(5): p. 1007-1015.
80. X. Chen, Y.P. Chyou, Y.C. Lee, and E. Pfender, *Heat-Transfer to A Particle Under Plasma Conditions with Vapor Contamination from the Particle.* Plasma Chemistry and Plasma Processing, 1985. **5**(2): p. 119-141.
81. S. Safai and H. Herman, *Microstructural Investigation of Plasma-Sprayed Aluminum Coatings.* Thin Solid Films, 1977. **45**(2): p. 295-307.
82. S. Sampath and H. Herman, *Rapid solidification and microstructure development during plasma spray deposition.* Journal of Thermal Spray Technology, 1996. **5**(4): p. 445-456.
83. X.Y. Jiang, S. Sampath, and H. Herman, *Grain morphology of molybdenum splats plasma-sprayed on glass substrates.* Materials Science and Engineering a-Structural Materials Properties Microstructure and Processing, 2001. **299**(1-2): p. 235-240.
84. P. Fauchais, M. Fukumoto, A. Vardelle, and M. Vardelle, *Knowledge concerning splat formation: An invited review.* Journal of Thermal Spray Technology, 2004. **13**(3): p. 337-360.
85. L. Bianchi, A. Grimaud, F. Blein, P. Lucchese, and P. Fauchais, *Comparison of Plasma-Sprayed Alumina Coatings by Rf and Dc Plasma Spraying.* Journal of Thermal Spray Technology, 1995. **4**(1): p. 59-66.
86. S. Sampath, X.Y. Jiang, J. Matejicek, L. Prchlik, A. Kulkarni, and A. Vaidya, *Role of thermal spray processing method on the microstructure, residual stress and properties of coatings: an integrated study for Ni-5 wt.%Al bond coats.* Materials Science and Engineering a-Structural Materials Properties Microstructure and Processing, 2004. **364**(1-2): p. 216-231.
87. D.G. Moore, *Studies of the Particle Impact Process for Applying Ceramic and Cermet Coating.* 1961, U.S. Air Force.
88. S. Safai and H. Herman, *Plasma-Sprayed Materials.* Treaties on Materials Science and Technology, 1981. **20**: p. 183-214.
89. M. Vardelle, A. Vardelle, A.C. Leger, and P. Fauchais. *Dynamics of Splat Formation and Solidification in Thermal Spraying Process*. in *Thermal Spray Industrial Applications*. 1994. Boston, MA: ASM International, Materials Park, OH, USA.
90. S. Fantassi, M. Vardelle, A. Vardelle, and P. Fauchais, *Influence of the Velocity of Plasma-sprayed Particles on Splat Formation.* J. Thermal Spray Technology, 1993. **2**(4): p. 379-384.
91. L. Bianchi, F. Blein, P. Lucchese, M. Vardelle, A. Vardelle, and P. Fauchais. *Effect of Particle Velocity and Substrate Temperature on Alumina and Zirconia Splat Formation*. in *Thermal Spray Industrial Applications*. 1994. Boston, MA: ASM International, Materials Park, OH, USA.
92. Z. Prochazka, K.A. Khor, and J. Cizek, *Influence of input parameters on splat formation and coating thermal diffusivity in plasma spraying.* Advanced Engineering Materials, 2006. **8**(7): p. 645-650.
93. A.C. Leger, M. Vardelle, A. Vardelle, P. Fauchais, S. Sampath, C. Berndt, and H. Herman. *Plasma Sprayed Zirconia: Relationship Between Particle Parameters, Splat*

Formation and Deposit Generation-Part I: Impact and Solidification. in *Thermal Spray: Practical Solution for Engineering Problems*. 1996. Cincinnati, OH: ASM International, Materials Park, OH, USA.

94. X.Y. Jiang, J. Matejicek, A. Kulkarni, H. Herman, S. Sampath, D.L. Gilmore, and R.A. Neiser. *Process Maps for Plasma Spray Part II: Deposition and Properties*. in *Thermal Spray: Surface Engineering via Applied Reseach*. 2000. Montreal, Quebec, Canada: ASM International, Materials Park, OH, USA.
95. R.N. Wright, J.R. Fincke, W.D. Swank, and D.C. Haggard. *Particle Velocity and Temperature Influences on Microstructure of Plasma Sprayed Nickel*. in *Thermal Spray: Practical Solution For Engineering Problems*. 1996. Cincinnati, OH: ASM International, Materials Park, OH, USA.
96. A. Bejan and D. Gobin, *Constructal theory of droplet impact geometry.* International Journal of Heat and Mass Transfer, 2006. **49**(15-16): p. 2412-2419.
97. A. Vardelle and P. Fauchais. *Oxidation of Metal Droplet in Plasma Spray*. in *Thermal Spray Science & Technology*. 1995. Houston, TX: ASM International, Materials Park, OH, USA.
98. G. Espie, P. Fauchais, J.C. Labbe, A. Vardelle, and B. Hannoyer. *Oxidation of Iron Particles during APS: Effect of the Process on Formed Oxide Wetting of Droplet on Ceramic Substrate*. in *Thermal Spray 2001: New Surfaces For A New Millennium*. 2001. Singapore: ASM International, Materials Park, OH, USA.
99. H. Jones, *Cooling, Freezing and Substrate Impact of Droplets Formed by Rotary Atomization.* Journal of Physics D-Applied Physics, 1971. **4**(11): p. 1657-1662.
100. J. Madejski, *Solidification of Droplets on a Cold Surface.* International Journal of Heat and Mass Transfer, 1976. **19**(9): p. 1009-1013.
101. P. Fauchais, A. Vardelle, and B. Dussoubs, *Quo vadis thermal spraying?* Journal of Thermal Spray Technology, 2001. **10**(1): p. 44-66.
102. Y.P. Wan, H. Zhang, X.Y. Jiang, S. Sampath, and V. Prasad, *Role of solidification, substrate temperature and Reynolds number on droplet spreading in thermal spray deposition: Measurements and modeling.* Journal of Heat Transfer-Transactions of the Asme, 2001. **123**(2): p. 382-389.
103. H. Zhang, *Theoretical analysis of spreading and solidification of molten droplet during thermal spray deposition.* International Journal of Heat and Mass Transfer, 1999. **42**(14): p. 2499-2508.
104. G.X. Wang, V. Prasad, S. Sampath, and H. Herman. *Modeling of Rapid Solidification During Splat Quenching*. in *Solidification 1998: Proceedings of Symposia Sponsored by the Solidification Committee of the Materials Design & Manufacturing Division of TMS*. 1998. Warrendale, PA: TMS.
105. C. Robert, G.X. Wang, A. Denoirjean, S. Sampath, A. Vardelle, and V. Prasad. in *Thermal Spray: A United Forum for Scientific and Technological Advances.* 1997. Indianapolis, IN: ASM International, Materials Park, OH, USA.
106. H. Zhang, X.Y. Wang, L.L. Zheng, and X.Y. Jiang, *Studies of splat morphology and rapid solidification during thermal spraying.* International Journal of Heat and Mass Transfer, 2001. **44**(24): p. 4579-4592.
107. H. Zhang, X.Y. Wang, L.L. Zheng, and S. Sampath, *Numerical simulation of nucleation, solidification, and microstructure formation in thermal spraying.* International Journal of Heat and Mass Transfer, 2004. **47**(10-11): p. 2191-2203.

108. A. Raessi, J. Mostaghimi, and M. Bussmann, *Effect of surface roughness on splat shapes in the plasma spray coating process.* Thin Solid Films, 2006. **506**: p. 133-135.
109. M. Vardelle, A. Vardelle, P. Fauchais, and C. Moreau, *Pyrometer System for Monitoring the Particle Impact on a Substrate During a Plasma Spray Process.* Measurement Science & Technology, 1994. **5**(3): p. 205-212.
110. M. Vardelle, A. Vardelle, K.I. Li, P. Fauchais, and N.J. Themelis, *Coating generation: Vaporization of particles in plasma spraying and splat formation.* Pure and Applied Chemistry, 1996. **68**(5): p. 1093-1099.
111. L. Bianchi, A.C. Leger, M. Vardelle, A. Vardelle, and P. Fauchais, *Splat formation and cooling of plasma-sprayed zirconia.* Thin Solid Films, 1997. **305**(1-2): p. 35-47.
112. F.L. Trifa, G. Montavon, and C. Coddet, *On the relationships between the geometric processing parameters of APS and the Al_2O_3-TiO_2 deposit shapes.* Surface & Coatings Technology, 2005. **195**(1): p. 54-69.
113. W.Z. Wang, C.J. Li, and Y.Y. Wang, *Effect of spray distance on the mechanical properties of plasma sprayed Ni-45Cr coatings.* Materials Transactions, 2006. **47**(7): p. 1643-1648.
114. O. Chumak, V. Kopecky, M. Konrad, M. Hrabovsky, and T. Kavka, *Powder particle penetration into steam-argon plasma jet and its relation with particle parameters.* Czechoslovak Journal of Physics, 2004. **54**: p. C931-C936.
115. J.C. Fang, W.J. Xu, H.S. Wang, and Z.Y. Zhao, *In-flight behavior of ceramic particle in plasma spray forming*, in *High-Performance Ceramics Iii, Pts 1 and 2*, P. Fauchais, J.v.d. Mullen, and J. Heberlein, Editors. 2005, Ann NY Acad Sci New York. p. 1807-1810.
116. C.W. Kang, H.W. Ng, and S.C.M. Yu, *Comparative study of plasma spray flow fields and particle behavior near to flat inclined substrates.* Plasma Chemistry and Plasma Processing, 2006. **26**(2): p. 149-175.
117. J.F. Li, H.L. Liao, C. Ding, and C. Coddet, *Optimizing the plasma spray process parameters of yttria stabilized zirconia coatings using a uniform design of experiments.* Journal of Materials Processing Technology, 2005. **160**(1): p. 34-42.
118. D. Zoler, C. Bruma, S. Cuperman, and S. Wald, *Theoretical modeling and optimization study of particle acceleration and heating inside an electrothermal-chemical device.* Physica Scripta, 1999. **59**(6): p. 462-474.
119. J. Mostaghimi, S. Chandra, R. Ghafouri-Azar, and A. Dolatabadi, *Modeling thermal spray coating processes: a powerful tool in design and optimization.* Surface & Coatings Technology, 2003. **163**: p. 1-11.
120. P. Fauchais, *Understanding plasma spraying.* Journal of Physics D-Applied Physics, 2004. **37**(9): p. R86-R108.
121. C. Moreau, J.F. Bisson, R.S. Lima, and B.R. Marple, *Diagnostics for advanced materials processing by plasma spraying.* Pure and Applied Chemistry, 2005. **77**(2): p. 443-462.
122. H.R. Salimijazi, L. Pershin, T.W. Coyle, J. Mostaghimi, S. Chandra, Y.C. Lau, L. Rosenzweig, and E. Moran, *Effect of droplet characteristics and substrate surface topography on the final morphology of plasma-sprayed zirconia single splats.* Journal of Thermal Spray Technology, 2007. **16**(2): p. 291-299.
123. K. Landes, *Diagnostics in plasma spraying techniques.* Surface & Coatings Technology, 2006. **201**(5): p. 1948-1954.

124. J.A. Brogan, C.C. Berndt, W.C. Smith, R.V. Gansert, S. Raghu, S. Sampath, and H. Herman, *Real-time imaging of the plasma spray process - Work in progress.* Journal of Thermal Spray Technology, 1995. **4**(4): p. 374-376.
125. A.F. Kanta, G. Montavon, M.P. Planche, and C. Coddet, *Plasma spray process on-line control by artificial intelligence methodology.* Advanced Engineering Materials, 2007. **9**(1-2): p. 105-113.
126. L. Prchlik, J. Gutleber, and S. Sampath, *Deposition and properties of high-velocity-oxygen-fuel and plasma-sprayed Mo-Mo_2C composite coatings.* Journal of Thermal Spray Technology, 2001. **10**(4): p. 643-655.
127. D.P. Guillen and B.G. Williams, *In-flight oxidation of aluminum in the twin-wire electric arc process.* Journal of Thermal Spray Technology, 2006. **15**(1): p. 63-71.
128. M.P. Planche, H. Liao, and C. Coddet, *Oxidation control in atmospheric plasma spraying coating.* Surface & Coatings Technology, 2007. **202**(1): p. 69-76.
129. C. Moreau, P. Gougeon, M. Lamontagne, V. Lacasse, G. Vaudreuil, and P. Cielo. *On-Line Control of the Plasma Spraying Process by Monitoring the Temperature, Velocity and Trajectory of In-Flight Particles*. in *Thermal spray Industrial Applications: Proceedings of 7th National Thermal Spray Conference*. 1994. Boston, MA, USA: ASM International, Materials Park, OH.
130. C. Moreau, P. Gougeon, A. Burgess, and D. Ross. in *Advances in Thermal Spray Science and Technology*. 1995: ASM International, Materials Park, OH.
131. W.D. Swank, J.R. Fincke, and D.C. Haggard. *A Particle Temperature Sensor for Monitoring and Control of the Thermal Spray Process*. in *Thermal Spray Science and Technology : Proceedings of the 8th National Thermal Spray Conference*. 1995. Houston, Texas, US: ASM International.
132. J.R. Fincke, D.C. Haggard, and W.D. Swank, *Particle Temperature Measurement in the Thermal Spray Process.* Journal of Thermal Spray Technology, 2001. **10(2)**(June): p. 255-266.
133. J.R. Fincke, W.D. Swank, R.L. Bewley, D.C. Haggard, M. Gevelber, and D. Wroblewski, *Diagnostics and control in the thermal spray process.* Surface and Coatings Technology, 2001. **146-147**: p. 537-543.
134. S. Vasudevan, *Preliminary Exam: An Integrated Approach towards Synthesis and Control of Microstructure and Properties of Thermal Sprayed Materials.* Stony Brook Unisity, 2005: p. 3-4.
135. J.R. Fincke, C.H. Chang, W.D. Swank, and D.C. Haggard, *Entrainment and Demixing in Subsonic Thermal Plasma Jets - Comparison of Measurements and Predictions.* International Journal of Heat and Mass Transfer, 1994. **37**(11): p. 1673-1682.
136. J.D. Ramshaw and C.H. Chang, *Ambipolar Diffusion in Multicomponent Plasmas.* Plasma Chemistry and Plasma Processing, 1991. **11**(3): p. 395-402.
137. G.X. Wang and E.F. Matthys, *Modeling of nonequilibrium surface melting and resolidification for pure metals and binary alloys.* Journal of Heat Transfer-Transactions of the Asme, 1996. **118**(4): p. 944-951.
138. M.K. Stanford, C. DellaCorte, and D. Eylon, *Effect of particle morphology on flow characteristics of a composite plasma spray powder.* Journal of Thermal Spray Technology, 2004. **13**(4): p. 586-592.

139. K. Ramachandran and H. Nishiyama, *Three-dimensional effects of carrier gas and particle injections on the thermo-fluid fields of plasma jets.* Journal of Physics D-Applied Physics, 2002. **35**(4): p. 307-317.
140. K. Ramachandran and H. Nishiyama, *Fully coupled 3D modeling of plasma-particle interactions in a plasma jet.* Thin Solid Films, 2004. **457**(1): p. 158-167.
141. H.B. Xiong, L.L. Zheng, S. Sampath, R.L. Williamson, and J.R. Fincke, *Three-dimensional simulation of plasma spray: effects of carrier gas flow and particle injection on plasma jet and entrained particle behavior.* International Journal of Heat and Mass Transfer, 2004. **47**(24): p. 5189-5200.
142. A.A. Amsden, P.J. O'Rourke, and T.D. Butler, *KIVA-II: a computer program for chemically reactive flows and fuel sprays*, in *Report LA-11560-MS*. May 1989, Los Alamos National Laboratory.
143. L.D. Zhao, K. Seemann, A. Fischer, and E. Lugscheider, *Study on atmospheric plasma spraying of Al_2O_3 using on-line particle monitoring.* Surface & Coatings Technology, 2003. **168**(2-3): p. 186-190.
144. J.R. Fincke, W.D. Swank, and D.C. Haggard, *The influence of injector geometry and carrier gas flow rate on spray pattern*, in *Thermal spray: A united forum for scientific and technological advances; Proceedings of the 1st United Thermal Spray Conference*. 1997: Indianapolis, IN, UNITED STATES. p. 335-342.
145. J.R. Fincke, W.D. Swank, and D.C. Haggard, *More on the influence of injector geometry and carrier gas flow rate on spray pattern and particle temperature*, in *ITSC 2000: 1st International Thermal Spray Conference*. 2000: Montreal, Quebec, Canada. p. 9-14.
146. E. Pfender and C.H. Chang, *Plasma spray jets and plasma-particulate interaction: modeling and experiments*, in *15th International Thermal Spray Conference*. 1998: Nice, France. p. 315-327.
147. A. Vaidya, *A Fundamental Approach to Process-Property Relationships*, in *Materials Sciences and Engineering*. 2004, Stony Brook University: Stony Brook, NY. p. 30-32.
148. S. Guessasma and M. Bounazef, *Experimental design to study the effect of APS process parameters on friction behaviour of alumina-titania coatings.* Advanced Engineering Materials, 2004. **6**(11): p. 907-910.
149. A. Kucuk, R.S. Lima, and C.C. Berndt, *Influence of plasma spray parameters on in-flight characteristics of ZrO2-8 wt% Y2O3 ceramic particles.* Journal of the American Ceramic Society, 2001. **84**(4): p. 685-692.
150. L.B. Delcea, *Plasma torch with axial injection of feedstock*. 1995: USA.
151. A. Vaidya, *Thesis: Process Maps for Thermal Spray: A Fundamental Approach to Process-Property Relationships.* Stony Brook Unisity, 2004: p. 30-32.
152. H. Zhang, H.B. Xiong, L.L. Zheng, A. Vaidya, L. Li, and S. Sampath, *in Thermal Spray: Advancing the Science and Applying the Thechnology.* Pub. ASM International, Materials Park, Ohio, 2003: p. 905-911.
153. B.L. Choi and S.H. Hong, *Theoretical investigations on sprayed particle-plasma interactions to optimize processing parameters in DC thermal plasma spraying.* Materials and Manufacturing Processes, 1997. **12**(2): p. 309-328.
154. S. Das, V.K. Suri, U. Chandra, and K. Sampath, *One-Dimensional Mathematical-Model for Selecting Plasma Spray Process Parameters.* Journal of Thermal Spray Technology, 1995. **4**(2): p. 153-162.

155. P.C. Huang, J. Heberlein, and E. Pfender, *Particle Behavior in a 2-Fluid Turbulent-Plasma Jet.* Surface & Coatings Technology, 1995. **73**(3): p. 142-151.
156. E. Pfender, *Plasma-Jet Behavior and Modeling Associated with the Plasma Spray Process.* Thin Solid Films, 1994. **238**(2): p. 228-241.
157. LS 13 320 Particle Size Analyzer, Beckman Coulter Inc. Particle Characterization Group.
158. C. Moreau, Gougeon P, Lamontagne M, Lacasse V, Vaudreuil G and Cielo P, *1994 Thermal Spray: Industrial Applications.* ASM International Materials Park, 1994: p. 431-437.
159. A. Vaidya, Banked, G., Sampath, S., and Herman, H., *Influence of Process Variables on the Plasma Sprayed CoatingsL An Integrated Study.* International Thermal Spray Conference, 2001: p. 1345-1349.
160. M. Fukumoto, E. Nishioka, and T. Nishiyama, *New criterion for splashing in flattening of thermal sprayed particles onto flat substrate surface.* Surface & Coatings Technology, 2002. **161**(2-3): p. 103-110.
161. C. Escure, M. Vardelle, and P. Fauchais, *Experimental and theoretical study of the impact of alumina droplets on cold and hot substrates.* Plasma Chemistry and Plasma Processing, 2003. **23**(2): p. 185-221.
162. C.J. Li, H.L. Liao, P. Gougeon, G. Montavon, and C. Coddet, *Experimental determination of the relationship between flattening degree and Reynolds number for spray molten droplets.* Surface & Coatings Technology, 2005. **191**(2-3): p. 375-383.
163. K. Shinoda, T. Koseki, and T. Yoshida, *Influence of impact parameters of zirconia droplets on splat formation and morphology in plasma spraying.* Journal of Applied Physics, 2006. **100**(7).
164. S. Sampath, X. Jiang, A. Kulkarni, J. Matejicek, D.L. Gilmore, and R.A. Neiser, *Development of process maps for plasma spray: case study for molybdenum.* Materials Science and Engineering a-Structural Materials Properties Microstructure and Processing, 2003. **348**(1-2): p. 54-66.
165. M. Fukumoto, M. Shiiba, H. Kaji, and T. Yasui, *Three-dimensional transition map of flattening behavior in the thermal spray process.* Pure and Applied Chemistry, 2005. **77**(2): p. 429-442.
166. G. Espie, P. Fauchais, B. Hannoyer, J.C. Labbe, and A. Vardelle, *Effect of metal particles oxidation during the APS on the wettability*, in *Heat and Mass Transfer under Plasma Conditions*. 1999. p. 143-151.
167. Y. Wan, H. Zhang, X. Jiang, S. Sampath, and V. Prasad, *Role of solidification, substrate temperature and Reynolds number on droplet spreading in thermal spray deposition: measurements and modeling.* J.Heat Trans., 2001. **123**: p. 382-389.
168. V. Srinivasan, A. Vaidya, T. Streibl, M. Friis, and S. Sampath, *On the reproducibility of air plasma spray process and control of particle state.* Journal of Thermal Spray Technology, 2006. **15**(4): p. 739-743.
169. M. Vardelle and P. Fauchais, *Plasma spray processes: diagnostics and control?* Pure and Applied Chemistry, 1999. **71**(10): p. 1909-1918.